# 國 立 交 通 大 學

## 應用化學研究所

## 碩 士 論 文

新穎低表面能材料 Polybenzoxazine 高分子之應用及其運用

於能表面自清潔的超疏水材料之研究

**A Novel Low Surface Free Energy Material Polybenzoxazine**

**Characterization and Applications for Superhydrophobic**

**and Smart Surface Material**

研 究 生：李昌源

指導教授：張豐志 教授

中 華 民 國 九 十 八 年 七 月

# 新穎低表面能材料 Polybenzoxazine 高分子之應用及其運用於能表面自清潔的超疏水材料之研究

# A Novel Low Surface Free Energy Material Polybenzoxazine Characterization and Applications for Superhydrophobic and Smart Surface Material


研 究 生：李昌源　　Student：Chang-Yung Li

指導教授：張豐志　　Advisor：Dr. Feng-Chih Chang

國 立 交 通 大 學

應 用 化 學 研 究 所


碩 士 論 文

**A Thesis**

**Submitted to Institute of Applied Chemistry**

**College of Science**

**National Chiao Tung University**

**In partial Fulfillment of the Requirements**

**For the Degree of Master of Science**

**In Applied Chemistry**

**July 2009**

**Hsinchu, Taiwan, Republic of China**

中華民國九十八年七月

## ACKNOWLEDGMENTS

The author wishes to express his deepest appreciation to his adviser,Dr. Feng-Chih Chang , and Dr. Chih-Feng Wang for their kindly guidance and patience throughout this research during the past two years. In addition, the thanks are also due to my classmates for their assistance to finish this research. Finally, I am thankful to my family for their support and understanding.

# 新穎低表面能材料 Polybenzoxazine 高分子之應用及其運用於能表面自清潔的超疏水材料之研究

學生:李昌諒　　指導教授:張豐志 教授

國立交通大學應用化學研究所

## 摘 要

在文獻中，我們得知降低高分子表面能的方法大多以加入含氟的化合物或其官能基。而利用高分子的分子間作用力與分子內作用力來改變表面能，此為一嶄新的方向，但相關探討仍屬少見。由於本實驗室發現高分子 polybenzoxazine 具有非常低表面能之特性，此特性在高分子中的化學性質與物理性質皆佔有相當重要的影響。

由於 polybenzoxazine 具有較鐵氟龍更低的表面能，是一個新穎的疏水低表面能材料，除此之外，Polybenzoxazine 較一般常見的含氟低表面能材料價格便宜且具有易於製程的優點。故本實驗為探討高分子 polybenzoxazine 表面能特性之應用，將以改變新的方法製備出以 polybenzoxazine 為主的超疏水表面。

本實驗則以 polybenzoxazine 為研究主體，研究內容分別為：

1. Polybenzoxazine 本身之低表面能特性研究

本研究室成功利用分子間與分子內作用力(氫鍵)來解釋高分子表

面能的變化。此一部分我們則就材料的表面能做學理的研究。

2. Polybenzoxazine 應用於能自清潔的超疏水表面(superhydrophobic and smart surface)之製備與原理探討

超疏水的定義為：水在物體表面的接觸角 (contact angle) 必須大於等於 150 度，且滾動角小於 10 度。物體表面具自清潔之功能是奈米科技時代廣為討論的課題，進行表面處理使其具備超疏水特性是科學家追求的目標。我們則利用噴砂的方法和加入光觸媒奈米粉體（$TiO_2$），使鋁材表面同時具有微米與奈米等級的粗糙結構，並達到像蓮花表面一樣的超疏水特性。我們亦運用最常拿來解釋超疏水現像的兩個學說，來對超疏水特性作學理上的探討。

3.氫鍵和高分子間的分佈對材料表面能量之影響

我們用簡單的熱處理方法可以得到一系列擁有極低的表面能的共聚物 poly(vinylphenol-co-methylmethacrylate)。 利用減少高分子間羟基所產生分子間氫鍵作用力原理產生較低表面能的高分子共聚物。 經由红外線分析指出在經過熱處理後，PVPh 段的羟基其所產生的分子間氫鍵轉換成自由羥基和羥基和羰基之間的分子內氫鍵,因而使得高分子的分子間氫鍵變小。 另外，我們也發現共聚物 poly(vinylphenol-co-methylmethacrylate)氫鍵的強度不僅與高分子的分佈有關且與在旋轉塗佈過程中溶液迅速蒸發速度有關。

# A Novel Low Surface Free Energy Material

# Polybenzoxazine Characterization and Applications for Superhydrophobic and Smart Surface Material

Postgraduate Student: Chang-Yuang Li  Adviser: Dr. Feng-Chih Chang

Department of Applied Chemistry

National Chiao Tung Universuty

## Abstract

In literature, we learned that most researchers add fluorinated functional groups to a given polymer to reduce its surface energy. The change of the surface energy of the polymer is due to the intermolecular and intramolecular force between polymers. Nevertheless, only few studies are related to this research area. Recently, we found that polybenzoxazine has extreme low surface energy which has significant influence on the chemical and physical properties of a polymer. Therefore, studying polybenzoxazine will give us better understanding of the low surface energy property.

Polybenzoxazine, due to its lower surface energy than Teflon, is a good alternative for superhydrophobic materials. Moreover, the cost and synthetic procedure of polybenzoxazine are less expensive and simpler than those of other fluorinated materials. In this research, I will study the low surface energy property and the application of polybenzoxazine. In addition, I will also develop new approach for

preparing polybenzoxazine for superhydrophobic materials.

:

**The objectives of my research are as follows:**

**1 The study of low surface energy property of polybenzoxazine:**

Our lab has already explained the change of polymer surface energy by intermolecular and intramolucular hydrogen bonding. This objective will extend the explanation of this property.

**2 The study and new preparation method of polybenzoxazine for smart and superhydrophobic surface:**

The definition of "Superhydrophobic Surface" is the water contact angle and the rolling angle must be larger than 150° and smaller than 10°respectively. The self-cleaning of the surface of objects is a hot subject in nanotechnology. We will apply sandblasting to create topographical microstructure on the surface of aluminum material. The surface-modified aluminum material is then coated by $TiO_2$ nanoparticles and polybenzoxazine. The resulting composite will have superhydrophobic property like lotus flower surface. Two theories will be used to explain the superhydorphobic property of this novel composite.

**3 Effect of Hydrogen Bonding and Sequence Distribution on Low-Surface-Energy Material of Poly (vinylphenol–co-methyl methacrylate)**

A series of poly(vinylphenol-co-methylmethacrylate) (PVPh-co-PMMA) block and random copolymers possessing extremely low surface energy can be obtained after a simple thermal treatment procedure. PVPh-co-PMMA copolymers result in a lower surface energy because of the decrease of intermolecular hydrogen bonding between hydroxyl groups. Infrared analyses indicate that the intermolecular hydrogen bonding of PVPh segment decreases by converting the hydroxyl group into a free hydroxyl and

increasing intramolecular hydrogen bonding and intermolecular hydrogen bonding between hydroxyls and carbonyls after thermal treatment. In addition, we also found that the hydrogen-bonding strength of poly(vinylphenol-co-methylmethacrylate) copolymers not only depended on sequence distribution but also the solvent casting process because of the rapid solvent evaporation during the spin casting process.

# Outline of Contents

# List of Tables

# List of Figures

# Chapter 1

# Introduction

## 1.1 Overview on Benzoxazines and Polybenzoxazines

A interesting addition-cure phenolic system is based on oxazine-modified phenolic resin that encounters a ring-opening polymerization to give polybenzoxazine, which is mainly a poly(amino-phenol). The benzoxazine monomers are formed from amines and phenol in the presence of formaldehyde, which were first synthesized by Holly and Cope [1]. These structures were not recognized as phenolic resin precursors until Schreiber [2] reported in 1973 that a hard and brittle phenolic material was formed from benzoxazine precursors, but no further details about structures and properties were included. In 1986, Riess et al. reported the synthesis and reactions of monofunctional benzoxazine compound. [3] The compounds that they obtained were oligomer phenolic structures because the thermo-dissociation of the monomer was always competing with the chain propagation. The bifunctional benzoxazine precursor synthesized by Ning and Ishida [4] overcame the low degree of crosslinking of above compounds. Furthermore, these samples possess high mechanical integrity and an be easily prepared from inexpensive raw materials.[5-7]

In phenolic chemistry, both the ortho- and para- position on the benzene ring are reactive toward electrophilic substitution reactions due to the directing effect of the hydroxyl group. Benzoxazines also show multiple reactivities of the benzene ring due to directing effect of both the alkoxyl and alkyl groups connected to the benzene ring as shown in Scheme 1-1. Benzoxazines can be polymerized without by using strong acid or basic catalyst, and produce no byproducts through the heterocyclic ring opening reaction. The free ortho- position on a benzene ring in the benzoxazine

system has high reactivity toward thermal and phenol-initiated ring-opening polymerizations and forms a phenolic Mannich base (-$CH_2$-NR-$CH_2$-) polymer structure. In addition, the free para- position also shows reactivity toward a similar type of polymerization [3,8].

The ring-opening polymerization can also be catalyzed by acidic catalysts that permit a wide curing temperature. In the presence of acidic catalysts [9], the curing temperature can be reduced from 160-220 °C to about 130-170 °C and increase the application range. In recent years, thermosetting polybenzoxazines have attracted an intense amount of interest from both academia and industry because of their fascinating characteristics, such as high performance, low cost, and ease of processing.[10-13]

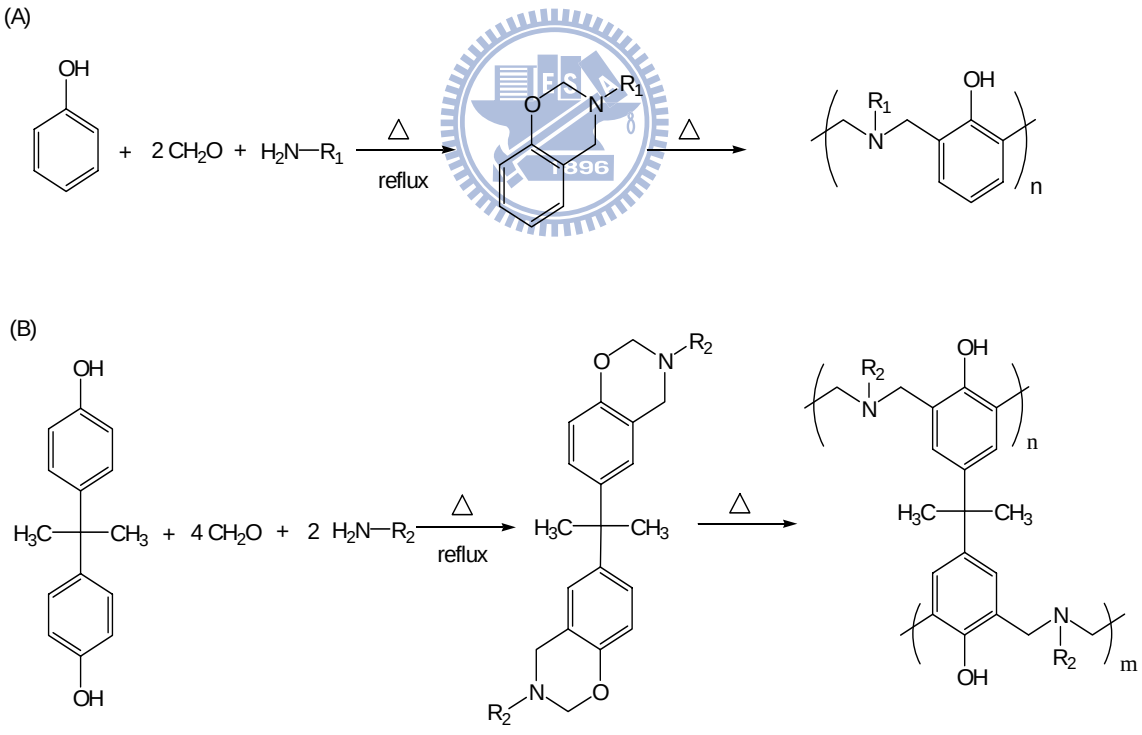


Scheme 1-1. The synthese and thermal curing of (A) monofunctional benzoxazines and (B) difunctional benzoxazines

In addition to these advantageous features, which they share with traditional phenolic resins, the polybenzoxazines also possess unique properties, such as low degrees of water absorption [14,15] (despite the large number of hydroxyl groups present in their backbone structure), high moduli, [16] excellent resistance to chemicals [17] and UV light, [18] near-zero volumetric shrinkage/expansion upon polymerization, [19] and high glass transition temperatures, even at a relatively low cross-linking density. [20] The polybenzoxazines overcome several defects of traditional novolac and resole-type phenolic resins, while retaining their advantages. Polybenzoxazine resins are supposed to replace traditional phenolics, polyesters, vinyl esters, epoxies, cyanate esters and polyimides in many respects. [21] In addition, our lab discovered, to our surprise, that polybenzoxazines also can possess surface free energies even lower than that of pure poly(tetrafluoroethylene) (Teflon).The lowest surface free energies that we observed for the BA-a polybenzoxazine and BA-m polybenzoxazine systems were 19.2 and 16.4 $mJ/m^2$, respectively. Both of these values are lower than that of pure Teflon (21 $mJ/m^2$). [22] And the molecular structure of polybenzoxazine offers excellent design flexibility that allows properties of the cured material to be controlled for specific requirements of a wide variety of individual requirements. The resin allows development of new applications by utilizing some of their unique features such as [19, 20-23]:

- Near zero volumetric change upon polymerization
- No release of volatiles during curing
- Low melting viscosity (for benzoxazine)
- High glass transition temperature ($T_g$)
- High thermal stability ($T_d$)
- Low Surface Free Energy

- Low water absorption
- Good mechanical properties
- Excellent electrical properties

Table 1-1 compares the properties of polybenzoxazine with those of the state-of the-art matrices. The relative benefits of polybenzoxazines are obvious.

Table 1-1 Comparative polybenzoxazine properties of various high performance polymers

| Property | Epoxy | Phenolics | Toughened BMI | Bisox–phen (40:60) | Cyanate ester | P–T resin | Polybenzoxazine |
|---|---|---|---|---|---|---|---|
| Density (g/cc) | 1.2–1.25 | 1.24–1.32 | 1.2–1.3 | 1.3 | 1.1–1.35 | 1.25 | 1.19 |
| Max use temperature (°C) | 180 | 200 | ~200 | 250 | 150–200 | 300–350 | 130–280 |
| Tensile strength (MPa) | 90–120 | 24–45 | 50–90 | 91 | 70–130 | 42 | 100–125 |
| Tensile modulus (GPa) | 3.1–3.8 | 03/05 | 3.5–4.5 | 4.6–5.1 | 3.1–3.4 | 4.1 | 3.8–4.5 |
| Elongation (%) | 3–4.3 | 0.3 | 3 | 1.8 | 02/04 | 2 | 2.3–2.9 |
| Dielectric constant (1 MHz) | 3.8–4.5 | 04/10 | 3.4–3.7 | – | 2.7–3.0 | 3.1 | 3–3.5 |
| Cure temperature (°C) | RT–180 | 150–190 | 220–300 | 175–225 | 180–250 | 177–316 | 160–220 |
| Cure shrinkage (%) | >3 | 0.002 | 0.007 | <1 | ~3 | ~3 | ~0 |
| TGA onset (8C) | 260–340 | 300–360 | 360–400 | 370–390 | 400–420 | 410–450 | 380–400 |
| Tg (°C) | 150–220 | 170 | 230–380 | 160–295 | 250–270 | 300–400 | 170–340 |
| $G_{IC}$ (J/m$^2$) | 54–100 | – | 160–250 | 157–223 | – | – | 168 |
| $K_{IC}$ (MPa m$^{1/2}$) | 0.6 | – | 0.85 | – | – | – | 0 |

## 1.2 Effect of Hydrogen Bonding on Low-Surface-Energy Material

The performance of polymeric materials is often dictated by surface properties, such as wettability, friction, and adhesion. In particular, hydrophobicity and oleophobicity have attracted tremendous interest due to their wide range of applications [24-27]. Both poly(dimethylsiloxane) (PDMS) and poly(tetrafluoroethylene) (PTFE) are two well-known examples possessing low surface energies. [28-31] PTFE may be regarded as the benchmark lower surface energy material, displaying water repellency [32] in combination with other desirable properties. [33] The small size of the fluorine atom with high electronegativity, low polarizability, and strong fluorine-fluorine repulsion [34] results in weak intermolecular forces of fluorinated polymer chains and thus relatively lower surface energies. However, PTFE and many fluorinated polymers have some application limitations such as high cost and poor processibility. Many efforts have been attempted to search for low-surface-free-energy polymeric materials with low cost, easy processibility, and good film-forming characteristics. [35-37]

Hydrogen bonding plays an important role in determining the surface properties of polymers. In general, the amorphous comblike polymers possessing a flexible linear backbone on the side chain with low intermolecular interaction exhibit a low surface energy. [38] We have found that the intermolecular hydrogen bonding between the hydroxyl groups increases their surface energies in the polybenzoxazine system[35]. Jiang et al[39] found that at temperatures above its lower critical solution temperature (LCST), the compact, collapsed conformation of poly(N-isopropylacrylamide) (PNIPAAm), induced by intramolecular hydrogen bonding between the C=O and N-H groups of the main chains results in a low surface free energy and a high contact angle

for water. When the temperature is below the LCST, however, intermolecular hydrogen bonding between the PNIPAAm main chains and water molecules predominates leading to a higher surface free energy and a lower water contact angle. Similarly, Chung et al. [40] reported that the presence of amide groups in a fluorinated-main-chain liquid-crystalline polymer system induces strong intermolecular hydrogen bonding resulting in higher surface free energies and higher degrees of hydrophilicity. The nature of the pendent chain has a most profound effect in determining the surface energy of the material; therefore, a low-surface-free-energy material can be obtained by decreasing the intermolecular interaction from the comblike polymer with a flexible linear backbone. [41] In our previous study[42], we discovered that PVPh, a fluorine- and silicone-free polymer, can possess an extremely low surface energy (15.7 $mJ/m^2$) after a simple thermal treatment procedure which is even lower than that of PTFE (22.0 $mJ/m^2$) calculated on the basis of the two-liquid geometric method. Besides, the sequence distribution of the vinyl phenol group in PVPh-*co*-PS copolymers plays an important role in dictating the final surface energy after thermal treatment. In this paper, we found that the PVPh-co-PMMA copolymers presents quiet different surface properties from PVPh-co-PS coplymers after thermal treatment. Furthermore, we discovered that the fraction of hydrogen bonding between vinylphenol groups and carbonyl groups not only depended on the sequence distribution of the vinylphenol group in PVPh-co-PMMA copolymers but also the casting process. The effects of molecule weight on surface free energy were also investigated carefully.

## References


[1] F. W. Holly, A. C. Cope, *J. Am. Chem. Soc.* **1944**, *66*, 1875.

[2] Scheriber, H. Ger, *Offen*. 2225504, **1973**; *Offen*. 2323936, **1973**.

[3] Riess, G.; Schwob, J. M.; Guth, G.; Roche, M.; Lande, B. in "Advances in Polymer Science" (Eds B. M. Culbertson and J. E. Mcgrath), Plenum, New York, **1986**.

[4] Ning, X.; Ishida, H. *J. Polym. Sci., Polym. Phys. Ed.* **1994**, *32*, 921.

[5] Ishida, H. *J. Appl. Polym. Sci.* **1995**, *58*, 1751.

[6] Burke, W. J.; Murdoch, K. C.; Ec, G. *J. Am. Chem. Soc.* **1954**, *76*, 1677.

[7] Burke, W. J.; Glennie, E. L. M.; Weatherbee, C. *J. Org. Chem.***1964**, *24*, 909.

[8] Shen, S. B.; Ishida, H. *J. Appl. Polym. Sci* .**1996**, *61*, 1595.

[9] Dunkers, J.; Ishida, H. *J. Polym. Sci. Part A: Polym. Chem.* **1999**, *37*, 1913.

[10] X. Ning,; H. Ishida, *J. Polym. Sci., Part A: Polym. Chem.* **1994**, *32*, 1121.

[11] T. Takeichi, I. Komiya, Y. Takayama, *Kyoka-Purasutikkus* (in Japanese) **1997**, *43*, 109.

[12] Y. X. Wang, H. Ishida, *Polymer* **1999**, *40*, 4563.

[13] J. A. Macko, H. Ishida, *Polymer* **2001**, *42*, 227.

[14] N. Furukawa, *Benzoxazine-based thermosetting polymers and their manufacture, compositions, and heat- and fire-resistant dielectric cured products with low water absorption.* Jpn. Kokai Tokkyo Koho, **2004**, p18.

[15] Y. X. Wang, H. Ishida, *Polym. mater. sci. eng.* **1999**, *80*, 211.

[16] H. Ishida, D. J. Allen, *J. Polym. Sci., Part B: Polym. Phys.* **1996**, *34*, 1019.

[17] H. D. Kim, H. Ishida, *J. Appl. Polym. Sci.* **2001**, *79*, 1207.

[18] J. Macko, H. Ishida, *J. Polym. Sci., Part B: Polym. Phys.* **2000**, *38*, 2687.

[19] H. Ishida, H. Y. Low, *Macromolecules* **1997**, *30*, 1099.

[20] H. Ishida, Y. Rodriguez, *Polymer* **1995**, *36*, 3151.

[21] Chih-Feng Wang, Yi-Che Su, Shiao-Wei Kuo, Chih-Feng Huang, Yuung-Ching Sheen and Feng-Chih Chang,*Angew. Chem. Int. Ed.* **2006**, *45*, 2248.

[22] C. P. R. Nair, *Prog. Polym. Sci.* **2004**, *29*, 401.

[23] T. Agag, T. Takeichi, *Macromolecules* **2001**, *34*, 7257.

[24] Li, H.; Wang, X.; Song, Y.; Liu, Y.; Li, Q.; Jiang, L.; Zhu, D. *Angew. Chem. Int., Ed*. **2001**, 40, 1743.

[25] Aussillous, P.; Quere, D. *Nature* **2001**, 411, 924.

[26] Shirtcliffe, N. J.; McHale, G.; Newton, M. I.; Perry, C. C. *Langmuir* **2005**, 21, 937.

[27] Wang, S.; Feng, L.; Liu, H.; Sun, T.; Zhang, X.; Jiang, L.; Zhu, D. *ChemPhysChem* **2005**, 6, 1475.

[28] Coulson, S. R.; Woodward, I.; Badyal, J. P. S.; Brewer, S. A.; Willis, C. *J. Phys. Chem. B* **2000**, 104, 8836.

[29] Jin, M.; Feng, X.; Xi, J.; Zhai, J.; Cho, K.; Feng, L.; Jiang, L. *Macromol. Rapid Commun.* **2005**, *26*, 1805.

[30] Feng, L.; Zhang, Z.; Mai, Z.; Ma, Y.; Liu, B.; Jiang, L.; Zhu, D. *Angew. Chem.*, Int. Ed. **2004**, 43, 2012.

[31] Hillborg, H.; Tomczak, N.; Olah, A.; Schonherr, H.; Vancso, G. *J. Langmuir* **2004**, 20, 785.

[32] Wu, S. *Polymer Interface and Adhesion*; Marcel Dekker: New York, **1982**.

[33] Feiring, A. E.; Imbalzano, J. F.; Kerbow, D. L. *Adv. Fluoroplast. Plast. Eng.* **1994**, 27.

[34] Carlson, D. P.; Schmiegel, W. Ullmann's Encyclopedia of Industrial Chemistry; VCH Verlagsgesellschaft: Weinheim, Germany, **1988**; p 393.

[35] Wang, C. F.; Su, Y. C.; Kuo, S. W.; Huang, C. F.; Sheen, Y. C.; Chang, F. C. *Angew. Chem., Int. Ed*. **2006**, 45, 2248

[36] Kobayashi, H.; Owen, M. J. Trends *Polym. Sci.* **1995**, 3, 5.

[37] Schmidt, D. L.; Coburn, C. E.; DeKoven, B. M.; Potter, G. E.; Meyers, G. F.; Fischer, D. A. *Nature* **1994**, 368, 41.

[38] Owen, M. J. Comments *Inorg. Chem.* **1988**, 7, 195.

[39] Sun, T.; Wang, G.; Feng, L.; Liu, B.; Ma, Y.; Jiang, L.; Zhu, D. *Angew. Chem. Int. Ed*. **2004**, 43,357-360.

[40] Ma, K. X.; Chung, T. S. *J. Phys. Chem. B* **2001**, 105, 4145-4150.

[41] Tsibouklis, J.; Graham, P.; Eaton, P. J.; Smith, J. R.; Nevell, T, G.; Smart, J. D.; Ewen, R. *J. Macromolecules* **2000**, 33, 8460.

[42] Lin, H. C.; Wang, C. F.; Kuo, S. W.; Tung, P. H.; Huang, C. F.; Lin, C. H.; Chang, F. C. *J. Phys. Chem. B* **2007**, 111, 3404.

# Chapter 2

# The Study of Theory

## 2.1 Surface Free Energy

As everyone knows , nanomaterial science and engineering already becomes world research focuses.While studying the surface characteristic of nanomaterial, it often involves this concept of the surface energy and contact angle. This section of articles are proving theory and researches of the surface free energy and contact angle .

### 2.1.1 Interfacial Thermodynamics

The interface (surface) is a region of finite thickness (usually less than 0.1 μm) in which the composition and energy very continuously from one bulk phase to other. The pressure (force field) in the interfacial zone is therefore nonhomogeneous, having a gradient perpendicular to the interfacial boundary. In contrast, the pressure in a bulk phase is homogeneous and isotropic. Consequently, no net energy is expended in reversibly transporting the matter within a bulk phase. However, a net energy is required to create an interface by transporting from the bulk phase to the interfacial zone. The reversible work require to create a unit surface area is the surface free energy, that is,

$$\gamma = \left( \frac{\partial G}{\partial A} \right)_{T,\, P,\, n} \tag{2.1}$$

where $\gamma$ is the surface free energy, G the Gibbs free energy of the total system, A the interfacial area, T the temperature, P the pressure, and n the total number of moles of matter in the system.

The work require to separate reversibly the interface between two bulk phases

$\alpha$ and $\beta$ form their equilibrium separation to infinity is the work of adhesion.

$$W_a = W_{\alpha\beta} = \gamma_\alpha + \gamma_\beta - \gamma_{\alpha\beta} \quad (2.2)$$

Where $W_a$ is the work of adhesion, $\gamma_\alpha$ the surface free energy of phase $\alpha$, $\gamma_\beta$ the surface free energy of phase $\beta$, and $\gamma_{\alpha\beta}$ the interfacial energy between phase $\alpha$ and $\beta$ (Figure 2-1).

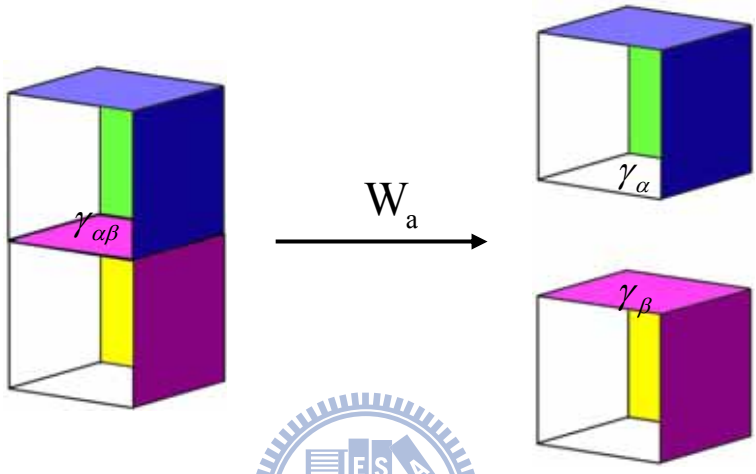


Figure 2-1. Work of adhesion.

This was apparently first purpose by Dupré.[1] When the two phase are identical, the reversible work is the work of cohesion (Figure 2-2),

$$W_c = W_{jj} = \gamma_j + \gamma_j - 0 = 2\gamma_j \quad (2.3)$$

where $W_c$ is the work of cohesion for phase j.

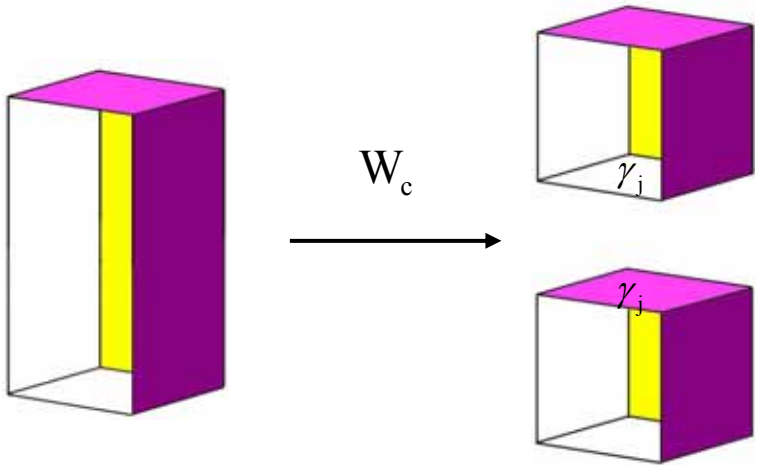


Figure 2-2. Work of cohesion.

The work of adhesion is the decrease of Gibbs free energy per unit area when an interface is formed from two individual surfaces. Thus, the greater the interfacial attraction, the greater the work of adhesion will be. Rearrangement of Eq. (2.1) gives

$$\gamma_{\alpha\beta} = \gamma_{\alpha} + \gamma_{\beta} - \mathrm{W_a} \tag{2.4}$$

indicating that the greater the interfacial attraction, the smaller the interfacial energy will be. The works of adhesion can be related to the cohesion theoretically. Thereby, the interfacial energy can be linked to the properties of the two individual phases.

Thermodynamic discussions of adhesion in solid-liquid systems should be carried out in terms of surface free energy rather than surface tension. Discussions that involve the shape of liquid-gas or liquid-liquid interfaces can be carried out either in terms of surface tension or surface free energy.

### 2.1.2 Contact Angle Equilibrium: Young Equation

A liquid in contact with a solid will exhibit a contact angle (Figure 2-3). If the system is at rest, a static contact angle is obtained. If the system is in motion, a dynamic contact angle is obtained. Here, static contact angles are discussed. A system at rest may be in stable equilibrium (the lowest energy state), or in meta stable equilibrium ( an energy through separated from neighboring states by energy barriers).

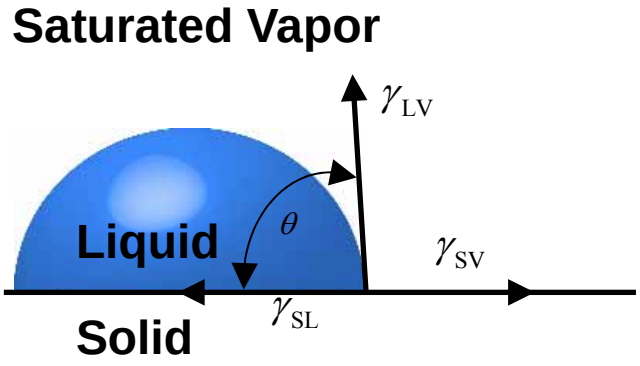

Figure 2-3. Contact angle equilibrium on a smooth, homogeneous, planar, and rigid surface

Stable equilibrium will be obtained if the solid surface is ideally smooth, homogeneous, planar, and nondeformable; the angle formed is the equilibrium contact angle, $\theta$.

On the other hand, if the solid surface is rough or compositionally heterogeneous, the system may reside in one of many stable states; the angle formed is a metastable contact angle. The amount of mechanical energy in the liquid drop (such as vibrational energy) determines which metastable state is to be occupied. Therefore, metastable contact angle vary with drop volume, external mechanical energy (such as vibration), and how the angle is formed ( whether by advancing or receding the liquid front on the solid). The stable equilibrium contact angle may sometimes (but rarely) be observed on a rough or heterogeneous surface. This equilibrium angle corresponds to the lowest energy state.

The angle formed by advancing the liquid front on the solid is termed advancing contact angle, $\theta_a$ (Figure 2-4). The angle formed by receding the liquid front on the solid is termed receding contact angle, $\theta_r$ (Figure 2-5).

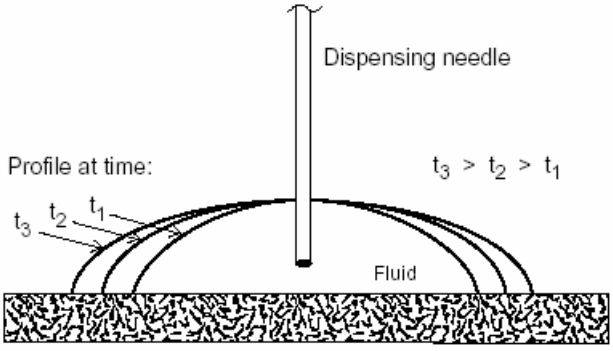

Figure 2-4. Advancing contact angle

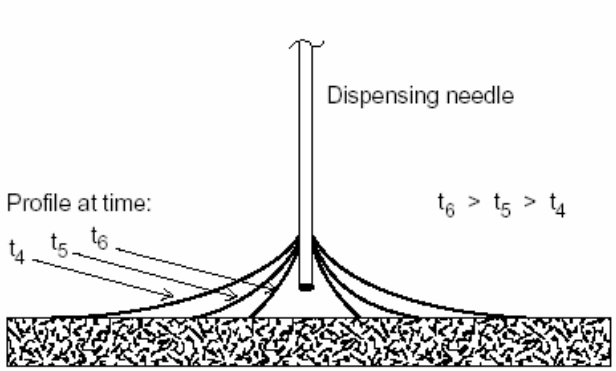


Figure 2-5. Receding contact angle

Advancing contact angle are usually greater than receding contact angle when the system is in a metastable state. On the other hand, the advancing and the receding angles are identical when equilibrium angles are formed. Many real surfaces are rough or heterogeneous. Thus, variable contact angles are often observed. This has previously led to concern as to whether is a true thermodynamic quality. The origin of variable contact angle has now been clearly established and the thermodynamic status of contact angle ascertained.

The equilibrium contact angle (abbreviated $\theta$ here) for liquid drop on an ideally smooth, homogeneous, planar, and nondeformable surface (Figure 2-3) is related to the various interfacial tension by

$$\gamma_{LV}\cos\theta = \gamma_{SV} - \gamma_{SL} \qquad (2.5)$$

where $\gamma_{LV}$ is the surface tension of the liquid in equilibrium with its saturated vapor, $\gamma_{SV}$ the surface free energy of the solid in equilibrium with the saturated vapor of the liquid, and $\gamma_{SL}$ the interfacial tension between the solid and the liquid. This is known as the Young equation. Young [2] described the relation in words, and did not attempt to prove it. Several proofs were offered later by others. [3-5]

Many real surfaces are rough or heterogeneous. A liquid drop resting on such a surface may reside in the stable equilibrium (the lowest energy state), or in a metastable equilibrium (energy trough separated from neighboring states by energy barriers). The equilibrium contact angle $\theta_e$ corresponds to the lowest energy state for a system. On an ideally smooth and compositionally homogeneous surface, the equilibrium contact angle is the Young's angle $\theta_Y$, which is also the microscopic local contact angle on any rough or heterogeneous surface, hence also known as the intrinsic contact angle $\theta_0$. The fact that $\theta_0$ equals $\theta_Y$ has been proved theoretically as the condition for minimization of system free energy.

The equilibrium contact angle on a rough surface is Wenzel's angle $\theta_W$. The equilibrium contact angle on a heterogeneous surface is Cassie's angle $\theta_C$. These angles correspond to the lowest energy state, but are often not observed experimentally. Instead, the system often resides in a metastable state, exhibiting a metastable contact angle. In this case, advancing and receding angles are different, known as hysteresis (H). The different $\theta_a - \theta_r$ is the extent of hysteresis.

### 2.1.3 Determination of Surface Free Energy

The surface free energy of a solid polymer cannot be measured directly, as reversible formation of its surface is difficult. Many indirect method have been proposed, including the polymer melt (temperature dependence) method, Good–Girifalco Method, Owens, Wendt, and Kaelble's Method (Two-Liquid Geometric Method), Wu's Method (Two-Liquid Harmonic Method), Lifshitz–van der Waals Acid-Base Theory (Three-Liquid Acid-Base Method), critical surface tension and others.

**Good–Girifalco Method**

Good and Girifalco in the 1950s proposed the following equation to describe the surface energy of interfacial phase systems: [6-8]

$$\gamma_{ab} = \gamma_a + \gamma_b - 2\Phi(\gamma_a\gamma_b)^{1/2} \tag{2.6}$$

The subscripts a and b refer to the two phases, which may be liquid or solid. $\Phi$ is a constant between interfaces of a system and is defined as:

$$-\frac{\Delta F_{ab}^{a}}{(\Delta F_a^c \Delta F_b^c)^{1/2}} = \Phi \tag{2.7}$$

where $\Delta F_{ab}^{a}$ = the free energy of adhesion for the interface between phases A and B, per cm$^2$, $= \gamma_{ab} - \gamma_a - \gamma_b$ and $\Delta F_n^c$ = free energy of cohesion for phase N $= 2\gamma_n$. Equation (2.6) can be rewritten as the well known Good and Girifalco equation:

$$\gamma_{SL} = \gamma_S + \gamma_{LV} - 2\Phi(\gamma_S\gamma_{LV})^{1/2} \tag{2.9}$$

Combined equations 2.5 and 2.9 yield:

$$\gamma_{LV}(1+\cos\theta) = 2\Phi(\gamma_S\gamma_{LV})^{1/2} \tag{2.10}$$

Or

$$\gamma_S = \frac{\gamma_{LV}(1+\cos\theta)^2}{4\Phi^2} \tag{2.11}$$

Suppose the value of $\Phi$ is known for a pair of the testing solid and liquid, $\gamma_S$ can be calculated from contact angle data with eq. (2.11). In the zeroth order approximation, Good and Girifalco suggested that $\Phi$ was equal to unity.

**Fowkes' Method**

Fowkes [9,10] proposed that "the surface tensions are a measure of the attractive forces between surface layers and liquid phase, and that such forces and

their contribution to the free energy are additive." He designated, in the case of the surface tension of water, the surface tension could be considered the sum of contributions from dispersion forces ($\gamma^d$) and dipole interactions, mainly hydrogen bonds ($\gamma^h$):

$$\gamma_{H_2O} = \gamma^d_{H_2O} + \gamma^h_{H_2O} \tag{2.12}$$

where superscript h refers to hydrogen bonding, and d to dispersion. In addition, at the interface between a liquid and solid, as Fowkes pointed out, the interfacial molecules are attracted by the bulk liquid from one side and from the other side by the intermolecular forces between the two phases. Fowkes defined the dispersion force contribution to surface tension of the solid in terms of the interaction with the dispersion forces of the liquid. As a result, the Young–Good–Girifalco equation can be modified as:

$$\gamma_{SL} = \gamma_S + \gamma_{LV} - 2(\gamma^d_S \gamma^d_{LV})^{1/2} \tag{2.13}$$

Combine eqs. (2.5) and (2.13) results in:

$$\gamma_{LV}(1+\cos\theta) = 2(\gamma^d_S \gamma^d_{LV})^{1/2} \tag{2.14}$$

Strictly speaking, eq. (2.14) provides a method to estimate the value of $\gamma^d_S$, but not total $\gamma_S$, from a single contact angle measurement, where only dispersion forces operate in the liquid, such as a hydrocarbon liquid. The $\gamma^d_S$ of any solid can be determined using a "dispersion force only" liquid.

**Owens, Wendt, and Kaelble's Method**

**(Two-Liquid Geometric Method)**

Owens and Wendt [11] and Kaelble [12] extended Fowkes' equation to a more general form:

$$\gamma_{SL} = \gamma_S + \gamma_{LV} - 2(\gamma_S^d \gamma_{LV}^d)^{1/2} - 2(\gamma_S^p \gamma_{LV}^p)^{1/2} \quad (2.15)$$

Combine eqs. (2.5) and (2.15) yield:

$$\gamma_{LV}(1+\cos\theta) = 2(\gamma_S^d \gamma_{LV}^d)^{1/2} + 2(\gamma_S^p \gamma_{LV}^p)^{1/2} \quad (2.16)$$

where superscript d refers to a dispersion (nonpolar) component, and p refers to a polar (nondispersion) component, including all the interactions established between the solid and liquid, such as dipole– dipole, dipole-induced dipole and hydrogen bonding, etc.

Since $\gamma_S$ is the sum of surface tension components contributed from dispersion and polar parts:

$$\gamma_S = \gamma_S^d + \gamma_S^p \quad (2.17)$$

Equations (2.15) and (2.16) provide a method to estimate surface tension of solids. Using two liquids with known $\gamma_L^d$ and $\gamma_L^p$ for contact angle measurements, one could easily determine $\gamma_S^d$ and $\gamma_S^p$ by solving the following two equations:

$$\gamma_{LV1}(1+\cos\theta_1) = 2(\gamma_S^d \gamma_{LV1}^d)^{1/2} + 2(\gamma_S^p \gamma_{LV1}^p)^{1/2}$$

$$\gamma_{LV2}(1+\cos\theta_2) = 2(\gamma_S^d \gamma_{LV2}^d)^{1/2} + 2(\gamma_S^p \gamma_{LV2}^p)^{1/2} \quad (2.18)$$

The values of $\gamma_L^d$ and $\gamma_L^p$ of reference liquids have been provided by Kaelble.

**Wu's Method**

**(Two-Liquid Harmonic Method)**

This method uses the contact angles of two testing liquids and the harmonic-mean equation. The result agree remarkable well with the liquid homolog method, polymer melt method, and the equation of state method.

Based on “harmonic” mean and force addition, Wu proposed the following equations: [13,14]

$$\gamma_{SL} = \gamma_S + \gamma_{LV} - \frac{4\gamma_S^d \gamma_{LV}^d}{\gamma_S^d + \gamma_{LV}^d} - \frac{4\gamma_S^p \gamma_{LV}^p}{\gamma_S^p + \gamma_{LV}^p} \tag{2.19}$$

Equation (2.19) can be written as follows with the aid of eq. (2.5):

$$\gamma_{LV}(1+\cos\theta) = \frac{4\gamma_S^d \gamma_{LV}^d}{\gamma_S^d + \gamma_{LV}^d} + \frac{4\gamma_S^p \gamma_{LV}^p}{\gamma_S^p + \gamma_{LV}^p} \tag{2.20}$$

Equations (2.19) and (2.20) provide a method to estimate surface tension of solids. Using two liquids with known $\gamma_L^d$ and $\gamma_L^p$ for contact angle measurements, one could easily determine $\gamma_S^d$ and $\gamma_S^p$ by solving the following two equations:

$$\gamma_{LV1}(1+\cos\theta) = \frac{4\gamma_S^d \gamma_{LV1}^d}{\gamma_S^d + \gamma_{LV1}^d} + \frac{4\gamma_S^p \gamma_{LV1}^p}{\gamma_S^p + \gamma_{LV1}^p}$$

$$\gamma_{LV2}(1+\cos\theta) = \frac{4\gamma_S^d \gamma_{LV2}^d}{\gamma_S^d + \gamma_{LV2}^d} + \frac{4\gamma_S^p \gamma_{LV2}^p}{\gamma_S^p + \gamma_{LV2}^p} \tag{2.21}$$

Wu [13] claimed that this method applied accurately between polymers and between a polymer and an ordinary liquid.

**Lifshitz–van der Waals Acid-Base Theory**

**(Three-Liquid Acid-Base Method)**

Van Oss et al. has proposed a methodology that represents both Fowkes–Owens–Wendt–Kaelble and Wu. This methodology introduces a new meaning of the concepts, “apolar” and “polar,” the later cannot be represented by a single parameter such as $\gamma^p$.

As shown in eq. (2.22), surface tension $\gamma$ could be divided into an apolar component and a hydrogen bonding component or (more generally) acidbase

interaction. One may follow Fowkes' approach [15,16] and separate surface energy into several components as:

$$\gamma = \gamma^{d} + \gamma^{dip} + \gamma^{ind} + \gamma^{h} + \ldots \tag{2.22}$$

$$\gamma = \gamma^{d} + \gamma^{AB} \tag{2.23}$$

where the superscripts, d, dip, ind, and h refer to (London) dispersion, (Keesom) dipole– dipole, (Debye) induction, and hydrogen bonding forces, respectively. And the superscript AB refers to the acid-base interaction.

By regrouping components in eq. 2–22, van Oss and Good expressed the surface energy as:

$$\gamma = \gamma^{LW} + \gamma^{AB} \tag{2.24}$$

$$\gamma^{LW} = \gamma^{d} + \gamma^{dip} + \gamma^{ind} \tag{2.25}$$

where LW stands for Lifshitz–van der Waals. Because a hydrogen bond is a proton-sharing interaction between an electronegative molecule or group and an electropositive hydrogen, a hydrogen bonding is an example of Lewis acid (electron acceptor) and Lewis base (electron donor). Van Oss et al., [17-23] therefore, treated hydrogen bonding as Lewis acid-base interactions. In addition, van Oss et al. [17- 19] created two parameters to describe the strength of Lewis acid and base interactions:

$\gamma^{+}$ = Lewis acid parameter of the surface free energy

$\gamma^{-}$ = Lewis base parameter of the surface free energy

$$\gamma^{AB} = 2\sqrt{\gamma^{+}\gamma^{-}} \tag{2.26}$$

Based on these definitions, a material is classified as a bipolar substance if both its $\gamma^{+}$ and its $\gamma^{-}$ are greater than 0 ($\gamma^{AB} \neq 0$). In other words, it has both nonvanishing $\gamma^{+}$ and $\gamma^{-}$. A monopolar material is one having either an acid or a base characters, which means either $\gamma^{+} = 0$ and $\gamma^{-} > 0$ or $\gamma^{+} > 0$ and $\gamma^{-} = 0$. An

apolar material is neither an acid nor a base (both its $\gamma^+$ and its $\gamma^-$ are 0). For both monopolar and apolar materials, their $\gamma^{AB} = 0$. Therefore, according to the Fowkes notation, the criterion for a substance to be apolar, is, $\gamma^{AB} = 0$. This is not true in the van Oss and Good's methodology.

How do we calculate these surface energy parameters? van Oss, Good, and their coworkers, have developed a "three-liquid procedure" (Equation 2.27) to determine $\gamma_S$ by using contact angles techniques and a traditional matrix scheme.

$$\gamma_{LV1}(1+\cos\theta_1) = 2(\sqrt{\gamma_S^{LW}\gamma_{LV1}^{LW}} + \sqrt{\gamma_S^+\gamma_{LV1}^-} + \sqrt{\gamma_S^-\gamma_{LV1}^+})$$

$$\gamma_{LV2}(1+\cos\theta_2) = 2(\sqrt{\gamma_S^{LW}\gamma_{LV2}^{LW}} + \sqrt{\gamma_S^+\gamma_{LV2}^-} + \sqrt{\gamma_S^-\gamma_{LV2}^+})$$

$$\gamma_{LV3}(1+\cos\theta_3) = 2(\sqrt{\gamma_S^{LW}\gamma_{LV3}^{LW}} + \sqrt{\gamma_S^+\gamma_{LV3}^-} + \sqrt{\gamma_S^-\gamma_{LV3}^+}) \quad (2.27)$$

In short, to determine the components of $\gamma_S$ of a polymer solid, it was recommended [24,25] to select three or more liquids from the reference liquids table, with two of them being polar, the other one being apolar. Moreover, the polar pairs—water and ethylene glycol, and water and formamide— were recommended to give good results, while aploar liquids are either diiodomethane or a-bromonaphthalene. Because the LW, Lewis acid, and Lewis base parameters of $\gamma_{LV1}$, $\gamma_{LV2}$, and $\gamma_{LV3}$ are available, one can determine the LW, Lewis acid, and base parameters of $\gamma_S$ by solving these three equations simultaneously.

**Critical Surface Tension – Zisman plot**

The concept of critical surface tension was first proposed by Fox and Zisman [26-28]. An empirical rectilinear relation was found between $\cos\theta$ and $\gamma_{LV}$ for a series of testing liquid on a given solid. When homogeneous liquids are used as the

testing liquids, a straight line is often obtained. When nonhomologous liquids are used, however, the data are often scattered within a rectilinear band or give a curved line.

The intercept of the line at $\cos\theta = 1$ is the critical surface tension $\gamma_c$. When a band is obtained, the intercept of lower line of the band is defined as the critical surface tension. The $\cos\theta$ versus $\gamma_{LV}$ plot is known as the Zisman plot. The example is given in Figure 2-6.

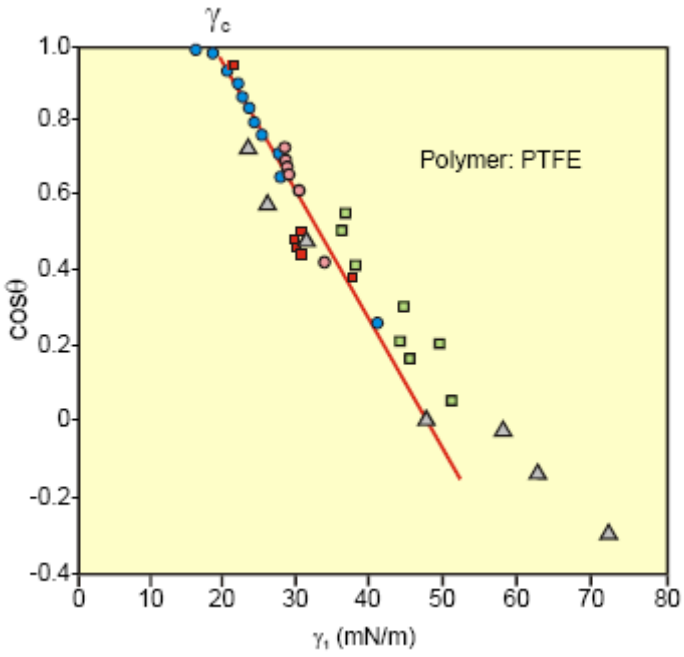


Figure 2-6. Zisman plot for poly(tetrafluoroethylene) (PTFE) using various testing liquids.

### 2.1.4 Surface Free Energy of Polymer

**Molecular-Weight Dependence**

The surface free energy of homologous series tends to increase, while the surface entropy tends to decrease, with increasing molecular weight. At infinite

molecular weight, both the surface free energy and the surface entropy are, however, finite.

The surface free energy of homologous series varies linearly with $M_n^{-2/3}$, [29,30]

$$\gamma = \gamma_\infty - \frac{k_e}{M_n^{2/3}} \tag{2.28}$$

where $\gamma_\infty$ is the surface free energy at infinite molecular weight and $k_e$ is a constant. This equation fits the data for n-alkanes with standard deviations in $\gamma$ about 0.05 dyne/cm, and for prefluoroalkanes, polyisobutylenes, polydimethylsiloxanes, and polystyrenes with standard deviations in $\gamma$ about 0.2 dyne/cm (Table 2-1).

Table 2-1. Numerical constant for molecular weight dependence of surface free energy.

| polymer | Temp. ℃ | $\gamma_\infty$ dyne/cm | $k_e$ | $\sigma$ [a] |
|---|---|---|---|---|
| n-alkanes | 20 | 37.81 | 385.9 | 0.03 |
| Polyisobutylenes | 24 | 35.62 | 382.7 | 0.34 |
| Polydimethylsiloxanes | 20 | 21.26 | 166.1 | 0.09 |
| Prefluoroalkanes | 20 | 25.85 | 682.8 | 0.30 |
| Polystyrenes | 176 | 29.97 | 372.7 | 0.08 |
| Poly(ethylene oxide)-dimethyl ether | 24 | 44.35 | 342.8 | 0.44 |

[a] $\sigma$ is the standard deviations in $\gamma$

The surface free energy variation decreases with increasing molecular weight. The $k_e$ values in Table 2-1 indicate that $\gamma$ will be smaller than $\gamma_\infty$ by less than 1 dyne/cm when the molecular weight is greater about 3000. Accordingly, for instance,

the surface free energy of poly(vinyl acetate) melts having molecular weight 11,000-120,000 are found to be practically independent of molecular weight. [31]

**Effects of Phase Transitions**

At the crystal-melt transition, the surface free energy of crystalline phase $\gamma^c$ is related to that of the amorphous phase $\gamma^a$ by [32]

$$\gamma^c = \left(\frac{\rho_c}{\rho_a}\right)^n \gamma^a \tag{2.29}$$

where $\rho_c$ is the crystalline density, $\rho_a$ the amorphous density, and n the Macleod's exponent (Table 2-2).

Table 2-2. Macleod's exponent for some polymers

| polymer | Macleod's exponent |
|---|---|
| Polychloroprene | 4.2 |
| Poly(methyl methacrylate) | 4.2 |
| Poly(n-butyl methacrylate) | 4.2 |
| Polystyrene | 4.4 |
| Poly(vinyl acetate) | 3.2 |
| Poly(ethylene oxide) | 3.0 |
| Polybutylene | 4.1 |
| Polypropylene | 3.2 |
| Polyethylene, linear | 3.2 |
| Polyethylene, branched | 3.3 |
| polydimethylsiloxane | 3.5 |

Thus, at the crystal-melt transition, the surface free energy changes discontinuously, since the density is discontinuous. As $\rho_c$ is usually greater than $\rho_a$, the crystalline phase will higher surface free energy than amorphous phase. For

instance, polyethylene has n = 3.2, $\gamma^a$ = 35.7 dyne/cm, and $\rho_a$ = 0.855 g/ml at 20 ℃. The crystalline density $\rho_c$ is 1.000 g/ml. Thus $\gamma^c$ is calculated by eq. (2.29) to be 58.9 dyne/cm, which compares rather well with an experimental value of 53.6 dyne/cm. [33]

Semicrystalline polymers tend to be covered with an amorphous surface layer. As the amorphous phase has lower surface free energy, it tends to migrate to the surface.

**Copolymers and Blends**

Low-energy components in copolymers or blends tend to preferentially adsorb on the surface, just as in small-molecule liquids, as this will lower the free energy of the system.

Random Copolymers

The surface free energy of a random copolymer usually follows the linear relation [34]

$$\gamma = x_1\gamma_1 + x_2\gamma_2 \qquad (2.30)$$

where $\gamma$ is the surface free energy and x is the mole fraction. The subscripts 1 and 2 refer to the components 1 and 2, respectively. Such behavior is shown for random copolymers of ethylene oxide and propylene oxide in Figure 2-7.

**Block and Graft Copolymers**

However, block and graft copolymers show considerable surface activity of the lower energy component, when the lower-energy blocks or grafts are sufficient long that they can accumulate and orient on the surfaces independently of the rest of the molecule. For instance, pronounced surface activity is observed for ABA block

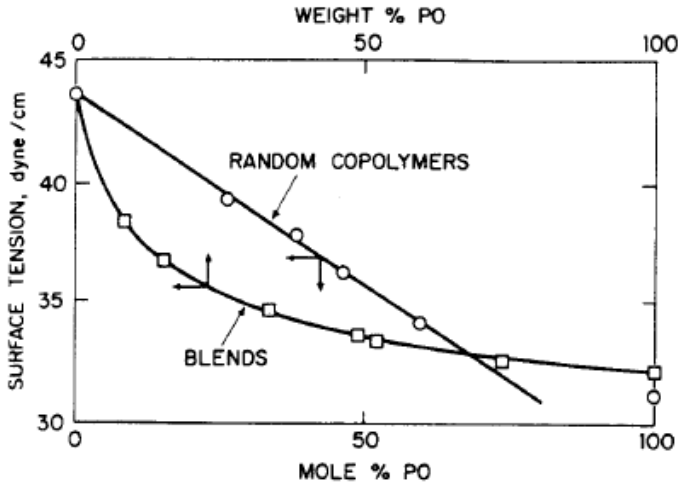


Figure 2-7. Linear additively of surface tension of random copolymers of ethylene oxide and propylene oxide, and surface-active behavior of blends of poly(ethylene oxide) (PEG 300) and poly(propylene oxide) (PPG 425). [34]

copolymers of ethylene oxide (A block, higher surface free energy) and propylene oxide (B block, lower surface free energy) (Figure 2-8). [34]

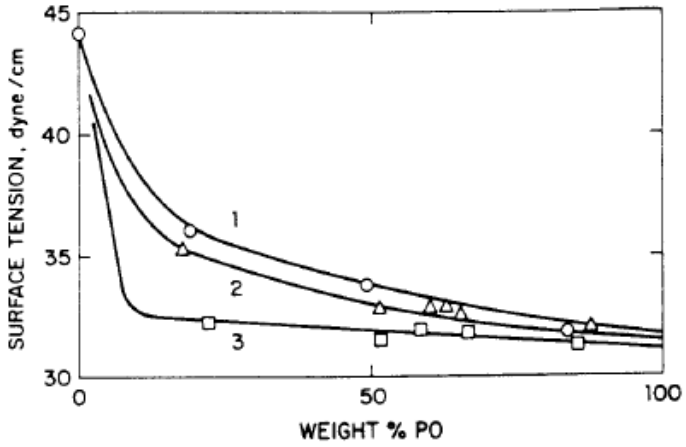


Figure 2-8. Surface tension versus composition for ABA block copolymers of ethylene oxide (A block) and propylene oxide (B block). Degree of polymerization are (1) DP = 16, (2) DP = 30, (3) DP = 56. [34]

**Blends of Polymers**

Blends of both compatible and incompatible polymers show pronounced surface activity, incompatible blends being more pronounced than compatible blends. The surface activity of an incompatible blends is further complicated by heterogeneous phase structure.

Surface activity of compatible blend of poly(ethylene oxide) and poly(propylene oxide) is shown in Figure 2-9. [34] The surface activity increases with increasing molecular weight, apparently because of increased in compatibility.

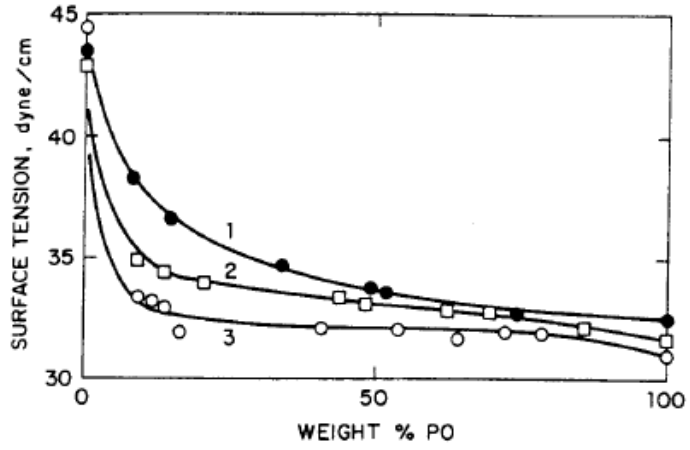


Figure 2-9. Surface tension of blends of compatible homopolymers. (1) poly(ethylene oxide) (PEG 300) + poly(propylene oxide) (PPG 425), (2) PPG 2025 + polyepichlorohydrin (PECH 1500), (3) PPG 400 + PECH 2000. [34]

## 2.2 Superhydrophobic Surfaces

Wettability is a fundamental property of a solid surface, which plays important roles in daily life, industry, and agriculture. Functional surfaces with special

wettability have aroused much interest because of their great advantages in applications. For example, the superhydrophilic surface (Figure 2-10) [35] with a water contact angle (CA) of almost 0° generated by UV irradiation has been successfully used as a transparent coating with antifogging and self-cleaning properties. On the other hand, various phenomena, such as contamination, snow sticking, erosion, and even current conduction are expected to be inhibited on superhydrophobic surfaces [36-39] with a CA larger than 150° and a sliding angle (SA) less than 10°. [40] The chemical compositions [41,42] determine the surface free energy and thus have great influence on wettability. However, it has certain limitation. For example, the -$CF_3$ terminated surface was reported to possess the lowest free energy and the best hydrophobicity, while on flat surfaces, the maximum CA could only reach about 120°. [43] The surface topographic structure is also an important factor that influences the wettability.

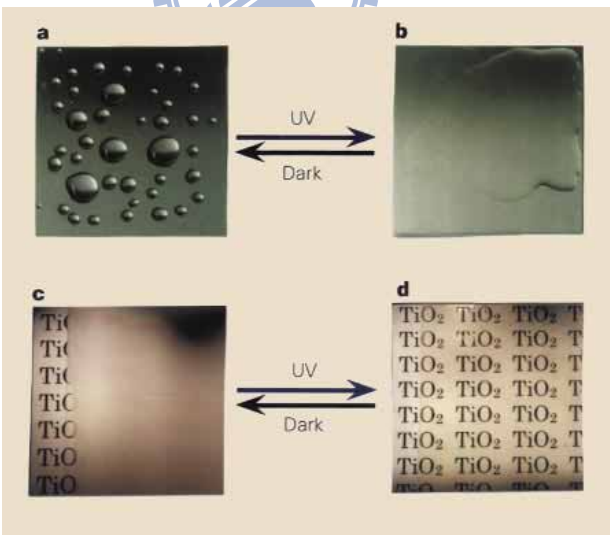


Figure 2-10 a, A hydrophobic surface before ultraviolet irradiation. b, A highly hydrophilic surface on ultraviolet irradiation. c, Exposure of a hydrophobic TiO2-coated glass to water vapour. The formation of fog (small water droplets) hindered the view of the text on paper placed behind the glass. d, Creation by ultraviolet irradiation of an antifogging surface. The high hydrophilicity prevents the

formation of water droplets, making the text clearly visible.

Conventionally, superhydrophobic surfaces have been produced mainly in two ways. One is to create a rough structure on a hydrophobic surface (CA > 90°), and the other is to modify a rough surface by materials with low surface energy. Up to now, many methods have been developed to produce rough surfaces, including solidification of melted alkylketene dimmer (AKD, akind of wax), [44] plasma polymerization/etching of polypropylene (PP) in presence of polytetrafluoroethylene (PTFE), [36] microwave plasma-enhanced chemical vapor deposition (MWPE-CVD) of trimethylmethoxysilane (TMMOS), [45] anodic oxidization of aluminum, [46] immersion of porous alumina gel films in boiling water, [47] mixing of a sublimation material with silica or boehmite, (Figure 2-11) [48] phase separation, [49] and molding [50] To obtain superhydrophobic surfaces, coating with low-surface-free-energy materials such as fluoroalkylsilane (FAS) is often necessary. [46-50] While the water CA has commonly been used as a criterion for the evaluation of hydrophobicity of a solid surface, this alone is insufficient to assess the sliding properties of water droplets on the surface. [51] A fully superhydrophobic surface should exhibit both high CA and low sliding angle, where sliding angle can also be expressed as the difference between advancing and receding contact angle (hysteresis).

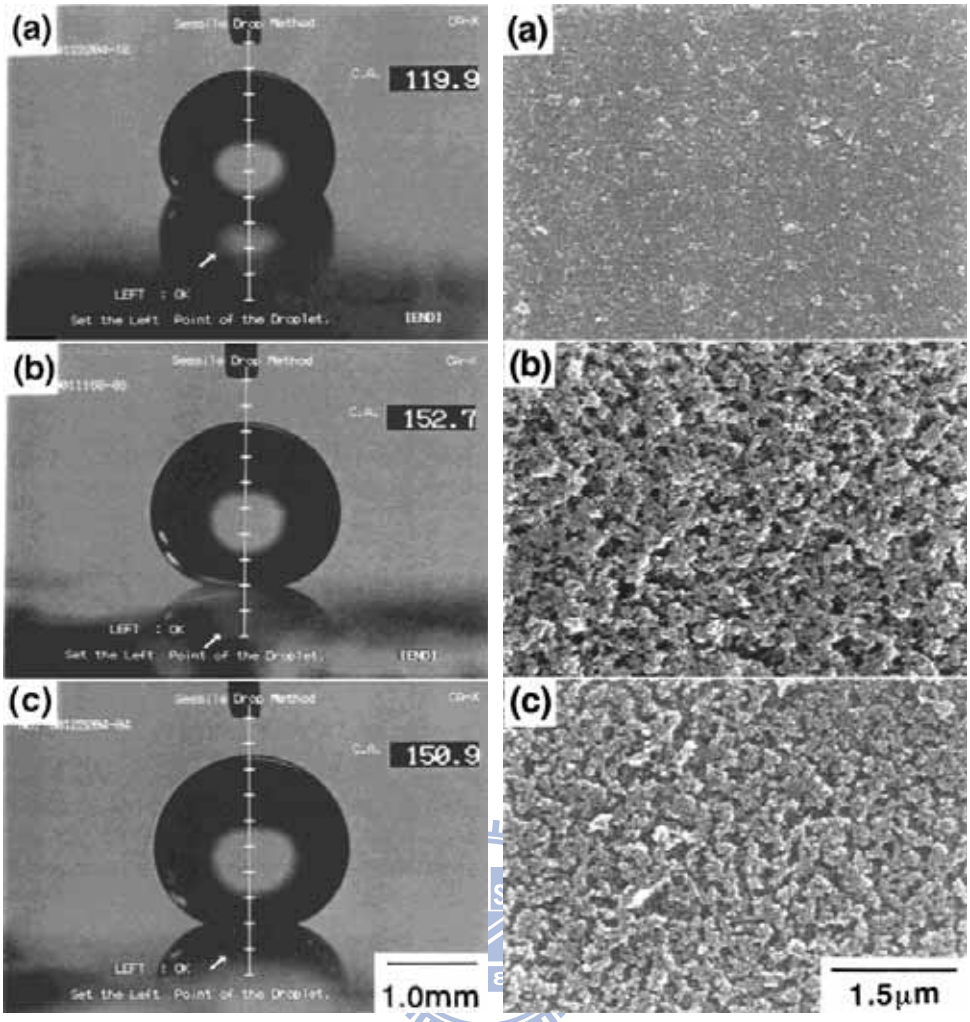


Figure 2-11 Shapes of water droplets and SEM micrographs of prepared films. a) Film prepared from a suspension containing only (AlOOH). b) Film prepared from a suspension containing (AlOOH) and ($Al(C_5H_7O_2)_3$). c) Film prepared from a suspension containing silica and ($Al(C_5H_7O_2)_3$)..

.

### 2.2.1 The Principle of Wetting

**Young's Relation**

Let us start with the academic case of a drop deposited on an ideal (i.e. homogeneous) solid (Figure 2-12). The drop contacts its substrate on a disc of radius $\ell$, whose border is a line (the so-called contact line) where the three phases of the system coexist. Close to this line, and whatever the size of the drop, we can observe

that the liquid joins the solid at an angle $\theta$, whose value defines the size, $\ell$, of the contact.

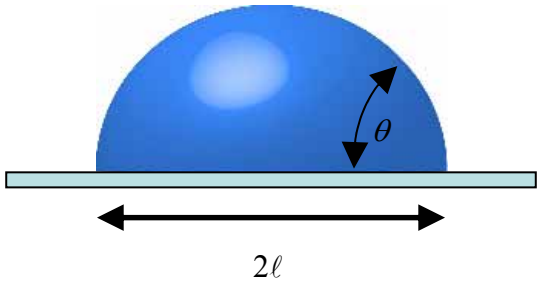


Figure 2-12. Liquid droplet on a solid. The liquid contacts the solid over a zone of size $\ell$, and joins it at an angle $\theta$.

The value of the contact angle was first discussed by Young. [2] Each interface draws the contact line so as to minimize the corresponding surface area, so that balancing the surface tensions on the direction of potential motion (i.e. the horizontal) yields a relation attributed to Young (although it does not explicitly show up in Young's paper):

$$\gamma_{LV}\cos\theta = \gamma_{SV} - \gamma_{SL} \qquad (2.5)$$

Equation (2.5) can alternatively be derived by calculating the variation of surface energy associated with a motion *dx* of the contact line (Figure 2-13).

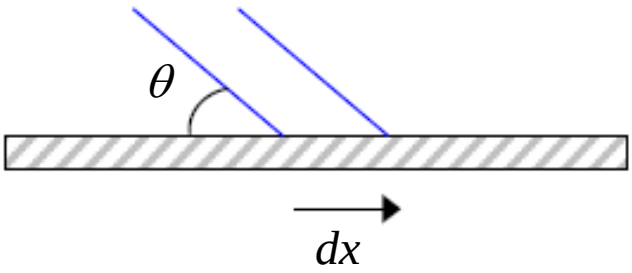


Figure 2-13. Displacing the contact line by a quantity dx (keeping the drop volume unchanged) modifies the surface area of each interface (solid/liquid, solid/vapor,

liquid/vapor).

We find

$$dE = (\gamma_{SL} - \gamma_{SV})dx + \gamma dx \cos\theta \qquad (2.31)$$

At equilibrium, E is minimum, which indeed yields equation (2.5).

**From Complete Wetting to Complete Drying**

Depending on the values of the different surface tensions (which are typically in the range of 20 to 500 $mNm^{-1}$ for pure liquids or solids), an angle may or may not be deduced from equation (2.5). Two limits are particularly interesting:

(a) If $(\gamma_{SV} - \gamma_{SL})$ is larger than $\gamma_{LV}$, the drop tends to spread completely on the solid, and the contact angle is considered as null ($\theta$ = 0°). As first identified by Marangoni, this condition (which can also be written $\gamma_{SV} > \gamma_{SL} + \gamma_{LV}$) indicates that the solid lowers its (surface) energy by being wetted. [52] Complete wetting happens for solids of high surface energy, such as glass or noble metals—but such solids often get polluted by aerosols (which wet them), so that their actual surface energy often decreases with time (and at the same time, these solids lose their ideality). This is the case with glass, which is wetted by water when it comes fresh out of a factory, but only shows partial wetting later, in most cases. Cleaning the glass very efficiently (with a strong acid) allows it to recover (transiently) a complete hydrophilicity. Complete wetting will also be observed with liquids of low surface tension ($\gamma_{LV}$ □ $\gamma_{SV}$), such as light alkanes or silicone oils, which wet completely glass, steel and most plastics. Surfactants, which lower the liquid/vapor surface tension, are often added to a paint to increase its wettability, in order to make the film of paint stable.

A drop deposited on a solid that it wets completely will spread spontaneously, and the question of the final contact (i.e. the size $\ell$) it develops with its substrate has

been discussed extensively over the last 20 years. We could think that the final stage of the drop is a monomolecular pancake (which defines $\ell$ for a given volume), but long range forces may thicken this pancake (in particular close to the wetting transition, where the spreading force, $\gamma_{SV} - \gamma_{SL} - \gamma_{LV}$, vanishes). [53]

(b) If $(\gamma_{SL} - \gamma_{SV})$ is larger than $\gamma_{LV}$, the drop should be in a pure non-wetting situation ($\theta$ = 180°). This can be easily observed by inverting the two fluids in a complete wetting situation (inverting indices L and V in equation (2.5) transforms $\theta$ in $\pi - \theta$): silicone oil wets most solids, so that an air bubble injected in a box filled with silicone oil will join the box ceiling at a contact angle of 180°. However, the important case of a solid which will not be wetted at all by water (with air around) cannot be achieved: on the most hydrophobic solids we know (waxes, or fluorinated materials such as Teflon), water drops make contact angles of the order of 120° or 130°, quite far from the maximum value of 180°. [54] One of our aims in this review is to show the different tricks which allow us to approach this limit, and to quantify the (expected) reduction of adhesion of the drops in such a limit.

### 2.2.2 Natural Examples

Several natural materials exhibit super-hydrophobicity, with advancing contact angles between 150° and 165°. Neinhuis and Barthlott reported that this is the case for the leaves of about 200 plants, including asphodelus, eucalyptus, euphorbia, Indian Cress, Lady's Mantle, lotus and tulipa (Figure 2-14). [55-57] These surfaces have generally three common features: (a) they are coated by an epicuticular film of wax, or by wax crystalloids, making them hydrophobic (Young contact angle greater than 90°); (b) they are decorated by textures such as bumps, at a scale of typically 10μm; (c) a secondary texture, of much smaller size (about 1μm in many cases) and different

morphology (often hairs) is superimposed on the first one. [55-57]

Figure 2-14 An almost ballshaped water droplet on a non-wettable plant leaf. [57]

Figure 2-15 shows as an example the upper surface of a leaf of Colocasia esculenta (Araceae), also called elephant ear, as observed under scanning electron microscopy (SEM). [58]

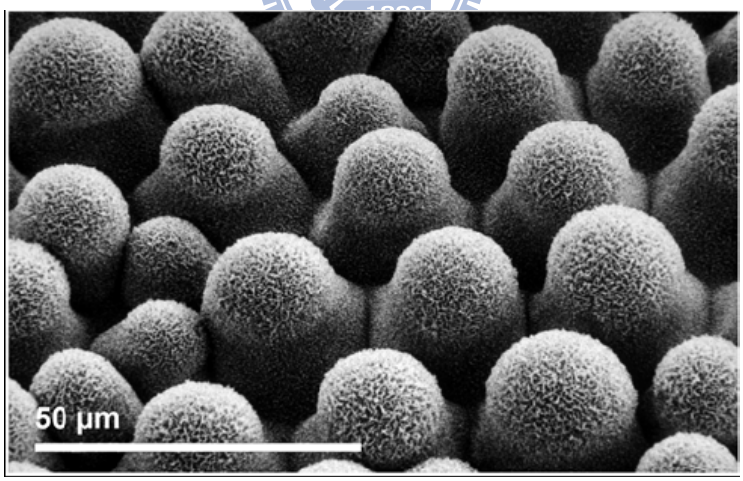


Figure 2-15. SEM picture of a super-hydrophobic plant (Colocasia esculenta). The surface is structured at two levels: bumps at a scale of 20 µm and hairs at a scale of 1µm. These structures together with the wax which coats the leaf provide super-hydrophobicity. [58]

Figure 2-16 Taking a leaf out of nature's book: electron micrographs of ultraphobic leaves.

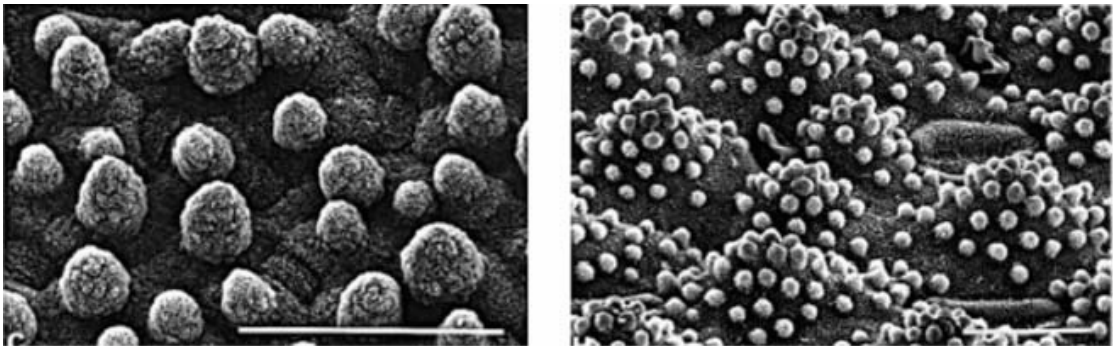

Figure 2-16 *Nelumbo nucifera*, left, scale bar =50 μm and *Hygoryza aristata*, right, scale bar= 20 μm, showing texture at different scales.

Similarly, animals can be super-hydrophobic, owing to micro-structures at a scale between 100 nm and several micrometres. This is the case for example for water strider legs (Figure 2-17), butterfly wings (and indeed lepidopter means 'having wings with scales') (Figure 2-18), duck feathers and some bugs. [59-61] In many cases, this is a strategy for allowing a safe interaction with water: a duck coming out of water immediately de-wets, and water striders are supported by the surface of a pond. Butterflies close their wings during the night, and dew condensation between the wings would stick them together if they were wettable. There is a Namibian beetle (Figure 2-19), Stenocara, which has a different reason for having part of its elytrae super-hydrophobic [62]: it survives in very desert areas, where water is only obtainable from a morning fog. Little spots in the elytrae are hydrophilic, so that the drops condense and grow there; once they are large enough, they detach and roll down the tilted beetle, following super-hydrophobic tracks (which, as we shall show, ensures a quick transportation without leakage) till they reach the beetle's mouthparts.

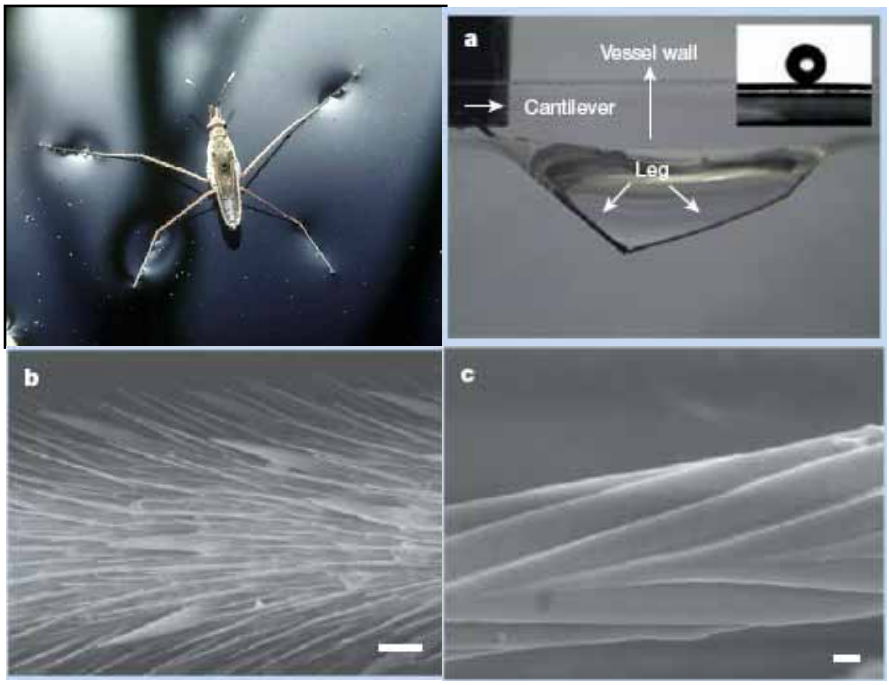


Figure 2-17. The non-wetting leg of a water strider. (a) Typical side view of a maximal-depth dimple (4.38 mm) just before the leg pierces the water surface. Inset, water droplet on a leg; this makes a contact angle of 167.6°. (b), (c), Scanning electron microscope images of a leg showing numerous oriented spindly microsetae (b) and the fine nanoscale grooved structures on a seta (c). Scale bars: b, 20 μm; c, 200 nm.

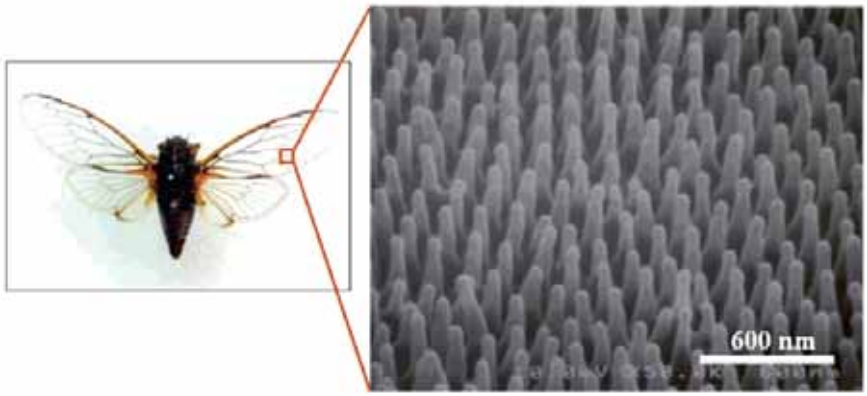


Figure 2-18. FE-SEM micrograph of the wing surface of Cicada orni with regularly

aligned nanoposts.

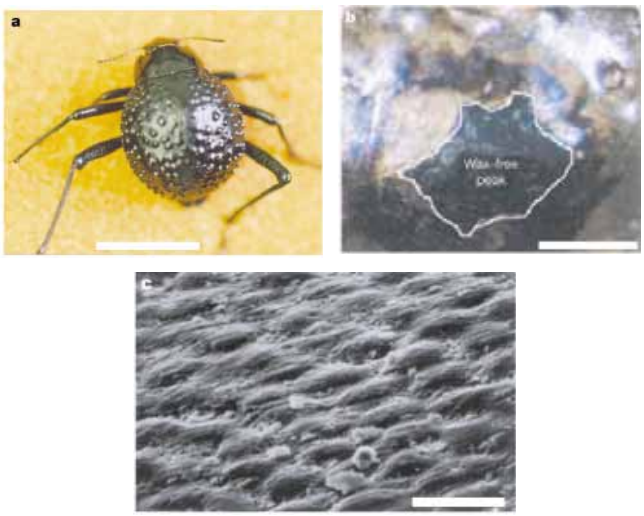


Figure 2-19. The water-capturing surface of the fused overwings (elytra) of the desert beetle Stenocara sp. (a) Adult female, dorsal view; peaks and troughs are evident on the surface of the elytra. (b) A 'bump' on the elytra, stained with Red O for 15 min and then with 60% isopropanol for 10 min, a procedure that tests for waxes. Depressed areas of the otherwise black elytra are stained positively (waxy, coloured), whereas the peaks of the bumps remain unstained (wax-free; black). (c) Scanning electron micrograph of the textured surface of the depressed areas. Scale bars, (a) 10 mm; (b) 0.2 mm; (c) 10 μm.

As a conclusion, all these natural materials clearly show that the hydrophobicity of a solid is enhanced by textures. We further examine what the mechanisms are of this effect and propose partial answers to the (open) question of why double structures are often present. But we first describe how many synthetic super-hydrophobic materials have been developed (in particular in the past few years) and discuss their properties.

### 2.2.3 Synthetic Substrates

Many synthetic materials have been developed like these natural examples in order to obtain water-repellency. Some applications are quite obvious: stone, wood and concrete need to be protected from the effects of rain. In other cases (fabrics), we need enhanced water-proofing. One can also try to get rid of droplets which affect the transparency of glass (window panes, windshields, greenhouses) or reflection (mirror). It is also expected (or hoped) that a water-repellent substrate will be anti-frost and anti-dew. But one of the most important properties of these substrates is their ability to let liquids move very quickly on them: this can be extremely interesting in microfluidic devices, where we often desire a reduction of the friction associated with a flow. This also explains why these materials are often referred to as self-cleaning: raindrops are efficiently removed, taking with them the dirt particles which were deposited on the solids [63]. We can see the same phenomenon when pouring liquid nitrogen on the ground: the very mobile drops take with them the dust present on the surface, the particles lowering interfacial energy by adsorbing at the interface. Many of the plants which are super-hydrophobic indeed look cleaner because of this effect— which could be one of the reasons for the reverence of the lotus in India.

One method to improve the liquid repellency of a surface is to combine a suitable chemical structure (surface energy) with a topographical microstructure (roughness); pervious attempts have included preparing fractal surface (Figure 2-20), [44] plasma treating polymer surfaces, [64,65] preparing roughened metal surface through chemical etching processing (Figure 2-21), [83] preparing gel-like roughened polymers through solvent processing(Figure 2-22), [66] preparing roughened block copolymers through solvent processing(Figure 2-23), [67] densely packing aligned carbon nanotubes (Figure 2-24) ,[68-70] surface-roughness-enhanced wettability of a

PNIPAAm-modified surface (Figure 2-25)[84]and preparing aligned polyacrylonitrile nanofibers (Figure 2-26). [71] Both super-hydrophobic and super-amphiphobic surfaces can result from increased surface roughness; this effect occurs in naturally on the lotus leaf, for example. [56,72] The surfaces of these leaves possess a micron-level roughness covered with nano-sized crystals of wax; [69] the water contact angles of these leaves can be as high as 160° because air is trapped between the water droplets and the wax crystals at the plant surface to minimize the contact area. [73]

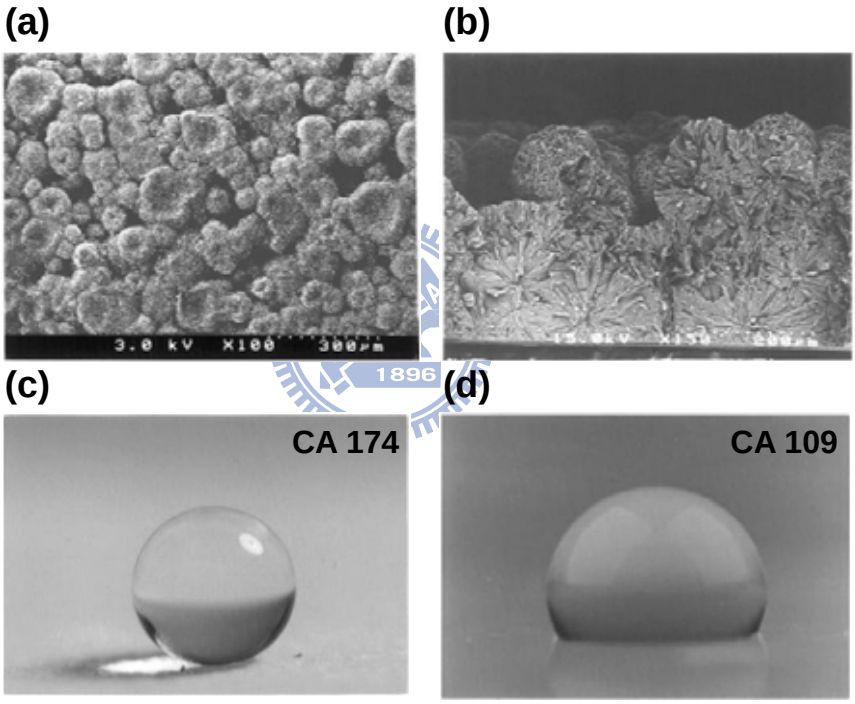


Figure 2-20. SEM images of the fractal alkylketene dimmer (AKD) surface: (a,) top view, (b) cross section**.** Water droplet on AKD surfaces: (c) fractal AKD surface; (d) flat AKD surface. [44]

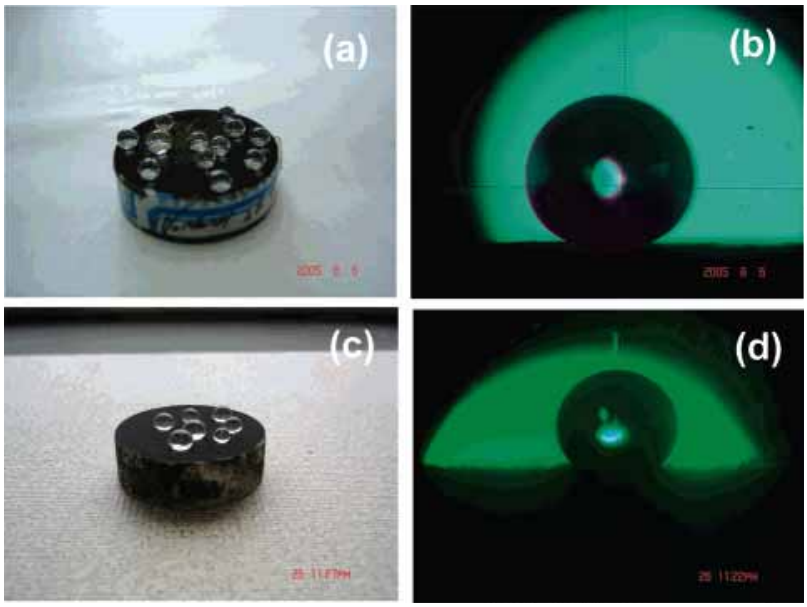


Figure 2-21. (a) Optical image of water droplets with different sizes on the surface of Al block treated with $C_9F_{20}$. (b) Profile of one water droplet on the surface having a CA of 168°. (c) Optical image of water droplets with different sizes on the surface of super-hydrophobic aluminum alloy modified with PDMSVT. (d) Profile of the water droplet with a CA of 161°. [83]

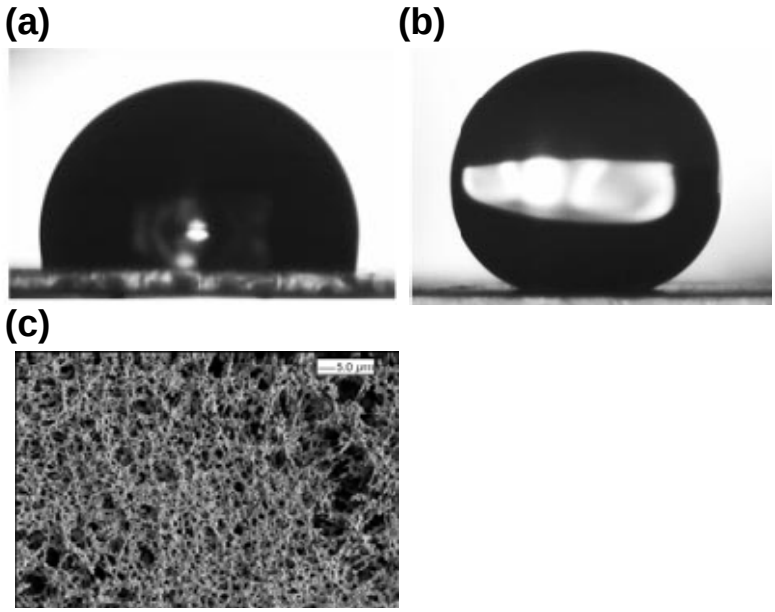


Figure 2-22. The profile of a water drop on (a) a smooth i-PP surface (CA = 104°), (b) a superhydrophobic i-PP coating on a glass slide (CA = 160°). (c) SEM picture of

a superhydrophobic i-PP film. [66]

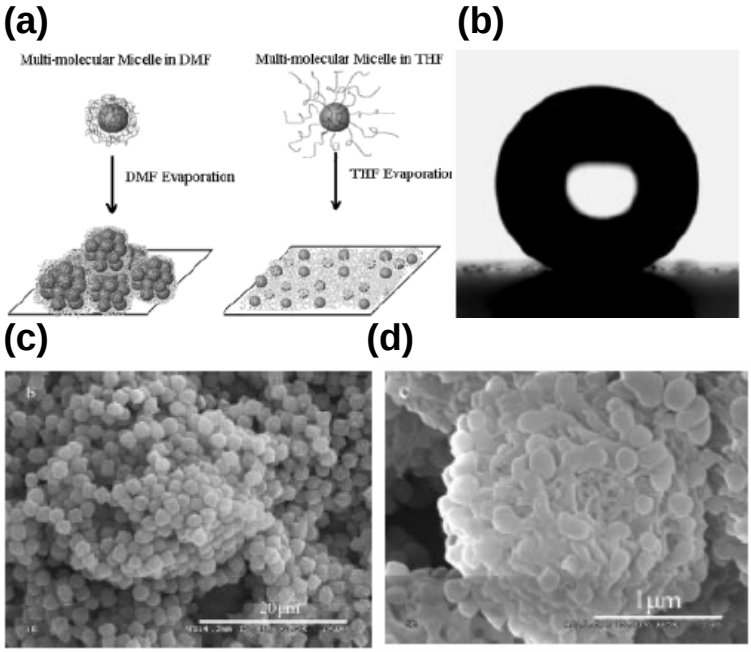


Figure 2-23. (a) Illustration of the solvent effect on the morphologies of PP-PMMA copolymer surface. (b) The profile of a water drop on superhydrophobic polymer surface. (c) SEM images of superhydrophobic polymer. (d) Enlarged view of (c). [67]

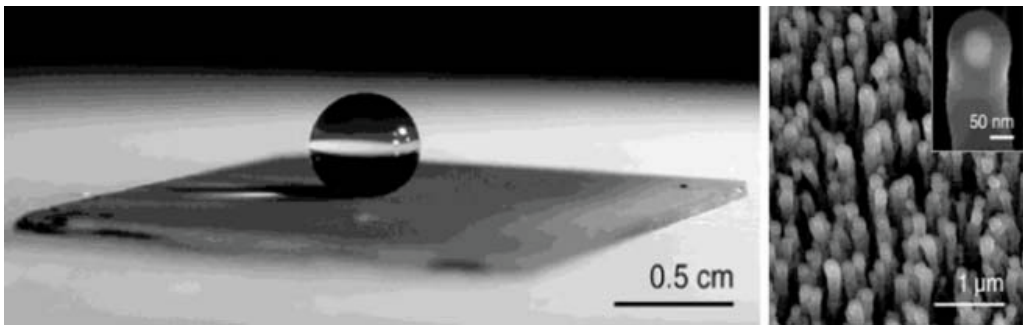


Figure 2-24 Left, a drop of water resting on a PTFE-coated carbon nanotube forest. Right, an electron micrograph of the same ultraphobic surface. [68]

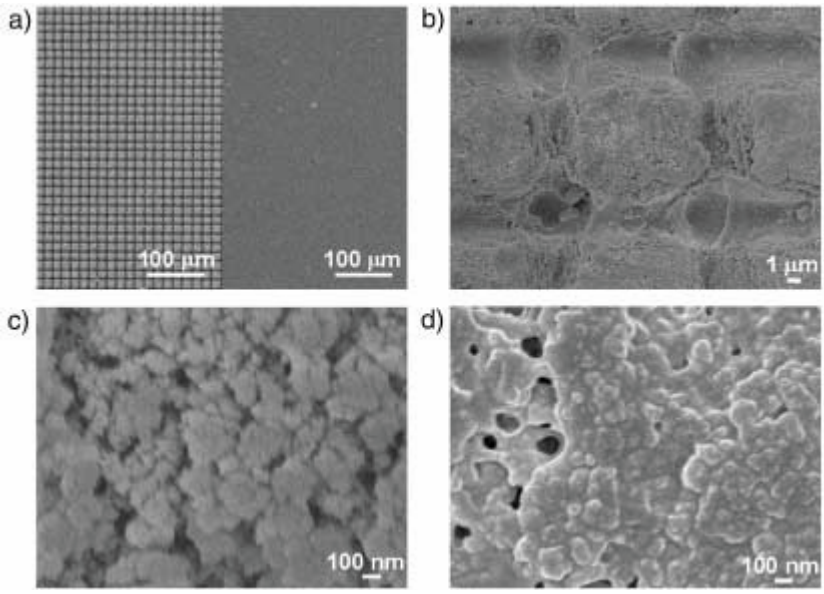


Figure 2-25 a) SEM image for the regular array of silicon microconvexes with PNIPAAm modification (left), compared with that of flat substrate (right). b) Magnified image of the microconvex array in the right of (a). c) Nanostructures on a single microconvex without PNIPAAm modification. d) Nanostructures on a single microconvex with PNIPAAm modification. [84]

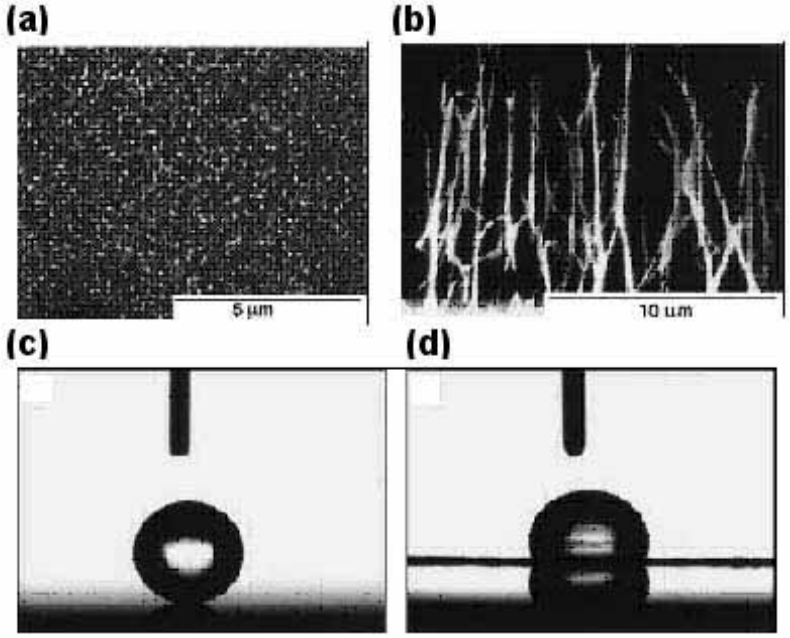


Figure 2-26. SEM images of (a) surface of the PAN nanofibers; (b) cross-sectional

view of the as-synthesized PAN nanofibers. Shapes of water droplets on (c) the PAN nanofibers with a rough surface; (d) the native PAN film with smooth surface. [72]

Whatever its nature, natural or artificial, regularly patterned or highly disordered, a structured hydrophobic material is super-hydrophobic. This property a priori sounds interesting, since it should provide a strong reduction of adhesion of the drops—but the situation is not that simple: we saw that in some cases the hysteresis of the contact angle can be extremely small, which defines a slippery surface, but that in other cases this quantity can be large, which implies a sticky state (in spite of a very high contact angle), of less obvious practical interest. We now give some hints about the mechanisms responsible for these different effects, and stress in particular that indeed two different super-hydrophobic states can exist and even coexist.

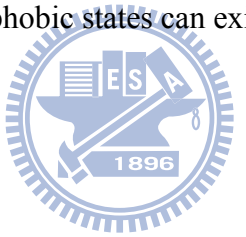

### 2.2.4 Models

**The Wenzel Equation**

The first attempt to understand the effect of roughness on wettability is that of Wenzel (1936). Wenzel was interested in ways of improving the water-proofing of fabrics, which are naturally textured materials (at the scale of the monofilaments which make the yarns). [74] He had noticed that the natural tendency of a material (hydrophilic or hydrophobic) is enhanced by the presence of textures. Wenzel's interpretation of these facts is based on the increasing of the surface area of a material because of its roughness: a liquid will tend to spread more on a rough hydrophilic substrate, since it allows it to develop more solid/liquid contact (which is favorable in a hydrophilic situation). Conversely, a rough hydrophobic material appears

(apparently) more hydrophobic, because the liquid would have to develop a much larger (unfavorable) contact with the solid if the contact angle is kept unchanged.

The key parameter is thus the roughness factor, defined by Wenzel as the ratio of the true surface area A (taking into account the peaks and valleys on the surface) to the apparent surface area A' is defined as the roughness factor $r$ = A/A'. It is thus a dimensionless number, larger than unity, and all the larger since the surface is rough. The main assumption of Wenzel is that the liquid follows the defects of the solid surface, as it is deposited on it. The apparent contact angle is the one which minimizes the (surface) energy of the drop as shown in Figure 2-27.

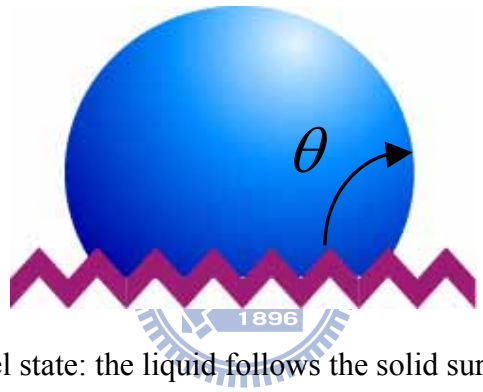


Figure 2-27. The Wenzel state: the liquid follows the solid surface.

For r = 1 (flat solid), we get back Young's law (equation (2.5)). For a rough surface (r > 1), we derive Wenzel's relation: [74, 75]

$$\cos\theta_w = r\cos\theta \tag{2.32}$$

In Eq. (2.32), $\theta$ is the intrinsic CA on a smooth surface, $\theta_w$ is that on a rough surface made of the same material, and $r$ is the roughness factor. The Wenzel relation qualitatively agrees with the main observations: both hydrophobicity and hydrophilicity are enhanced by roughness, since we deduce from equation (2.32) that increasing surface roughness results in actual CA decrease for hydrophilic materials ($\theta$ < 90°) and increase for hydrophobic materials ($\theta$ > 90°).. This looks like a simple and attractive solution for inducing superhydrophobicity: the rougher the

material, the higher the contact angle. However, this is not that simple, for two reasons: firstly, contact angles generally spread in quite a large interval, contrasting with equation (2.32) which predicts a unique angle. This interval, often referred to as the contact angle hysteresis, is responsible for the sticking of drops, an effect in contradiction with water repellency. In a Wenzel state, the contact angle hysteresis will be very large: trying to remove a liquid makes it contact itself (owing to the fraction left in the textures), which yields a low ‘‘receding’’ contact angle—values as low as 40° were reported, making this state hydrophilic-like in the receding stage. [76] The second reason which makes it impossible to reach high values of $\theta_w$, as expected from equation (2.32) for $r$ large and $\theta > 90°$, can be guessed quite easily: for very rough hydrophobic materials, the energy stored for following the solid surface is much larger than the energy associated with the air pockets sketched in Fig. 2-28. [76-79]

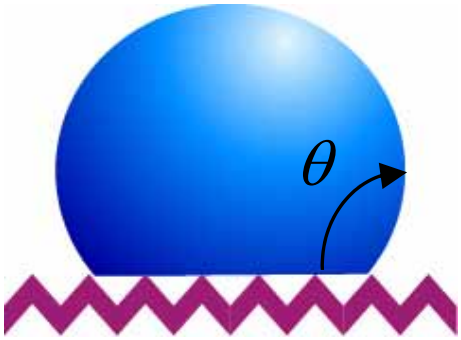


Figure 2-28. The Cassie state, the liquid only contacts the top of the asperities, leaving air below.

**The Cassie and Baxter Equation**

In Cassie and Baxter state (Figure 2-28), the liquid only contacts the solid

through the top of the asperities, on a fraction that we denote as $f_1$. [80] If only air were present between the solid and the liquid (as for a water drop on a very hot plate), the ‘‘contact angle’’ would be 180°: the smaller $f_1$, the closer to this extreme situation, and thus the higher the hydrophobicity. More precisely, the contact angle $\theta_c$ of such a ‘‘fakir’’ drop (Figure 2-28) is an average between the angles on the solid (of cosine $\cos\theta$), and on the air (of cosine-1), respectively weighed by the fractions $f_1$ and 1 - $f_1$, which yields:

$\cos\theta_c = f_1 \cos\theta_1 + f_2 \cos\theta_2$

$f_1$ , $f_2$ :the respective fraction of projected planner area $f_1 + f_2 = 1$

$\theta_1, \theta_2$ : equilibrium contact angle

$$\cos\theta_c = f_1 (\cos\theta_1 + 1) - 1 \qquad (2.33)$$

For $\theta_1$ = 110° and $f_1$ = 10%, we find that $\theta_c$ is about 160°. In this case, 90% of the drop base contacts air! This makes it understandable that the corresponding hysteresis is observed to be very low (typically around 5 to 10°), as first reported by Johnson and Dettre: [81] the liquid has very little interactions with its substrate. Hence, this state will be the (only) repellent one, since it achieves both a large contact angle and a small hysteresis (this can be observed further, in Figure 2-29).

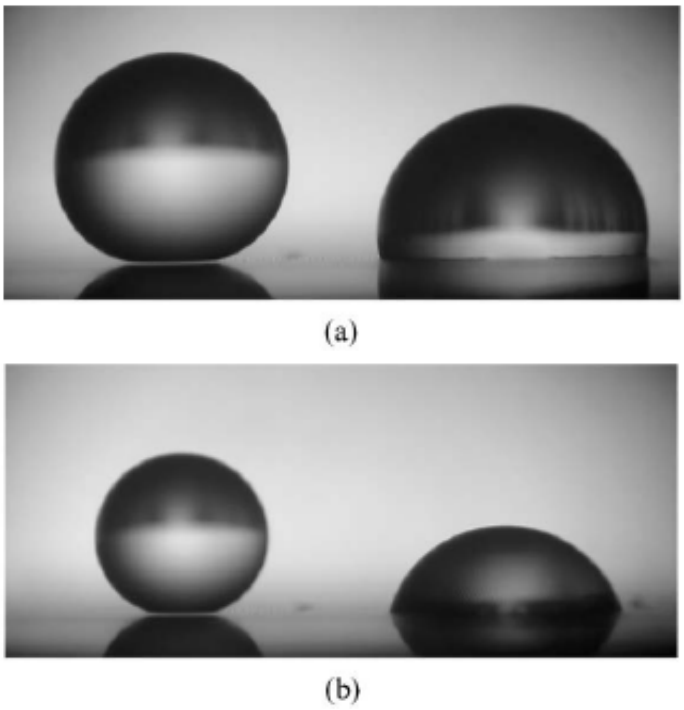


Figure 2-29. Millimetric water drops (of the same volume) deposited on a superhydrophobic substrate consisting of dilute pillars ($f_1 = 0.01$). (a) The right drop has been pressed, which induced a Wenzel state, characterized by a smaller angle (the roughness is very low, and equal to 1.1). The light passes below the left drop, indicating a Cassie state. (b) Ten minutes later, the drop volumes have decreased, owing to evaporation, and angles became receding ones. The difference of hysteresis between both states is clearly visible: the Wenzel drop even became hydrophilic

$\theta_c$ monotonously increases as $f_1$ decreases, suggesting that $f_1$ should be made as small as possible. But reducing $f_1$ also makes the roughness decrease, so that we reach the critical roughness rc below which the Wenzel state is favoured. The quantity rc is easily deduced from the intersection of equation (2.32) and (2.33), and is found to be $(f_1 - 1)/\cos\theta + f_1$, which is generally close to $-1/\cos\theta$ (since we will often have: $f_1 << 1$). For $\theta = 120°$ (a high value for the Young angle, obtained on fluorinated substrates), the fakir state will thus be favored for larger roughness factors.

Equations (2.32) and (2.33) should therefore be successively obeyed as the contact angle increases, and the threshold value $\theta$c between the two regimes given by equating the two (Figure 2-30).Conversely, Öner and McCarthy experimentally observed that below a critical density of defects (i.e. below a critical roughness), there is indeed a serious deterioration of the water-repellent properties. [82]

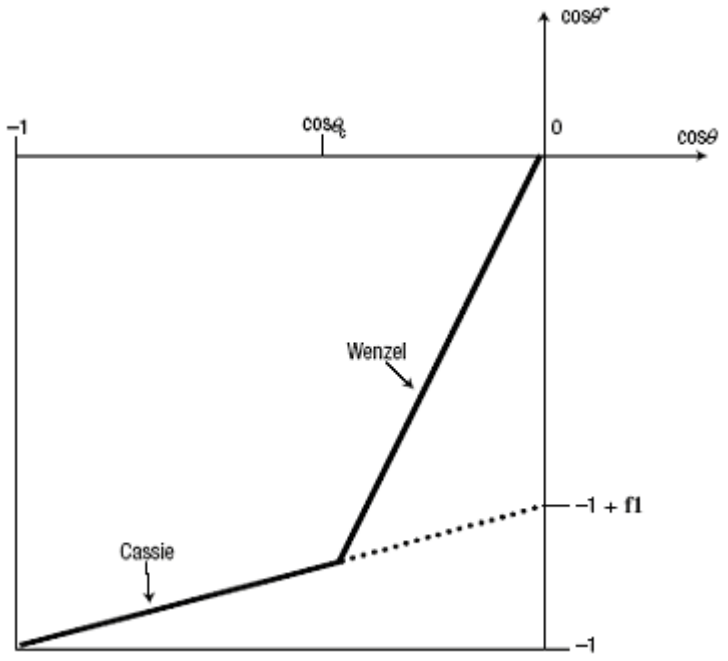


Figure 2-30 The two models of superhydrophobicity. For a moderate hydrophobicity($90<\theta<\theta_c$, where $\theta$ is the contact angle on a flat surface, and $\theta_c$ is fixed by the texture design, as defined in the text), the apparent contact angle$\theta$* should be given by the Wenzel model (equation 2.32). If $\theta$ is larger than $\theta$c, air remains trapped below the drop, which sits on a composite surface made of solid and air; $f_1$ is the fraction of solid in contact with the liquid (Cassie regime, equation 2.33). However it has often been reported that the Cassie regime can also be observed for $\theta<\theta$c, in spite of a higher energy.This metastable situation is represented by a dotted line.

## 2.3 Photocatalytic Coatings

The second class of self-cleaning surfaces to be discussed differ from Lotus-Effect coatings in that they are hydrophilic rather than hydrophobic, and do not rely solely on the flow of water to wash away dirt. These coatings chemically break down dirt when exposed to light, a process known as 'photocatalysis', although of course it is the coating not the incident light that acts as a catalyst. While the Lotus-Effect was inspired by the self-cleaning properties of plant leaves,hydrophilic coatings have parallels with photosynthesis, using sunlight to drive chemistry. Despite the commercialisation of a hydrophilic self-cleaning coating in a number of products, the field is far from mature; investigations into the fundamental mechanisms of self-cleaning and characterisations of new coatings are regularly published in the primary literature.

In 2001 Pilkington Glass announced the development of the first self-cleaning windows, Pilkington Activ™, and in the following months several other major glass companies released similar products, including PPG's Sunclean™. As a result, glazing is perhaps the largest commercialisation of self-cleaning coatings to date. All of these windows are coated with a thin transparent layer of titanium dioxide (titania or $TiO_2$), a coating which acts to clean the window in sunlight through two distinct properties: photocatalysis causes the coating to chemically break down organic dirt adsorbed onto the window, while hydrophilicity causes water to form 'sheets' rather than droplets – contact angles are reduced to very low values in sunlight (the coating becomes 'super-hydrophilic'),and dirt is washed away. Titania has become the material of choice for self-cleaning windows, and hydrophilic self-cleaning surfaces in general, because of its favourable physical and chemical properties. Not only is titania highly efficient at photocatalysing dirt in sunlight and reaching the

superhydrophilic state, it is also non-toxic, chemically inert in the absence of light, inexpensive, relatively easy to handle and deposit into thin films and is an established household chemical – it is used as a pigment in cosmetics and paint and as a food additive. The latter point may explain the rapid transition of self-cleaning titania surfaces from the research laboratory to the marketplace. The mechanisms of the self-cleaning processes that occur on titania surfaces have been thoroughly investigated over the past decade,[85] and although research continues to describe the exact mechanism for the destruction of specific pollutants,[86–88] a basic model has gained wide acceptance. A thorough discussion of the theory of photocatalysis and super-hydrophilicity is beyond the scope of this article, hence only a brief summary follows. Greater detail can be found in one of several review articles on the subject.[85,89–91] A semiconductor under normal conditions, titanium dioxide absorbs light with energy equal to or greater than its band gap energy, resulting in excited charge carriers: an electron, $e^-$, and a hole, $h^+$ (Fig. 2-31). Although the fate of most of these charge carriers is rapid recombination, some migrate to the surface. There, holes cause the oxidzation of adsorbed organic molecules while electrons eventually combine with atmospheric oxygen to give the superoxide radical, which quickly attacks nearby organic molecules. The result is a cleaning of the surface by 'cold combustion', the conversion of organic molecules to carbon dioxide and water (and other products if heteroatoms are present) at ambient temperatures. This process is remarkably effective and clean; e.g. the total decomposition of stearic acid [$CH_3(CH_2)_{16}CO_2H$] in the presence of atmospheric oxygen to $CO_2$ and $H_2O$, A wide range of solid-, liquid- and gas-phase organic pollutants can be broken down in this way, including aromatics, polymers, dyes and surfactants,[85] although a much smaller range of inorganic materials have been successfully decomposed on titania.

Photocatalysis is usually tested by monitoring the destruction of a model pollutant.

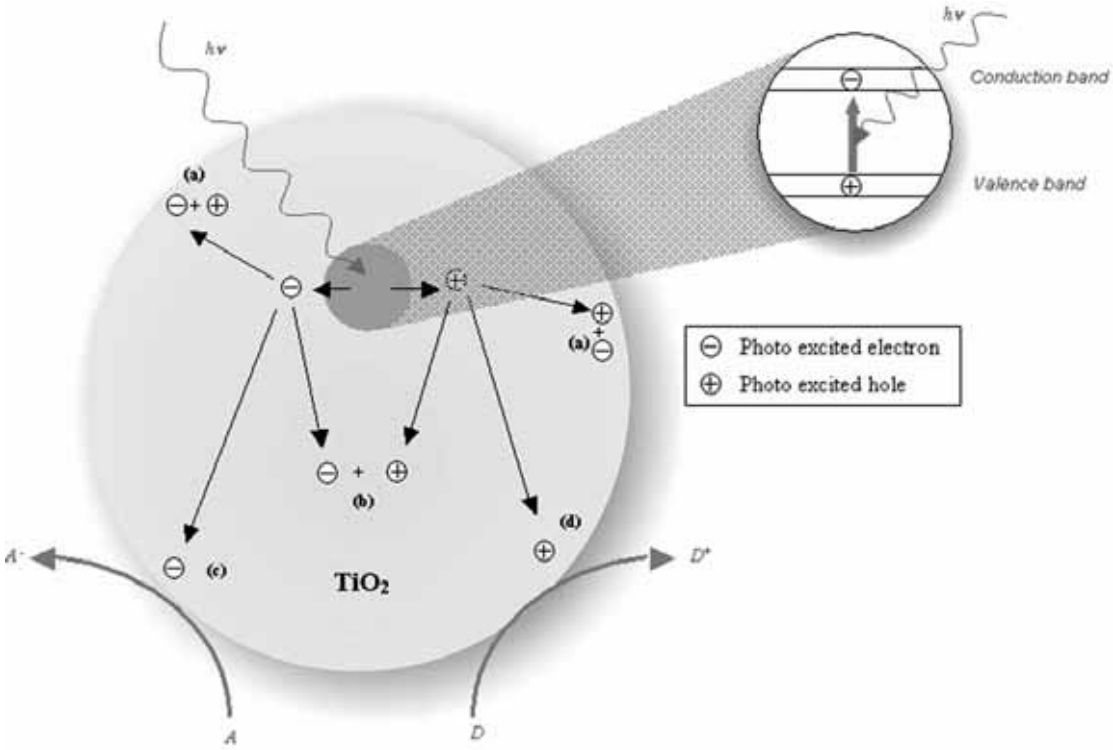


Figure 2-31 Upon irradiation of $TiO_2$ by ultra band gap light, the semiconductor undergoes photo-excitation. The electron and the hole that result can follow one of several pathways: (a) electron–hole recombination on the surface; (b) electron–hole recombination in the bulk reaction of the semiconductor; (c) electron acceptor A is reduced by photogenerated electrons; and (d) electron donor D is oxidised by photogenerated holes.

Super-hydrophilicity in $TiO_2$ is also a light-induced property. [92] Holes produced by photo-excitation of the semiconductor oxidise lattice oxygen at the surface of the material, resulting in oxygen vacancies. These can be filled by adsorbed water, resulting in surface hydroxide groups that make the wetted surface more

favourable compared to the dry surface, lowering the static contact angle to almost 0° after irradiation. [93] Both self-cleaning properties of $TiO_2$ are therefore governed by the absorption of ultra band gap light and the generation of electron/hole pairs. The band gap of bulk anatase TiO2 is 3.2 eV, corresponding to light of wavelength 390 nm – near-ultraviolet (UV) light. The physical and chemical properties of $TiO_2$ depend greatly on its form and the method of preparing the sample. Several polymorphs of $TiO_2$ are known, the most significant of which are rutile and anatase. The positions of the conduction and valence bands relative to key redox potentials cause pure anatase to be very photoactive (photocatalytic and super-hydrophilic) while pure rutile is less so.[85,94] As highlighted by a recent Royal Society report, nanoscale (dimensions in the range 1–10 nm) and micro- or macro-scale titania show distinctly different properties. Semiconductors with physical dimensions of the order of the wavelengths of the electrons they contain display properties not observed in the bulk solid. Such materials are often referred to as nanoparticles, nanocrystals or quantum dots. Bulk or macroscale powder titania is a brilliant white solid, non-toxic and widely used as a pigment in paint, cosmetics and food, while nanoscale titania particles are used in sunscreens and their absorption properties.

## References


[1] A. Dupré, *Theorié mécanique de la chleur*, Paris, **1869**, p.368.

[2] T. Young, *Phil Trans. R. Soci. Lond.* **1805**, *95*, 65.

[3] A. S. Michaeles, S. W. Dean, Jr., J. Phys. Chem. **1962**, *66*, 34.

[4] G. L. J. Baily, Proc. 2nd Int. Congr. Surf. Act., **1957**, *3*, 189.

[5] J. H. Poynting, J. J. Thompson, *A Textbook of Physics: Properties of Matter,* 8th ed., Charles Griffin, London, **1920**.

[6] L. A. Girifalco, R. J. Good, *J. Phys. Chem.* **1957**, *61*, 904.

[7] R. J. Good, L. A. Girifalco, G. Kraus, *J Phys. Chem.* **1957**, *62*, 1418.

[8] R. J. Good, L. A. Girifalco, J. Phys. Chem. **1960**, *64*, 561.

[9] F. W. Fowkes, in *Contact Angle, Wettability and Adhesion, Advances in Chemistry Series* 43, R. F. Gould, Ed., American Chemical Society, Washington, DC, **1964**, p. 99.

[10] F. W. Fowkes, in *Adhesion and Adsorption of Polymers, Polymer Science and Technology*, vol. 12A, L. H. Lee, Ed., Plenum Press, New York, **1980**, p. 43.

[11] D. K. Owens, R. C. Wendt, *J. Appl. Polym. Sci.* **1969**, *13*, 1741.

[12] D. H. Kaelble, J. Adhesion **1970**, *2*, 50.

[13] S. Wu, J. Polym. Sci., Part C **1971**, *34*, 19.

[14] S. Wu, in *Adhesion and Adsorption of Polymers, Polymer Science and Technology*, vol. 12A, L. H. Lee, Ed., Plenum Press, New York, **1980**, p. 53.

[15] F. M. Fowkes, M. A. Mostafa, *Int. Eng. Chem. Prod. Res. Dev.* **1978**, *17*, 3.

[16] F. M. Fowkes, D. C. McCarthy, M. A. Mostafa, *J. Colloid Interface Sci.* **1980**, *78*, 200.

[17] C. J. van Oss, M. K. Chaudhury, R. J. Good, *Chem. Rev.* **1988**, *88*, 927.

[18] C. J. van Oss, L. Ju, M. K. Chaudhury, R. J. Good, *J. Colloid Interface Sci.* **1989**,

*128*, 313.

[19] C. J. van Oss, R. J. Good, *J. Macromol. Sci.-Chem.* **1989**, *A26*, 1183.

[20] C. J. van Oss, *J. Dispers. Sci. Technol.* **1990**, *11*, 491.

[21] C. J. van Oss, K. Arnold, R. J. Good, K. Gawrisch, S. Ohki, *J. Macromol. Sci.-Chem.* **1990**, *A27*, 563.

[22] C. J. van Oss, R. J. Good, H. J. Busscher, *J. Dispers. Sci. Technol.* **1990**, *11*, 75.

[23] C. J. van Oss, R. F. Giese, Jr., R. J. Good, *Langmuir* **1990**, *6*, 1711.

[24] R. J. Good, C. J. van Oss, in *Modern Approaches to Wettability*, M. E. Schrader and G. I. Loeb, Eds., Plenum Press, New York, **1992**, p. 1.

[25] R. J. Good, in *Contact Angle, Wetting, and Adhesion*, K. L. Mittal, Ed., VSP, xxx, **1993**, p. 3.

[26] H. W. Fox, W. A. Zisman, *J. Colloid Sci.* **1950**, *5*, 514.

[27] H. W. Fox, W. A. Zisman, *J. Colloid Sci.* **1952**, *7*, 109.

[28] H. W. Fox, W. A. Zisman, *J. Colloid Sci.* **1952**, *7*, 428.

[29] D. G. LeGrand, G. L. Gaines, Jr., *J. Colloid Interface Sci.* **1969**, *31*, 162.

[30] D. G. LeGrand, G. L. Gaines, Jr., *J. Colloid Interface Sci.* **1973**, *42*, 181.

[31] S. Wu, *J. Colloid Interface Sci.* **1969**, *31*, 153.

[32] S. Wu, J. Macromol. Sci. **1974**, *C10*, 1.

[33] H. Schonhorn, F. W. Ryan, J. Phys. Chem. **1966**, *70*, 3811.

[34] A. K. Rastogi, L. E. St. Pierre, *J. Colloid Interface Sci.* **1969**, *31*, 168.

[35] R. Wang, K. Hashimoto, A. Fujishima, M. Chikuni, E. Kojima, A. Kitamura, M. Shimohigoshi, T. Watanabe, *Nature* **1997**, *388*, 431.

[36] W. Chen, A. Y. Fadeev, M. C. Hsieh, D. Õner, J. Youngblood, T. J. McCarthy, *Langmuir* **1999**, *15*, 3395.

[37] L. Feng, S. Li, Y. Li,; H. Li, L. Zhang, J. Zhai, Y. Song, B. Liu, L. Jiang, D. Zhu,

*Adv. Mater.* **2002**, *14*, 1857.

[38] R. Blossey, *Nat. Mater.* **2003**, *2*, 301.

[39] A. Lafuma, D. Quéré, *Nat. Mater.* **2003**, *2*, 457.

[40] A. Nakajima, A. Fujishima, K. Hashimoto, T. Watanabe, *Adv. Mater.* **1999**, *11*, 1365.

[41] J. T. Woodward, H. Gwin, D. K. Schwartz, *Langmuir* **2000**, *16*, 2957.

[42] T. Sun, W. Song, L. Jiang, *Chem. Commun.* **2005**, 1723.

[43] T. Nishino, M. Meguro, K. Nakamae, M. Matsushita, Y. Ueda, *Langmuir* **1999**, *15*, 4321.

[44] T. Onda, S. Shibuichi, N. Satoh, K. Tsujii, *Langmuir* **1996**, *12*, 2125.

[45] Y. Wu, H. Sugimura, Y. Inoue, O. Takai, *Chem. Vap. Deposition* **2002**, *8*, 47.

[46] K. Tsujii, T. Yamamoto, T. Onda, S. Shibuchi, *Angew. Chem. Int. Ed. Engl.* **1997**, *36*, 1011.

[47] K. Tadanaga, N. Katata, T. Minami, *J. Am. Ceram. Soc.* **1997**, *80*, 3213.

[48] A. Nakajima, A. Fujishima, K. Hashimoto, T. Watanabe, *Adv. Mater.* **1999**, *11*, 1365.

[49] A. Nakajima, K. Abe, K. Hashimoto, T. Watanabe, *Thin Solid Films* **2000**, *376*, 140.

[50] J. Bico, C. Marzolin, D. Quéré, *Europhys. Lett.* **1999**, *47*, 220.

[51] M. Miwa, A. Nakajima, A. Fujishima, K. Hashimoto, T. Watanabe, *Langmuir* **2000**, *16*, 5754.

[52] C. Marangoni, *Ann. Phys. Chem.* **1871**, *143*, 337.

[53] P. G. De Gennes, *Rev. Mod. Phys.* **1985**, *57*, 827.

[54] E. G. Shafrin, W. A. Zisman, *Contact Angle, Wettability and Adhesion (Advances in Chemistry Series vol 43)* (Washington, DC: American Chemical Society) 1964

pp 145

[55] C. Neinhuis, W. Barthlott, *Ann. Bot.* **1997**, *79*, 667.

[56] C. Neinhuis, W. Barthlott, *Planta* **1997**, *202*, 1.

[57] R. Blossey *Nat. Mater.* **2003**, *2*, 301.

[58] P. Wagner, R. Fürstner, W. Barthlott, C. Neinhuis, *J. Exp. Bot.* **2003**, *54*, 1.

[59] T. Wagner, C. Neinhuis, W. Barthlott, *Acta Zool.* **1996**, *3*, 213.

[60] W. Lee, M. K. Jin, W. C. Yoo, J. K. Lee, *Langmuir* **2004**, *20*, 7665.

[61] X. Gao, L. Jiang, *Nature* **2004**, *432* 36.

[62] A. R. Parker, C. R. Lawrence, *Nature* **2001**, *414* 33

[63] R. Blossey *Nat. Mater.* **2003**, *2*, 301.

[64] M. Morra, E. Occhiello, F. Garbassi, *Langmuir* **1989**, *5*, 872.

[65] I. Woodward, W. C. E. Schofield, V. Roucoules, J. P. S. Badyal, *Langmuir* **2003**, *19*, 3432.

[66] H. Y. Erbil, A. L. Demirel, Y. Avci, O. Mert, *Science* **2003**, *299*, 1377.

[67] Q. Xie, G. Fan, N. Zhao, X. Guo, J. Xu, J. Dong, L. Zhang, Y. Zhang, C. C. Han, *Adv. Mater.* **2004**, *16*, 302.

[68] K. K. S. Lau, J. Bico, K. B. K. Teo, M. Chhowalla, G. A. J. Amaratunga, W. I. Milne, G. H. McKinley, K. K. Gleason, *Nano. Lett.* **2003**, *3*, 1701.

[69] L. Feng, S. Li,Y. Li, H. Li, L. Zhang, J. Zhai,Y. Song, B. Liu, L. Jiang, D. Zhu, *Adv. Mater.* **2002**, *14*, 1857.

[70] H. Li, X. Wang, Y. Song, Y. Liu, Q. Li, L. Jiang, D. Zhu, *Angew. Chem. Int. Ed*. **2001**, *40*, 1743.

[71] L. Feng, S. Li, H. Li, J. Zhai, Y. Song, L. Jiang, D. Zhu, *Angew. Chem. Int. Ed.* **2002**, *41*, 1221.

[72] C. Neinhuis, W. Barthlott, *New Phytologist* **1998**, *138*, 91.

[73] S. Herminghaus, *Europhys. Lett.* **2000**, *52*, 165.

[74] R. N. Wenzel, *Ind. Eng. Chem.* **1936**, *28*, 988.

[75] R. N. Wenzel, J. Phys. Chem. **1949**, *53*, 1466.

[76] A. Lafuma and D. Quéré, *Nat. Mater.* **2003**, *2*, 457.

[77] J. Bico, U. Thiele and D. Quéré, *Colloids Surf. A* **2002**, *206*, 41.

[78] N. Patankar, *Langmuir* **2003**, *19*, 1249.

[79] A. Marmur, *Langmuir* **2003**, *19*, 8343.

[80] A. B. D. Cassie, S. Baxter *Trans. Faraday Soc.* **1944**, *40*, 546.

[81] R. E. Johnson, R. H. Dettre, in *Contact angle, Wettability and Adhesion, Advances in Chemistry Series, American Chemical Society*, Washington DC, **1964**, vol. 43, pp. 112–135.

[82] D. Öner, T. J. McCarthy, *Langmuir* **2000**, 16, 7777.

[83] Weimin Liu *J. Am. Chem. Soc.* **2005**, 127, 15670

[84] Jiang L. et al. *Angew Chem. Int. Ed.* **2004**, 43, 357

[85] A. Mills and S. Le Hunte, *J. Photochem. Photobiol.*, A: Chem., **1997**, 108,1

[86] A. Sobczynski, L. Duczmal and W. Zmudzinski, *J. Photochem Photobiol., A: Chem.*, **2004**, 213, 225

[87] H. Ibrahim and H. de Lasa, *React. Kinet. Catal.*, **2004**, 50, 1017.

[88] C. H. Kwon, H. Shin, J. H. Kim, W. S. Choi and K. H. Yoon, *Mater. Chem. Phys.*, **2004**, 86, 78

[89] M. R. Hoffman, S. T. Martin, W. Y. Choi and D. W. Bahnemann, *Chem. Rev.*, **1995**, 95, 69.

[90] A. Hagfeldtt and M. Gratzel, *Chem. Rev.*, **1995**, 95, 49.

[91] A.Fujishima, K. Hashimoto and T. Watanabe, *TiO2 Photocatalysis Fundamentals and Applications*, BKC, Tokyo, **1999**.

[92] R. Wang, K. Hashimoto, A. Fujishima, M. Chikuni, E. Kojima, A. Kitamura, M. Shimohigoshi and T. Watanabe, *Nature*, **1997**, 338, 431

[93] A. Mills, A. Lepre, N. Elliot, S. Bhopal, I. P. Parkin and S. A. O'Neill, *J. Photochem. Photobiol., A: Chem.*, **2003**, 160, 213.

[94] B. Sun and P. G. Smirniotis, *Catal. Today*, **2003**, 88, 49.

# Chapter 3

# Experimental

## 3.1 Part A

### 3.1.1 Materials

1. 2,2-bis(3,4-dihydro-3-phenyl-2H-1,3-benzoxazine) propane(BA-a)

   ：Shikoku Chemicals Corp.,Japan

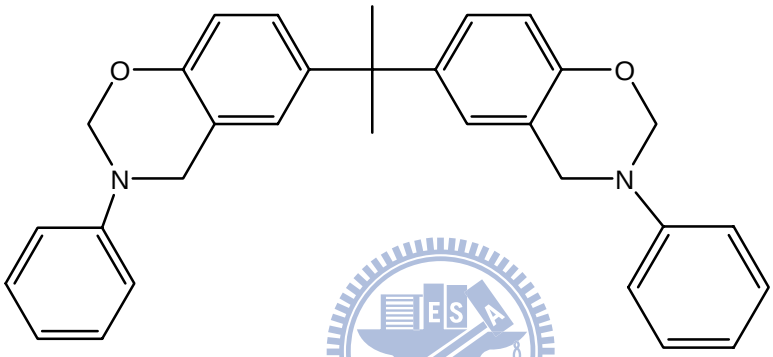


2. $TiO_2$ nanoparticles , AEROXIDE® $TiO_2$ P25, were purchased from the Degussa Corporation. The size of nanoparticle is a 21nm
3. Tetrahydrofurane ( THF )：J.T. Baker, 100%：FW=72.11, d=0.886 g/cm3, b.p.=66℃
4. Aluminum Alloys: Pan-Folks Corporation,Taiwan:96%
5. Ethanol：TEDIA, 99.9%：FW=46.07, d=0.789 g/cm3, b.p.= 78.4℃
6. Acetone：LEDA, 99.5%：FW=58.08, d=0.79 g/cm3, b.p.=56.29℃

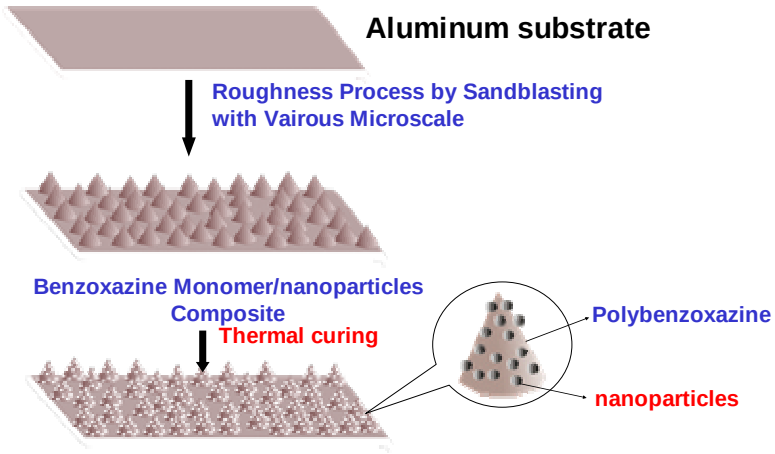


Figure 3.1. Flow diagram of the processing of superhydrophobic films by sandblasting.

### 3.1.2 Fabrication of Superhydrophobic Surfaces by Sandblasting

Super-hydrophobic coating on a Al substrate was performed through a two-step process. Firstly, Aluminum specimens with a size of 5 cm × 5 cm × 0.1 cm were cut from a rolled aluminum sheet(96.0%). Then they were etched by sandblasting with varuous roughness. The roughness of Al surface to was changed as 0.4 , 0.8 , 1 , 2 , 4 , and 6 μm to control the super- hydrophobic property of Al surface.

Secondly ,the BA-a benzoxazine (0.5 g) was mixed with nanoparticles (0.5 g) in tetrahydrofuran (THF) (10 mL). After keeping the solutions in ultrasound for 30min, the mixture was spin-coated on a Al sheet (50 × 50 × 1 mm) at 1500 rpm for 45 s and then cured in an oven at 240 °C for 1 h. The flow diagram of the film processing is shown in Figure 3.1

## 3.2 Part B

### 3.2.1 Materials

1. 2,2-bis(3,4-dihydro-3-phenyl-2H-1,3-benzoxazine) propane(BA-a)

   ：Shikoku Chemicals Corp.,Japan

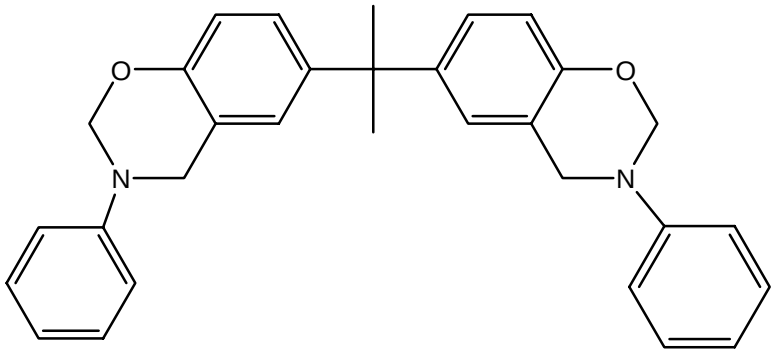


2. Silica nanoparticles, Tokusil 233G, were kindly provided by Oriental Silicas Corp. The nanoparticle is a precipitate hydrated silica with a ultimate particle size of 22 nm.
3. $TiO_2$ nanoparticles , AEROXIDE® $TiO_2$ P25, were purchased from the Degussa Corporation. The nanoparticle is a 21nm
4. Tetrahydrofurane ( THF )：J.T. Baker, 100%：FW=72.11, d=0.886 g/cm3, b.p.=66℃
5. Aluminum Alloys: Pan-Folks Corporation,Taiwan:96%
6. Ethanol：TEDIA, 99.9%：FW=46.07, d=0.789 g/cm3, b.p.= 78.4℃
7. Acetone：LEDA, 99.5%：FW=58.08, d=0.79 g/cm3, b.p.=56.29℃

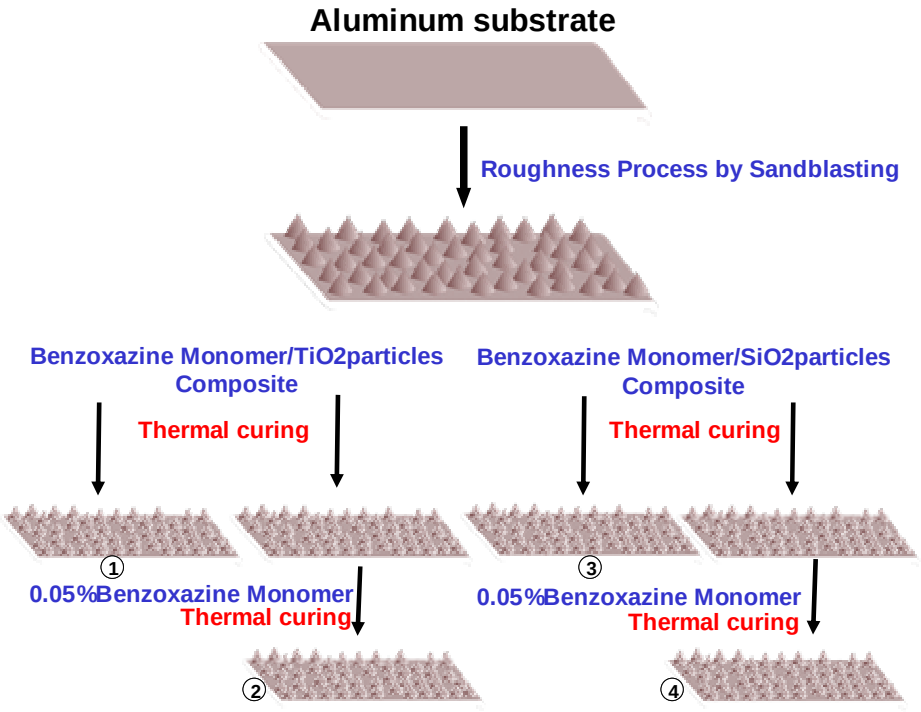


Figure 3.2. Flow diagram of the processing of superhydrophobic films with photocatalytic coatings

### 3.2.2 Photocatalytic Coatings on Superhydrophobic Surfaces

Super-hydrophobic coating on a Al substrate was performed through a four-part process(①②③④). Firstly, Aluminum specimens with a size of 5 cm × 5 cm × 0.1 cm were cut from a rolled aluminum sheet(96.0%). Then they were etched by sandblasting with the roughness is 6 μm.

Secondly ,the BA-a benzoxazine (0.5 g) was mixed with nanoparticles ($TiO_2$ and $SiO_2$)(0.5 g) in tetrahydrofuran (THF) (10 mL) respectively. After keeping the solutions in ultrasound for 30min, the mixture was spin-coated on a Al sheet (50 × 50 × 1 mm) at 1500 rpm for 45 s and then cured in an oven at 240 °C for 1 h.

Subsequently, the polybenzoxazine hybrid surface(②④) was modified with the

pure BA-m polybenzoxazine film. BA-m benzoxazine solution having 0.05% concentrations was spin-coated onto a rough surface for 45 s at 1500 rpm then been cured at 240 °C for 60 mins.The flow diagram of the film processing is shown in Figure 3.2

## 3.3 Part C

**Preparation of PVPh/PMMA Random and Block Copolymers and Blends.**

The detailed synthesis procedures of PVPh-r-PMMA and PVPh-b-PMMA copolymers have been reported previously[1]. Table 3-1 lists the characterizations of PVPh, PMMA, and PVPh/PMMA random and block copolymers. Various binary PVPh/PMMA blend compositions were prepared by solution-casting. A THF solution containing 5 wt % polymer was stirred for 6-8 h and then cast onto a wafer. The solution was left to evaporate at 60°C for 1 day and dried in vacuum at room temperature for 2 days. The thermal treatment was carried out by placing the as-prepared polymer film in a vacuum oven at 180 °C for 24 h and then quenching to ambient temperature

Table 3-1. Formulations and thermal properties of PVPh-*co*-PMMA copolymers and corresponding Blends

| copolymer | phenol ratio[a] (mol %) | *M*n [b] | *M*w/*M*n [b] | *T*g (°C) | *T*d (°C) |
|---|---|---|---|---|---|
| PMMA | 0 | 22000 | 1.29 | 105.0 | 346.5 |
| PVPh10-r-PMMA90 | 10 | 18000 | 1.85 | 130.3 | 310.7 |
| PVPh30-r-PMMA70 | 30 | 18000 | 1.64 | 143.0 | 315.6 |
| PVPh50-r-PMMA50 | 50 | 19000 | 1.68 | 151.5 | 325.9 |
| PVPh76-r-PMMA24 | 76 | 17000 | 1.51 | 166.7 | 362.0 |
| PVPh92-r-PMMA8 | 92 | 16000 | 1.67 | 173.7 | 362.1 |
| PVPh10-b-PMMA90 | 10 | 37000 | 1.15 | 143.1 | 373.3 |
| PVPh30-b-PMMA70 | 30 | 16000 | 1.11 | 155.0 | 372.0 |
| PVPh44-b-PMMA56 | 44 | 16000 | 1.15 | 163.4 | 370.5 |
| PVPh55-b-PMMA45 | 55 | 30000 | 1.10 | 164.5 | 368.0 |
| PVPh75-b-PMMA25 | 75 | 22000 | 1.13 | 176. 7 | 365.0 |
| PVPh10/PMMA90 | 10 | | | 124.4 | 359.9 |
| PVPh30/PMMA70 | 30 | | | 135.5 | 353.1 |
| PVPh50/PMMA50 | 50 | | | 147.8 | 351.8 |
| PVPh70/PMMA30 | 70 | | | 159.2 | 345.9 |
| PVPh90/PMMA10 | 90 | | | 166.8 | 343.6 |
| PVPh | 100 | 20000 | 186.8 | 1.07 | 372.1 |

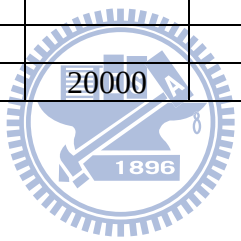

### 3.4 Experimental Equipments

#### 3.4.1 Spin Coater

SWIENCO,Type:PM490

### 3.4.2 Sandblasting Machine

CHAO SHUN ABRASIVES CO,LTD,Type:CS600

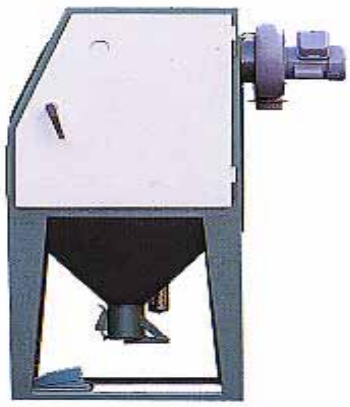

### 3.4.3 Contact Angle Measurement

The advancing contact angle of the polymer sample was measured at 25 °C using a Krüss GH-100 goniometry interfaced with image-capture software by injecting a 5 $\mu$L liquid drop. To obtain reliable contact data, at least three droplets were dispensed at different regions of the same piece of film, and at least two pieces of film were used to obtain reliable contact angle data. Thus, at least six advancing contact angles were averaged for each kind of film and each kind of liquid.

Contact angles were measured on a Krüss GH-100 contact angle goniometer. Each reported contact angles is the average of six measurements. The advancing contact angle was read by injecting a 5 $\mu$L liquid drop. The receding contact angle was measured by removing about 3 $\mu$L of liquid from the drop; the static contact angle was obtained from a 5 $\mu$L drop.

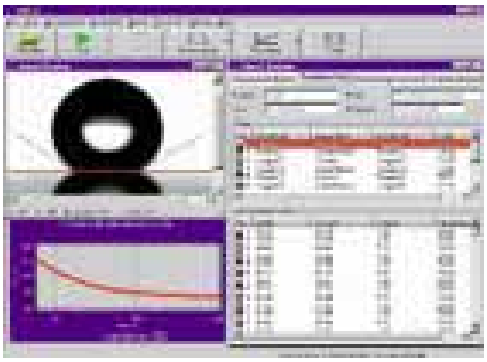

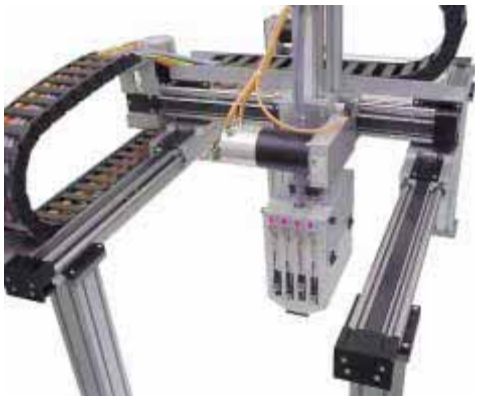

### 3.4.4 Scanning Electron Microscopy (SEM)

SEM images were carried out with a HITACHI-S-4000 scanning electron microscopy.

### 3.4.5 Surface Roughness Determinations

Roughness measurement of the surfaces was performed by using a Taylor Hobson Sutronic 25 roughness checker.

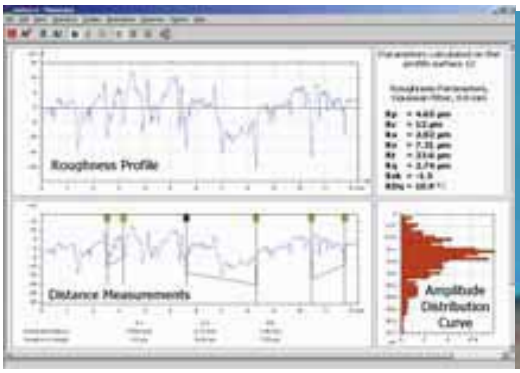


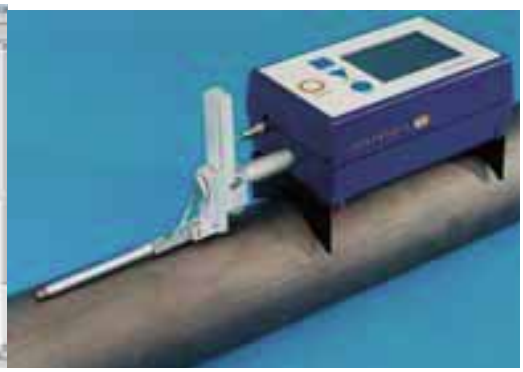

### 3.4.6 Nuclear Magnetic Resonance (NMR)

1H NMR and 13C NMR spectra were recorded on a Varian Unity Inova 500 FT NMR spectrometer operating at 500 MHz; chemical shifts are reported in parts per million (ppm). CDCl3 or C4D8O2 were used as the solvents.

### 3.4.7 Fourier Transform Infrared Spectroscopy (FTIR)

All infrared spectra were recorded using a Nicolet Avatar 320 FTIR spectrophotometer; 32 scans were collected at a spectral resolution of 1 cm-1 under nitrogen purge. FTIR spectra of the polymer films were determined using the conventional potassium bromide (KBr) plate method. Each sample was prepared by casting a THF solution directly onto a KBr plate. All films were sufficiently thin to exist within the absorbance range in which the Beer–Lambert law is obeyed.

### 3.4.8 Thermogravimetry Analysis (TGA)

Thermal stabilities of as prepared samples were investigated using a DuPont 2050 TGA instrument operated at a rate of 20 °C/min from 30 to 800 °C under a nitrogen flow.

### 3.4.9 Atomic Force Microscopy (AFM)

Atomic force microscopy (AFM) images were acquired using a Digital Instruments DI5000 scanning probe microscope in the tapping mode. Damage to both the tip and the sample surface was minimized by employing the AFM in the tapping mode. The values of root-mean-square (rms) roughness were calculated over scan area of 5 μm × 5 μm.

## References

[1]. Lin, C. L.; Chen, W. C.; Liao, C. S.; Su, Y. C.; Huang, C. F.; Kuo, S. W.; Chang, F. C. *Macromolecules* **2005**, 38, 6435

# Chapter 4

# Results and Discussion

Superhydrophobic surface of solid is an important property and depends both on the surface chemistry (low surface free energy) and on the surface roughness. Recently, superhydrophobic surfaces with water contact angles larger than 150° have received a lot of research attention, due to their important applications ranging from self-cleaning materials to microfluidic devices. The archetype superhydrophobic surface is that of the lotus leaf, on which a water droplet apparently forms a sphere, unstably sitting on the leaf, and dirt is easily removed with a rain shower. This behavior, known as the lotus or self-cleaning effect, is found to be a result of the hierarchical rough structure, as well as the wax layer present on the leaf surface. In this section, we introduce a simple method for fabricating a lotus-like micro–nanoscale binary structured surface of aluminum. The microstructure on aluminum substrate was generated by sandblasting and the nanoscale was produced by spin-coating with a mix solution of $TiO_2$ particles and polybenzoxazine. By this process, superhydrophobic surfaces on aluminum substrate with contact angle for water larger than 150 and a sliding angle (SA) less than 10° can be obtained. Besides, we discovered that a series of poly(vinylphenol-*co*-methylmethacrylate) (PVPh-*co*-PMMA) block and random copolymers possess extremely low surface energy after a simple thermal treatment procedure, even lower than that of poly(tetrafluoroethylene) (22.0 $mJ/m^2$) calculated on the basis of the two-liquid geometric method.

## 4.1 Composite Rough Surfaces

The shape of a water drop on BA-a and surface-modified aluminum surface with nanoparticles can be seen in Figure 4.1. On smooth BA-a thin film, the water contact angle $\theta$ was 108° (Figure 4.1a) The water contact angle, $\theta$, was 160±3° for

superhydrophobic surface prepared by $TiO_2$ nanoparticles and surface modified aluminum substrates (Figure 4.1b). From SEM images, we find that $TiO_2$ nanoparticles and surface modified aluminum substrates form nanometer and micrometer two scale structure (Figure 4.2). Besides, the nanometer-sized $TiO_2$ particles formed secondary layer which covered the aluminum surface homogeneously. However, the contact angle, $\theta$ , is related to mass ratio of $TiO_2$ nanoparticles. Figure 4.3 shows the corresponding $\cos\theta$ with different mass percent of nanoparticles in 5 % BA-a solution concentrations. With increasing mass percent, $\cos\theta$ first decreased slowly ( $\theta$ increased slowly ), then decreased rapidly above the mass ratio of 60/100, and then decrease slowly until $\theta$ reached the value of 160°. The observed transition was dependently on mass % of nanoparticles. As the mass % of nanoparticles increased from 60/100($TiO_2$/BA-a) ratio to 80/100 (TiO2/BA-a) ratio, the transition shifted to a smaller mass percent of particles. The concentration of particles at the onset of the transition was at 80/100 ($TiO_2$/BA-a) ratio. This suggests that, above a critical particle concentration of 80/100 ($TiO_2$/BA-a) , either the surface composition or the surface roughness changed significantly resulting in a sharp decrease in $\cos\theta$. A critical particle concentration was also observed in which the surface composition effect of aluminum was eliminated by coating only nanoparticles from solutions of varying ratio on rough aluminum substrates. The particles did not cover the aluminum surface completely below a concentration of 80/100 ($TiO_2$/BA-a), and the water contact angle was nearly 120°, similar to that on the bare flat substrate. Above a concentration of 80/100 ($TiO_2$/BA-a) in a 5% BA-a concentration, the contact angle increased and reached the value of 160°. These observations confirmed that the fraction of particles on the surface increased above a critical value until the surface was completely covered by particles.

## 4.2 The Explanation of Superhydrophobic State by Wenzel，s Model and Cassie-Baxter Model

On the basis of data we mention above, we conclude that the reason for the transition as a function of mass percent of particles in Figure 4.3 is the significant change of surface composition from bare to covered surface with nanoparticles. The result of SEM measurements (Figures 4.4) supported this conclusion. In the system of BA-a + nanoparticles, BA-a covered the underlying solid substrate uniformly and changed the surface chemistry of the substrate. Thus, water contact angles were close to 92° at a low mass percent of nanoparticles. The nanoparticle aggregates were dispersed on top of this rough aluminum layer. The surface fraction of the particle aggregates increased with increasing mass percent of particles. Figure 4.4(e) corresponds to a film containing 80/100 ($TiO_2$/BA-a) ratio with a 5% BA-a concentration which is located at the the transition region (Figure 4.3). The height of the particle aggregates stayed constant but the overall surface roughness increased compared to that in Figure 4.4(a) because the surface fraction of particle containing rough regions increased. Figure 4.4(f) shows that the surface was completely covered by particle aggregates for a film containing 100/100 ($TiO_2$/BA-a) ratio with a 5% BA-a concentration ($\cos\theta$ = -0.94 in Figure 4.3).

SEM measurements of 6μm × 8μm area helped the surface profile of the films to be understood quantitatively at small length scales. However, the surface profile at larger length scales is also important in surface hydrophobicity and contact angle measurements depending on the water drop size. Because the typical water drop size was 5μL in the measurements, the contact angle data of Figure 4.3 represents contributions from～$mm^2$ area. We measured larger area pictures of the film surfaces by SEM. Figure 4-5(a)(b) show SEM pictures of an area of 60 $\mu$m × 80 $\mu$m for bare rough aluminum and the film containing 100/100 ($TiO_2$ /BA-a) ratio having a 5% BA-a concentration.

The Figure 4-5(c) is the magnified view of the same region (b) corresponding to an area of $6\,\mu\text{m} \times 8\,\mu\text{m}$. The existence of two regions, darker and lighter areas, is clearly seen. The lighter areas are the regions where the nanoparticles were densely populated, as shown in Figure 4-5(c). The darker areas correspond to regions where some nanoscale roughness are seen, as shown in Figure 4-5(c). Because the size of these regions is much smaller than the size of the water drop ($5\,\mu\text{L}$), their contributions to the contact angle are averaged out.

For the two-component system of microrough surface + nanoparticles, microscopy investigations clearly show that the surface fraction of components changed nonlinearly with the mass fraction in the films. The reason of this nonlinearity is the large aggregate formation of nanoparticles in the film after curing. Nanoparticles formed nanoscale roughness. BA-a covered the substrate surface as a thin film and nanoparticle aggregates dispersed on BA-a film. Below the transition,the surface consisted of a continuous matrix of BA-a film with nanoparticle islands on it. Thus, the contact angles were close to that of BA-a and increased slowly with increasing mass percent of nanoparticles. The change of surface composition resulted in a change in surface roughness as the number of aggregates on the surface increased. The contribution of the surface composition to the contact angle was dominant below the transition. The transition corresponds to the point where the continuous component on the surface changed from BA-a to nanoparticles.. Beyond the transition, the surface was almost completely covered by nanoparticles. The contact angle was predominantly determined by the surface roughness and changed again slowly with mass percent.

To understand the physical mechanisms of superhydrophobicity for the composite films, the ease of sliding/rolling of a water drop down the film surface was investigated by tilting the film surface at controlled angles and observing the advancing and receding

contact angles until the drop slid/rolled. To our surprise, water drops rolled easily (at small tilt angles of less than 10°) only on the rough substrate containing 100/100 ($TiO_2$ / BA-a) ratio having a 5% BA-a concentration. Addition of even 100/100 ($TiO_2$ /BA-a) ratio on flat substrate prevented the water drops from sliding even upto 90° tilt angles although the water contact angle was still high ($\theta$ = 126°). Interaction of water with BA-a together with chemical and topographical heterogeneity of the BA-a + nanoparticle film surfaces is expected to contribute to strong pinning of the drop. Large static contact angles with a large pinning force that prevented sliding of water drops at 90° tilt angles have also been observed previously on different roughness systems.

Figure 4-6 and Figure 4-7 show the CA and CAH, $\triangle\theta = \theta a - \theta r$, as a function of roughness of aluminum containing 100/100 ($TiO_2$ /BA-a) ratio having a 5% BA-a concentration. Films could not be prepared above 100/100 ($TiO_2$/BA-a) ratio because of powder formation. In the beginning, the CAH increased almost linearly with the roughness of aluminum.Then the CAH decreased slowly with the roughness of aluminum. The film at large microroughness(2 $\mu$m) indicates a transition from the Wenzel regime to the Cassie-Baxter regime in which the CAH decreases with increasing roughness.

The CA is calculated according to the two theory that emphasizes the concept of contact angle amplification both in Wenzel and in Cassie-Baxter regimes. In the calculation, the contact angle on the smooth BA-a surface was taken as 108°. For BA-a + nanoparticle composites above 80/100 ($TiO_2$/BA-a) ratio, the contact angles of composite surfaces ($\theta$ smooth) were calculated using the Cassie-Baxter formula (eq 2.32) which takes into account the surface composition. Assuming the composite surfaces are in the Wenzel regime, the roughness factor r was determined using eq 2.33, by dividing experimentally determined $\cos\theta^{\text{rough}}$ by $\cos\theta^{\text{smooth}}$. I, thus, conclude that the observed CAH increase with the roughness of aluminum indicates that the surfaces remain in the

Wenzel regime up to 80/100 ($TiO_2$/BA-a) ratio. Static contact angles increase with increasing surface roughness both in the Wenzel and in the Cassie-Baxter regimes, but the behavior of the CAH goes in opposite directions in the two regimes. In the Wenzel regime the CAH increases with increasing roughness, and in the Cassie-Baxter regime it decreases with increasing roughness. The CAH above 80/100 ($TiO_2$ / BA-a) ratio can be interpreted as evidence of a transition from the Wenzel to the Cassie-Baxter regime.

### 4.3 Photocatalytic Coatings on Superhydrophobic Surfaces

In the part, We introduce the photocatalytic concept to our superhydrophobic system. These $TiO_2$/BA-a composite were found to operate under the UV light irradiation indoor as the efficient photocatalyst for the degradation of organic compounds in the air finally into the inert $CO_2$ and $H_2O$. Fig. 4.8 shows the time profiles of the photocatalytic degradation of dirt attached on the surface of $TiO_2$/BA-a composite obtained by monitoring the contact angle.The CA of superhydrophobic surfaces on ③ and ④ of $SiO_2$/BA-a composite without $TiO_2$ was reduction gradually. However, on the ① $TiO_2$/BA-a composite exposed in the air the CA didn't decreased with time under UV light irradiation and finally, dirt decomposed through the photocatalytic reaction of $TiO_2$ on the surface.

Fig. 4.8 shows the profiles of time with CA. The water contact angle on the ① was very large, indicating that ① $TiO_2$/BA-a composite still has the super-hydrophobic surface. The addition of $TiO_2$ photocatalysts on the ② ,$TiO_2$/BA-a composite coating with BA-a 0.05% concentrations, caused the water contact angle to be larger than that of the original ① ,because $TiO_2$ particles exposed in the air is under the cover of BA-a having 0.05% concentrations. Such hydrophobicity on the ②, ③ and ④ decreased

dramatically after exposing in the air for weeks .because of adsorbed compounds of pollutants.

The dirty adsorbed on the surface in the air was decomposed photocatalytically and, furthermore, the super-hydrophobic properties often observed in ①. The UV irradiation indoor is about 5% of the quantity outdoor. On the other hand, in the case of the ① with a smaller CA than ② at firstly, the value was recovered gradually with proceeding the photocatalytic degradation of the dirt to regenerate the super-hydrophobic surface. These phenomena and their mechanism are summarized in Fig. 4.9. The attachment of dirt on the $SiO_2$/ BA-a surface decreased the water contact angle dramatically, but on the $TiO_2$/BA-a with a small amount of $TiO_2$ exposed in the air can recover their super-hydrophobic surface by the photocatalytic degradation of the dirt under the UV light irradiation. This self-cleaning effect to recover the super-hydrophobic surface is effective only on the surface of the $TiO_2$/BA-a sample, ① ,with a small amount of $TiO_2$ exposing in the air, because the super-hydrophobic properties will occur on the UV light irradiated $TiO_2$ on the $TiO_2$/BA-a sample.

### 4.4.1 The effect of hydrogen bonding and sequence distribution in PVPh/PMMA system

Formulations and thermal properties of these synthesized copolymers are summarized in Table 4-1. It is well-known that a high temperature above *T*g tends to partially disrupt hydrogen bond formation, and this is why we chose 180°C as the thermal treatment temperature and 180°C are far lower than the decomposition temperature (Table 4-1), thus the thermal treatment should not damage the polymer structure. Table4-2 lists the surface roughness, advancing contact angles, and surface free energies of all specimens, before and after thermal treatment. The surface roughnesses of all

specimens are lower than 5 nm; therefore, the influence of topography on the surface free energy is negligible. The advancing contact angle is relatively less sensitive to surface roughness and heterogeneity than the receding angle; thus, the advancing contact angle data are commonly used to calculate the components of surface and interfacial tension.[6,7] In our previous study, we have found that the surface free energy of PVPh homopolymer decreases substantially after thermal treatment, resulting in a significant decrease in surface free energy (from 41.8 to 15.7 mJ/m2) and the sequence distribution of the vinylphenol group in PVPh-*co*-PS copolymers plays an important role in dictating the final surface energy after thermal treatment. In this paper, we change the immiscible PVPh-*co*-PS copolymer to miscible PVPh-co-PMMA copolymer to investigate the effect of hydrogen bonding between PVPh and PMMA on the surface free energy. Before we discussed the effect of hydrogen bonding between PVPh and PMMA on the surface free energy we studied the preparing process effect of hydrogen bonding first.

From Figure 4.11, we find pure PVPh homopolymer possesses quiet different FTIR spectrum after different preparing process. Different from solvent casting process, the PVPh homopolymer prepared from spin coating process possessed higher content of the free hydroxyl group and the hydroxyl groups involved in intramolecular hydrogen bonding. According to previous studies, solvent-cast films from volatile solutions such as chloroform, toluene or tetrahydrofuran may not be thermodynamically equilibrated due to rapid solvent evaporation during the spin-casting process, and the resulting surface could primarily be the result of solvent effects.[8,9] Thus, the PVPh homopolymer prepared from spin coating process possessed higher content of the free hydroxyl group and the hydroxyl groups involved in intramolecular hydrogen bonding than it prepared from solvent casting. In our previous report,[7] it is more favorable to re-form hydrogen bonds from neighboring hydroxyl groups or those in the vicinity (most likely from the same

chain, defined as an intramolecular hydrogen bond) in PVPh system. This is probably the reason for PVPh homopolymer prepared from 180°C thermal treatment possessed higher content of the free hydroxyl group and the hydroxyl groups involved in intramolecular hydrogen bonding than it prepared from spin coating process.

For PVPh-co-PMMA copolymer system, we have reported that the hydrogen-bonding strength of poly (vinylphenol-*co*-methyl methacrylate) copolymers depended on sequence distribution and polydispersity index due to its intramolecular screening and functional group accessibility effects.[2]The FTIR spectra shown in Figure 4.12 a and 4.12 b are good evidences for intramolecular screening and functional group accessibility effects. However, the FTIR spectra shown in Figure 4.12 c and 4.12 d are quiet different from Figure 4.12 a and 4.12 b. The carbonyl stretching band for PMMA appears at 1730 cm-1 and the peak at 1705 cm-1 corresponding to the hydrogen-bonded carbonyls and they can be fitted well to the Gaussian function (Table 4-3). From Figure 3c, we can find that the hydrogen-bonded carbonyls are few in PVPh/PMMA blends and PVPh-PMMA block copolymer except in PVPh-PMMA random copolymer. Furthermore, we find the similar phenomenon in the FTIR spectra of all polymer films (Figure 4.13) which prepared by spin coating process. From mention above, the reason for this phenomenon is due to rapid solvent evaporation during the spin-casting process.[8,9] We deduced that it is more favorable to form hydrogen bonds from neighboring hydroxyl groups and carbonyls during the rapid evaporation of tetrahydrofuran. As a result, there is more hydrogen-bonded carbonyl can be found in PVPh-PMMA random copolymer. From Table 3, we find all polymer specimens possess lower surface free energy after thermal treatment. In our previous report, we deduced that the decrease of surface energy is due to the decrease of the intermolecular hydrogen-bonding interaction for PVPh/PMMA system. For clarity, the spectra display the hydroxyl stretching region

between 2800 and 3800 $cm^{-1}$ and the carbonyl stretching region between 1660 and 1800 $cm^{-1}$ are shown in Figure 4.14, 4.15 and 4.16. According to a recent study,[10] the -OH band can be fitted by three Gaussian functions: a narrower shoulder band at 3525 cm-1 represents the free hydroxyl group, the peak at *v* 3280 cm-1 corresponds to the hydroxyl groups involved in intermolecular hydrogen bonding, and the peak at *v* 3420 cm-1 corresponds to the hydroxyl groups involved in intramolecular hydrogen bonding. Besides, the peaks at 1730 and 1705 cm-1 corresponding to the free carbonyl and hydrogen-bonded carbonyls and the band at 3440 cm-1 represents the hydroxyl groups interacting with carbonyl groups. [2] We find all polymer films possess fewer fractions of the hydroxyl groups involved in intermolecular hydrogen bonding resulting in lower surface free energy after thermal treatment in Figure 4.15. Most of intermolecular hydrogen bondings of hydroxyl groups convert into free hydroxyl groups, intramolecular hydrogen bonding and hydrogen bonding between hydroxyl groups and carbonyl groups after thermal treatment.

In our previous work,[11] we have studied the effect of an inert diluent segment on the immiscibility behavior of PVPh-*r*-PS copolymers and found that the incorporation of a styrene moiety into the PVPh polymer chain can dilute and decrease the strong self-association in the PVPh component. The spacing of these vinylphenol groups tends to decrease the average hydroxyl-hydroxyl distance and increase the fraction of free hydroxyl in PVPh/PS random copolymers and provides a positive effect to lower the surface energy of the polymer. However, the contact angles and resulting $\gamma$ of PVPh/PS blends show no significant change before or after 180 °C thermal treatment in PVPh/PS systems.[1] We find miscible polymers, PVPh-co-PMMA, with different sequence distribution present different surface properties from immiscible PVPh-co-PS copolymers because of its hydrogen bonding between hydroxyl groups and carbonyl groups. It is

interesting to note that the surface free energy of PVPh/PMMA blends increase with the increasing of PMMA content (Figure 4.17). The PVPh-*r*-PMMA and PVPh-b-PMMA copolymers possess the most drastic reduction in surface energy after the thermal treatment in comparison with corresponding blends under comparable compositions. In the PVPh/PS systems, the interference of the styrene segment tends to prevent the vinylphenol segment from migrating to the surface, which can be regarded as a negative effect, i.e., an increase in the surface energy of the material. Thus, the PVPh-*r*-PS copolymers possess the most drastic reduction in surface energy after the thermal treatment in comparison with corresponding block copolymers and blends under comparable compositions. From the second-run DSC data of both PVPh-*co*-PMMA copolymers and PVPh/PMMA blends, revealing that essentially all PVPh/PMMA specimens possess only one glass transition temperature. Single glass transition temperature strongly suggests that these systems are fully miscible and possess a homogeneous amorphous phase. Besides, it have been reported that hydrogen bonding interaction would reduce surface enrichment.[12] As a result, there is no surface enrichment occurs in PVPh/PMMA blends and block copolymers.

To further investigate the importance of hydrogen bonding between the hydroxyls and carbonyls, we turn our attention back to the FTIR spectra of the carbonyl stretching region between 1660 and 1800 cm-1 of PVPh/PMMA random and block copolymers and their corresponding blends were shown in Figure 4.16. From Figure 4.16, we clearly know that the fraction of hydrogen bonded carbonyl group increases after 180°C 24h thermal treatment. It indicates that we increase the interaction between PVPh and PMMA after thermal treatment. For PVPh/PMMA random and block copolymers we speculated that it is more favorable to re-form hydrogen bonds from neighboring hydroxyl groups or carbonyl groups in the vicinity (most likely from the same chain, defined as an

intramolecular hydrogen bond) resulting in the most drastic reduction in surface energy after the thermal treatment. Unlike PVPh/PMMA random and block copolymers, the surface free energy of PVPh/PMMA blends increases with the increasing of PMMA content (Figure 4.17). Different from PVPh (after 180°C 24 h thermal treatment), PMMA homopolymer possessed higher surface free energy. In addition, intermolecular hydrogen bonding between hydroxyl groups and carbonyls increased after 180°C 24 h thermal treatment. Thus, the surface free energy of PVPh/PMMA blends increases with the increasing of PMMA content

### 4.4.2 Conclusions

An easy method was used for the preparation of a $TiO_2$ photocatalyst on the superhydrophobic surface. Small amounts of $TiO_2$ photocatalyst prepared on BA-a led to the purification of the surface by the photocatalytic degradation of the attached pollutants under UV light irradiation, so that it could recover the super-hydrophobic property of surface. The $TiO_2$/BA-a is promising for the applications in waterproof materials because it has water-repellent properties induced by BA-a and the self-cleaning properties induced by $TiO_2$ photocatalyst.

The decrease of the intermolecular hydrogen-bonding fraction between hydroxyl groups of PVPh in PVPh/PMMA systems through a simple thermal treatment procedure tends to decrease the surface energy. The sequence distribution of the vinylphenol group in PVPh-co-PMMA copolymers plays an important role in dictating the final surface energy after thermal treatment. Besides, there is no surface enrichment occurs in PVPh/PMMA systems because of its hydrogen bonding between hydroxyl groups and carbonyl groups. The effects of molecule weight on surface free energy were also investigated carefully in this paper

## References


[1]. Lin, H. C.; Wang, C. F.; Kuo, S. W.; Tung, P. H.; Huang, C. F.; Lin, C. H.; Chang, F. C. *J. Phys. Chem. B* **2007**, 111, 3404.

[2]. Lin, C. L.; Chen, W. C.; Liao, C. S.; Su, Y. C.; Huang, C. F.; Kuo, S. W.; Chang, F. C. *Macromolecules* **2005**, *38*, 6435.

[3]. D. G. LeGrand, G. L. Gaines, Jr., *J. Colloid Interface Sci.* **1969**, 31, 162.

[4]. D. G. LeGrand, G. L. Gaines, Jr., *J. Colloid Interface Sci*. **1973**, 42, 181.

[5]. S. Wu, *J. Colloid Interface Sci*. **1969**, 31, 153.

[6]. Xu, Y.; Graf, J.; Painter, P. C.; Coleman, M. M. *Polymer* **1991**, 32, 3103.

[7]. Wang, L. F.; Pearce, E. M.; Kwei, T. K. *J. Polym. Sci., Polym. Phys. Ed*. **1991**, 29, 619.

[8]. Garbassi, F.; Morra, M.; Occhiello, E. *Polymer Surfaces: from Physics to Technology*; John Wiley & Sons: Chichester, **1998**; p 291.

[9]. Green, P. F.; Christensen, T. M.; Russell, T. P.; Jerome, R. J. *Chem. Phys*. **1990**, 92, 1478-1482.

[10]. Yuan, F.; Wang, W.; Yang, M.; Zhang, X.; Li, J.; Li, H.; He, B. Minch, B.; Lieser, G.; Wegner, G. *Macromolecules* **2006**, 39, 3982.

[11]. Kuo, S. W.; Chang, F. C. J. *Polym. Sci., Part B: Polym. Phys*. **2002**, 40, 1661.

[12]. Duan, Y.; Pearce, E. M.; Kwei, T. K. Hu, X.; Rafailovich, M.; Sokolov, J.; Zhou, K.;Schwarz, S. *Macromolecules*, **2001**, 34 (19), 6761-6767

Table 4-1. Formulations and thermal properties of PVPh-*co*-PMMA copolymers and corresponding Blends

| copolymer | phenol ratio[a] (mol %) | *M*n [b] | *M*w/*M*n [b] | *T*g (°C) | *T*d (°C) |
|---|---|---|---|---|---|
| PMMA | 0 | 22000 | 1.29 | 105.0 | 346.5 |
| PVPh10-r-PMMA90 | 10 | 18000 | 1.85 | 130.3 | 310.7 |
| PVPh30-r-PMMA70 | 30 | 18000 | 1.64 | 143.0 | 315.6 |
| PVPh50-r-PMMA50 | 50 | 19000 | 1.68 | 151.5 | 325.9 |
| PVPh76-r-PMMA24 | 76 | 17000 | 1.51 | 166.7 | 362.0 |
| PVPh92-r-PMMA8 | 92 | 16000 | 1.67 | 173.7 | 362.1 |
| PVPh10-b-PMMA90 | 10 | 37000 | 1.15 | 143.1 | 373.3 |
| PVPh30-b-PMMA70 | 30 | 16000 | 1.11 | 155.0 | 372.0 |
| PVPh44-b-PMMA56 | 44 | 16000 | 1.15 | 163.4 | 370.5 |
| PVPh55-b-PMMA45 | 55 | 30000 | 1.10 | 164.5 | 368.0 |
| PVPh75-b-PMMA25 | 75 | 22000 | 1.13 | 176. 7 | 365.0 |
| PVPh10/PMMA90 | 10 | | | 124.4 | 359.9 |
| PVPh30/PMMA70 | 30 | | | 135.5 | 353.1 |
| PVPh50/PMMA50 | 50 | | | 147.8 | 351.8 |
| PVPh70/PMMA30 | 70 | | | 159.2 | 345.9 |
| PVPh90/PMMA10 | 90 | | | 166.8 | 343.6 |
| PVPh | 100 | 20000 | 186.8 | 1.07 | 372.1 |

Table 4-2. Root-mean-square surface roughness, advancing contact angle for water and diiodomethane, surface Free energy, and XPS Analysis of PVPh/PMMA Copolymers

| | Before 180°C thermal treatment | | | | After efore 180°C thermal treatment | | | |
|---|---|---|---|---|---|---|---|---|
| | | Contact angle (deg) | | | | Contact angle (deg) | | |
| polymer | Roughness (nm) | $H_2O$ | DIM | $\gamma$ (mJ/m$^2$) | Roughness (nm) | $H_2O$ | DIM | $\gamma$ (mJ/m$^2$) |
| PVPh | 2.1 | 75.6 | 47.8 | 37.9 | 2.2 | 107.0 | 86.6 | 14.5 |
| PVPh/PMMA=10/90 | 1.4 | 103.4 | 48.4 | 37.0 | 1.4 | 89.5 | 60.2 | 28.7 |
| PVPh/PMMA=30/70 | 2.1 | 98.7 | 48.1 | 36.1 | 2.3 | 92.6 | 66.6 | 25.4 |
| PVPh/PMMA=50/50 | 2.0 | 95.9 | 48.5 | 35.4 | 1.8 | 96.6 | 69.3 | 23.5 |
| PVPh/PMMA=70/30 | 1.2 | 92.55 | 47.5 | 35.7 | 1.2 | 85.8 | 76.7 | 23.5 |
| PVPh/PMMA=90/10 | 1.5 | 90.2 | 48.3 | 35.2 | 1.5 | 103.5 | 80.9 | 17.3 |
| PVPh10-b-PMMA90 | 1.8 | 95.1 | 52.9 | 32.7 | 1.5 | 100.0 | 84.9 | 16.2 |
| PVPh30-b-PMMA70 | 2.1 | 91.5 | 52.3 | 33.0 | 1.7 | 103.0 | 86.7 | 15.0 |
| PVPh44-b-PMMA56 | 1.7 | 83.4 | 52.4 | 33.8 | 1.7 | 105.3 | 87.9 | 14.2 |
| PVPh55-b-PMMA45 | 1.3 | 82.3 | 53.2 | 33.7 | 1.5 | 105.8 | 88.2 | 14.0 |
| PVPh75-b-PMMA25 | 1.5 | 80.3 | 54.6 | 33.6 | 1.5 | 105.9 | 88.2 | 13.9 |
| PVPh10-r-PMMA90 | 2.3 | 101.3 | 53.1 | 33.3 | 2.1 | 102.5 | 82.6 | 16.6 |
| PVPh30-r-PMMA70 | 1.1 | 93.2 | 53.5 | 32.3 | 1.5 | 104.1 | 84.8 | 15.5 |
| PVPh50-r-PMMA50 | 1.3 | 91 | 53.5 | 32.3 | 1.3 | 105.6 | 88.5 | 13.9 |
| PVPh76-r-PMMA24 | 1.4 | 81.8 | 53.5 | 33.7 | 1.4 | 106 | 89 | 13.7 |
| PVPh92-r-PMMA8 | 1.2 | 79.6 | 53.1 | 34.4 | 1.2 | 106.3 | 89 | 13.6 |
| PMMA | 2.0 | 108.4 | 48.8 | 38.3 | | | | |

Table 4-3. Results of Curve-Fitting the Data for PVPh-*co*-PMMA and PVPh/PMMA Blends with different process at Room temperature

| copolymer | H-bonded C=O | | | Free C=O | | | |
|---|---|---|---|---|---|---|---|
| | υ, $cm^{-1}$ | $W_{1/2}$, $cm^{-1}$ | $A_{b,}$ % | υ, $cm^{-1}$ | $W_{1/2}$, $cm^{-1}$ | $A_{b,}$ % | $f_b$ [a] |
| *Solvent casting* | | | | | | | |
| PVPh/PMMA=50/50 | 1707 | 25 | 17.2 | 1732 | 19 | 82.8 | 12.2 |
| PVPh44-b-PMMA56 | 1707 | 24 | 45.8 | 1735 | 19 | 54.2 | 36.1 |
| PVPh50-r-PMMA50 | 1704 | 24 | 49.2 | 1731 | 19 | 50.8 | 39.2 |
| *Spin coating* | | | | | | | |
| PVPh/PMMA=50/50 | 1707 | 25 | 11.4 | 1731 | 19 | 88.6 | 7.9 |
| PVPh44-b-PMMA56 | 1707 | 24 | 13.8 | 1731 | 19 | 86.2 | 9.6 |
| PVPh50-r-PMMA50 | 1706 | 25 | 44.5 | 1731 | 19 | 55.5 | 34.8 |
| *180°C thermal treatment* | | | | | | | |
| PVPh/PMMA=50/50 | 1708 | 24 | 34.7 | 1731 | 19 | 65.3 | 26.2 |
| PVPh44-b-PMMA56 | 1708 | 24 | 38.9 | 1732 | 19 | 61.1 | 29.8 |
| PVPh50-r-PMMA50 | 1707 | 25 | 42.5 | 1732 | 19 | 57.5 | 33.0 |

**(a)** **(b)**

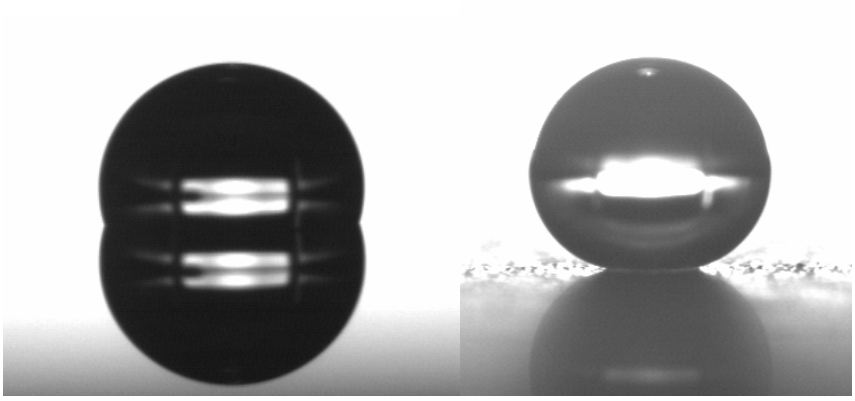

Figure 4.1. (a) Shape of a water drop (5 $\mu$L ) on the film of BA-a (left). The water contact angleθis 108 °. (b) Shape of a water drop (5 $\mu$L) on the surface of Al with nanoparticles (right). The water contact angle θ is 160±3°.

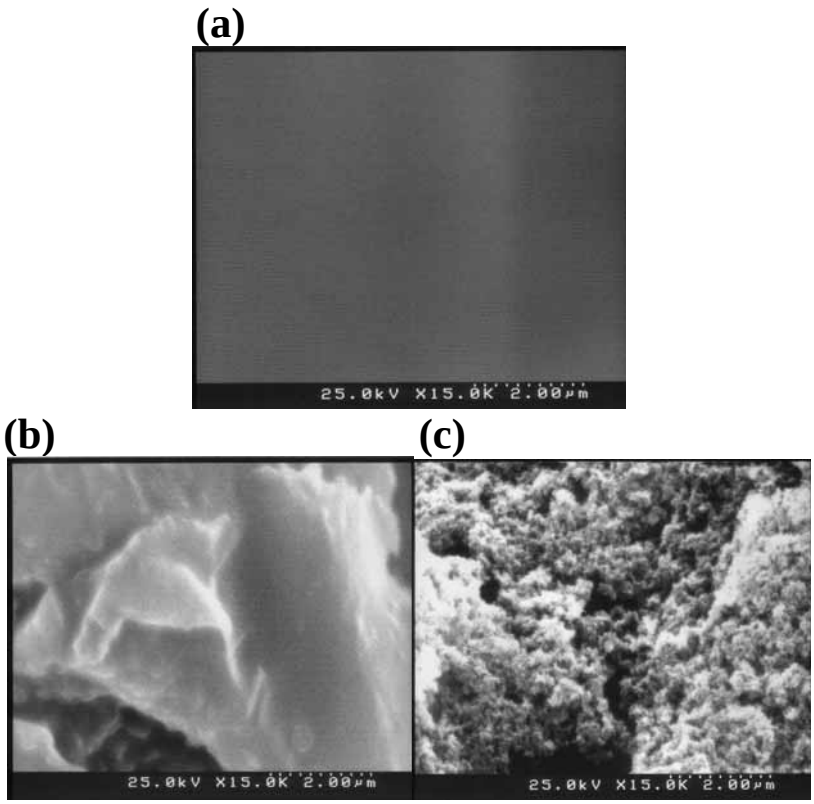


Figure 4-2. SEM images of BA-a + nanoparticle films on aluminum substrate (a) flate aluminum substrate without composite (b) sandblasting topographical microstructure on the surface of aluminum, and (c) sandblasting topographical microstructure of aluminum . Films were prepared from solutions having a 100/100 ($TiO_2$ /BA-a) ratio having 5% BA-a concentration.

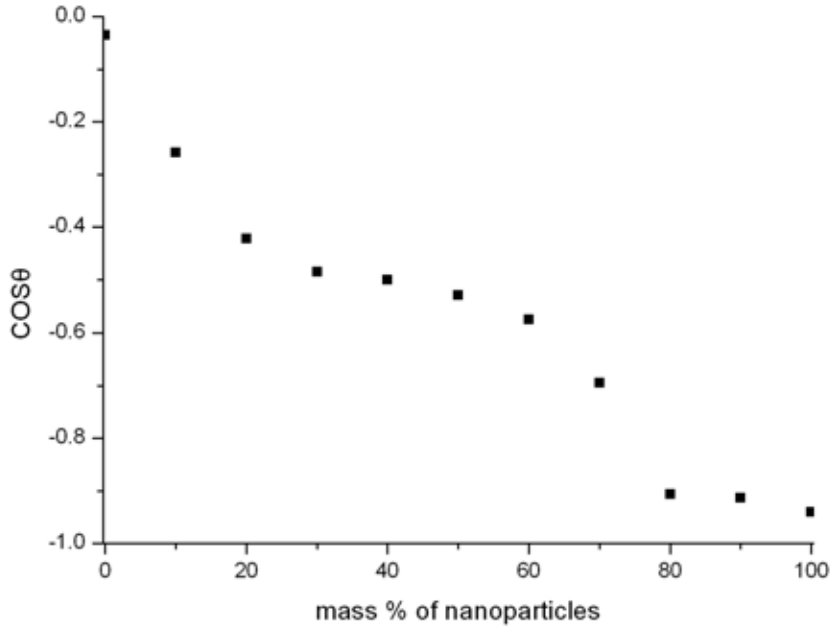


Figure 4-3. The change of cosθ with different mass ratio nanoparticles. The sharp change in contact angles occurs at different mass percentages, depending on the $TiO_2$/BA-a ratio concentration of the spin-coated solutions.

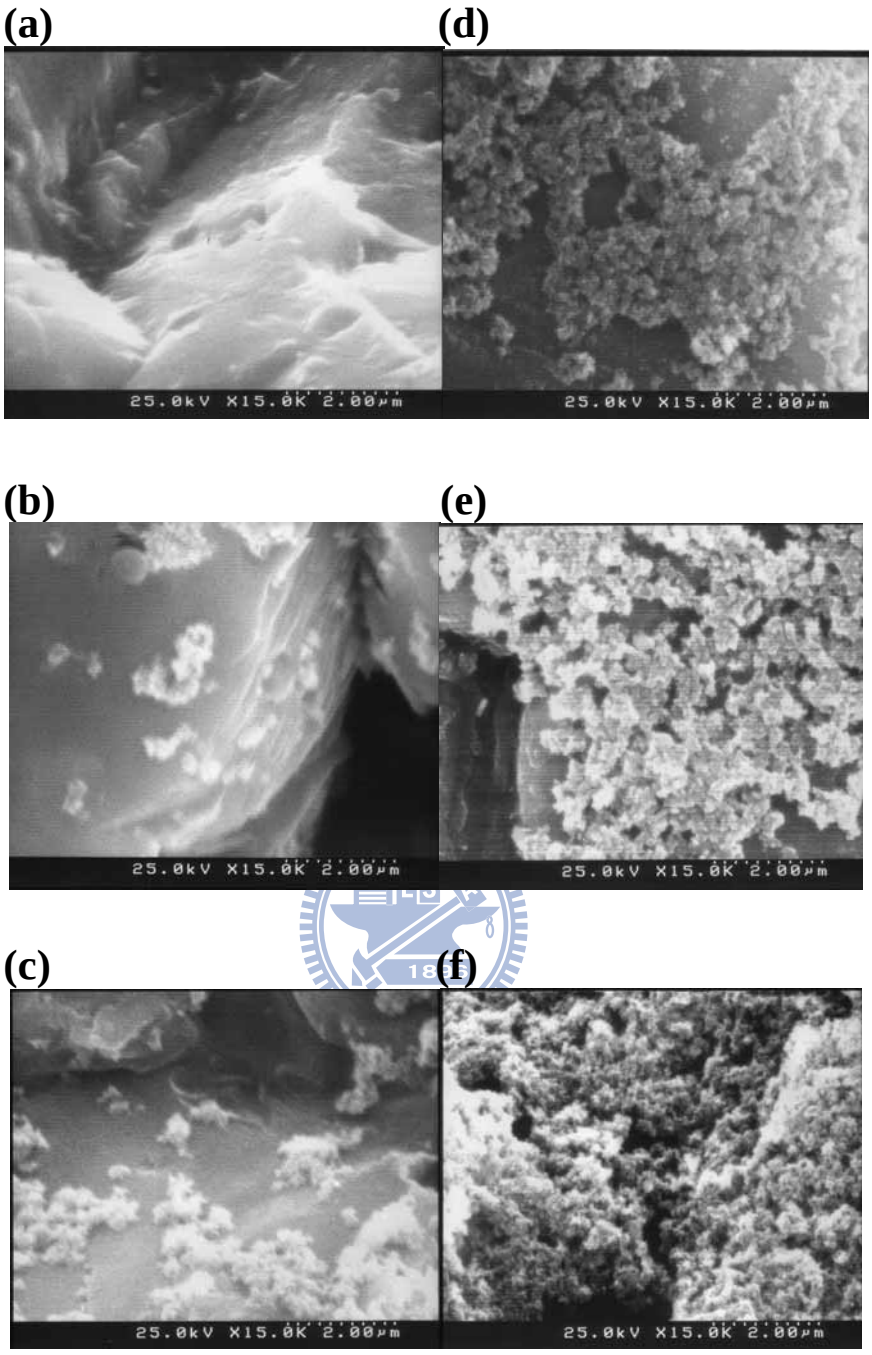


Figure 4-4. SEM image of the BA-a + nanoparticle film on rough aluminum surface, obtained from a solution having (a) a 5% BA-a concentration. (b) 20/100 ($TiO_2$ /BA-a) ratio with a 5% BA-a concentration. (c) 40/100 ($TiO_2$ /BA-a) ratio with a 5% BA-a concentration. (d) 60/100 ($TiO_2$ /BA-a) ratio with a 5% BA-a concentration. (e) 80/100 ($TiO_2$ /BA-a) ratio with a 5% BA-a concentration. (f) 100/100 ($TiO_2$ /BA-a) ratio with a 5% BA-a concentration.

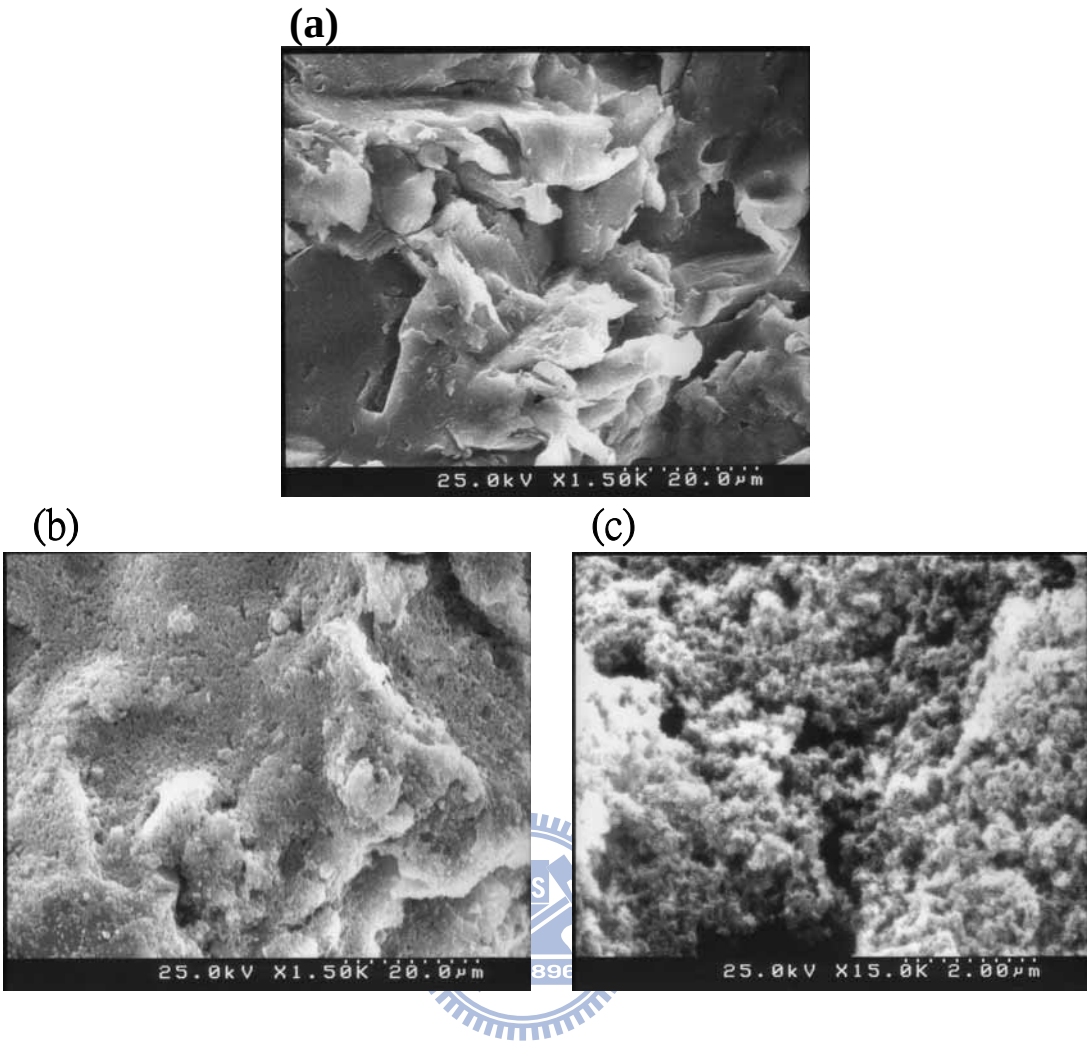


Figure 4-5. SEM pictures of (a) an area of 60μm ╳ 80μm for bare rough aluminum, (b) the rough substrate containing 100/100 ($TiO_2$ /BA-a) ratio having a 5% BA-a concentration , and (c) magnified view of (b).

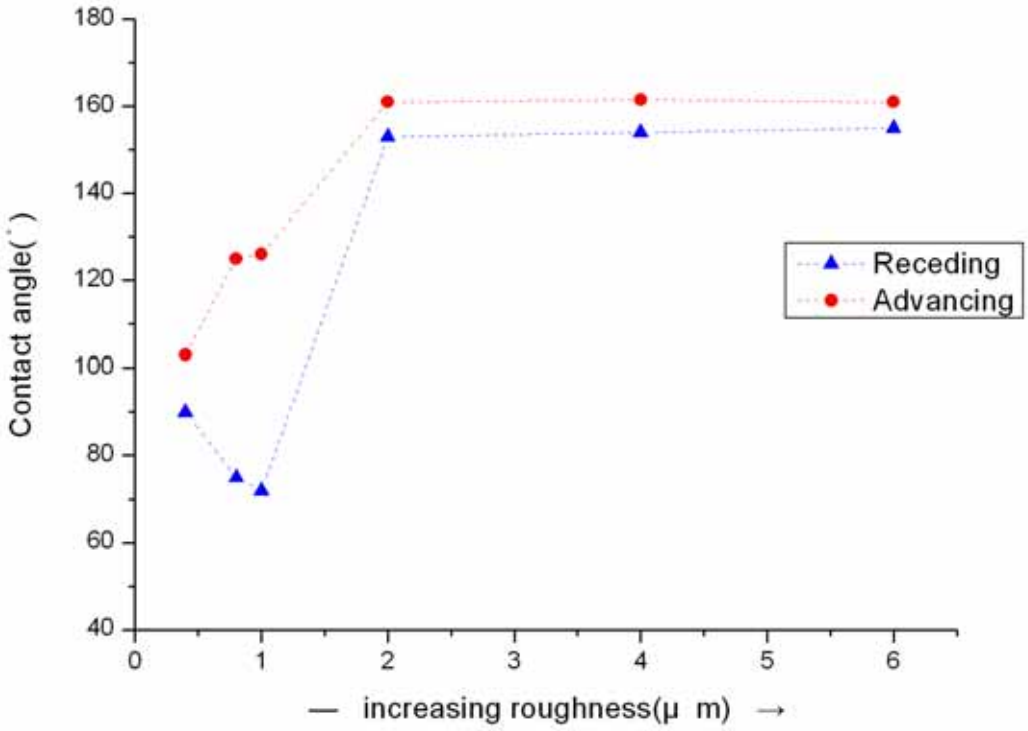


Figure 4-6 Advancing and receding of water drops placed on rough aluminum composite as functions of the roughness of the substrate.

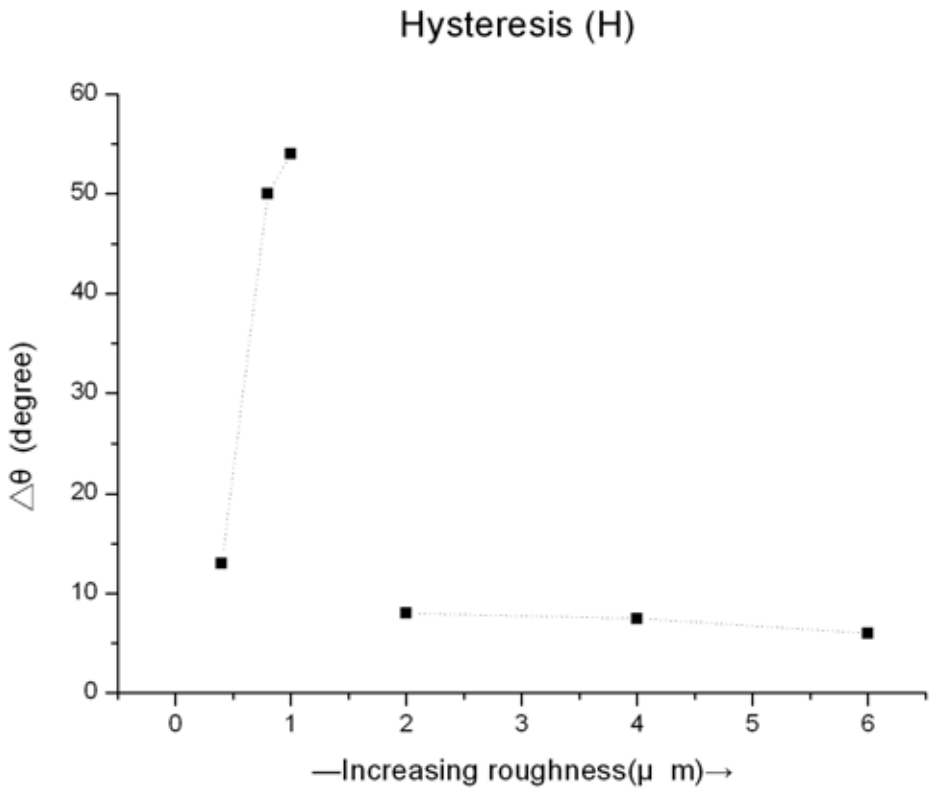


Figure 4.7 CAH, △θ＝θa —θr, as a function of microscale roughness of the substrate.

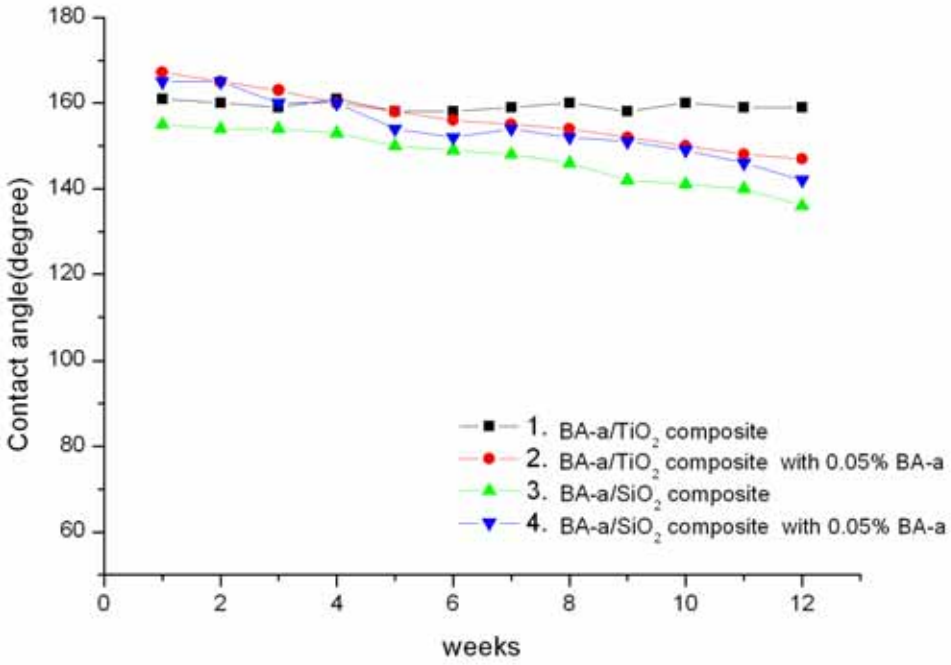


Figure 4.8.Time profiles of the photocatalytic degradation of dirt attached on the surface of BA-a composite obtained by monitoring the contact angle.

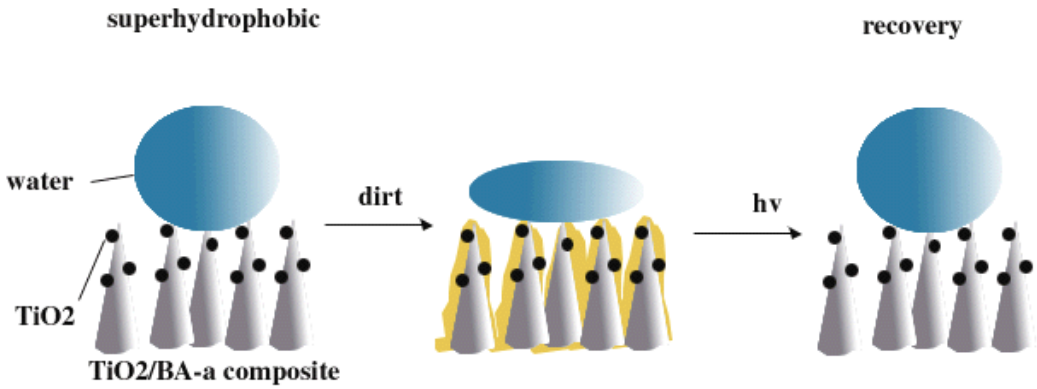


Figure 4-9. The mechanism of self-cleaning and recovery properties on superhydrophobic $TiO_2$/BA-a surface.

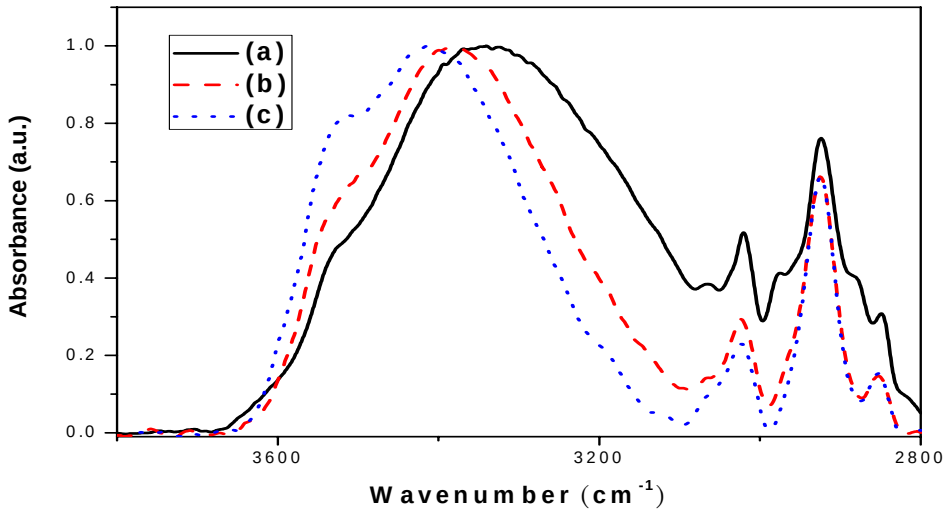


Figure 4.10. The FTIR spectra of pure PVPh homopolymer (Mw = 9697) (a) solvent casting (b) spin coating (c) 180℃ 24h thermal treatment.

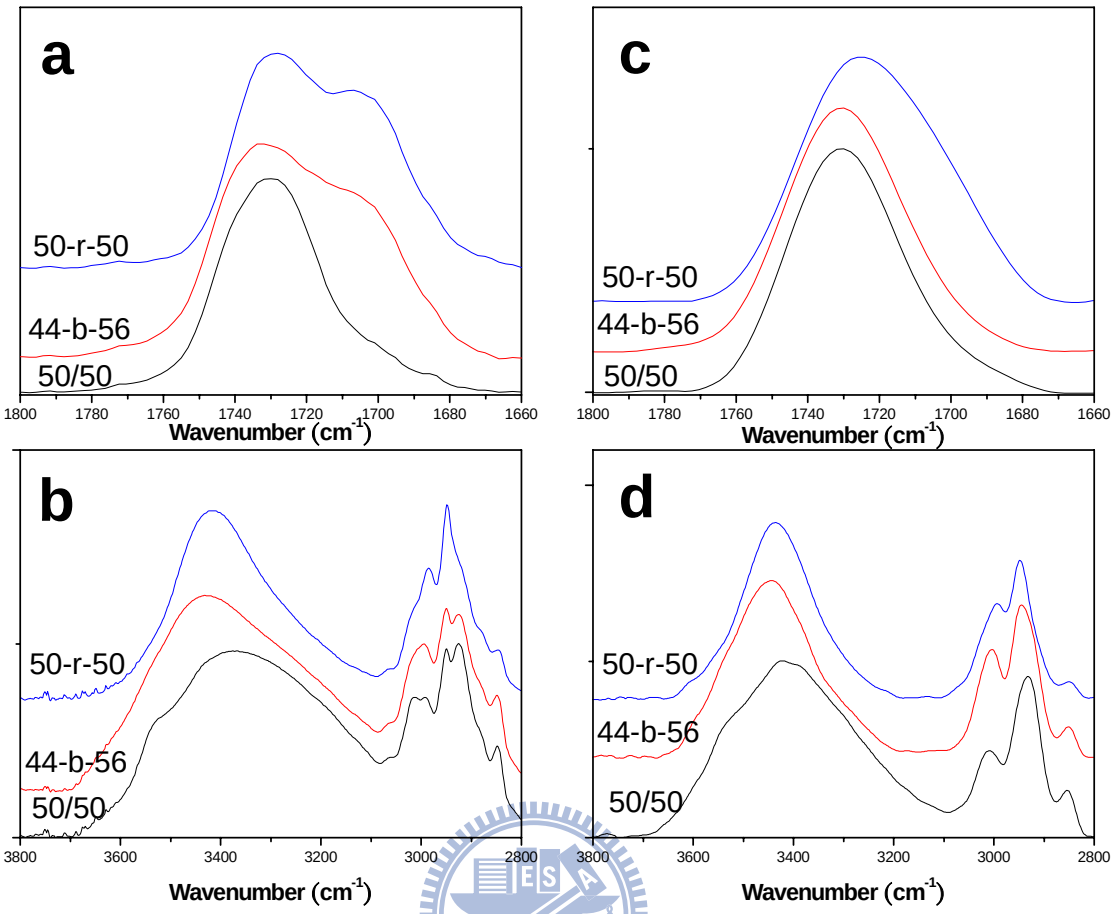


Figure 4.11. The FTIR spectra of samples having similar PVPh contents preparing by different coating process (a)、(b) solvent casting and (c)、(b) spin coating .

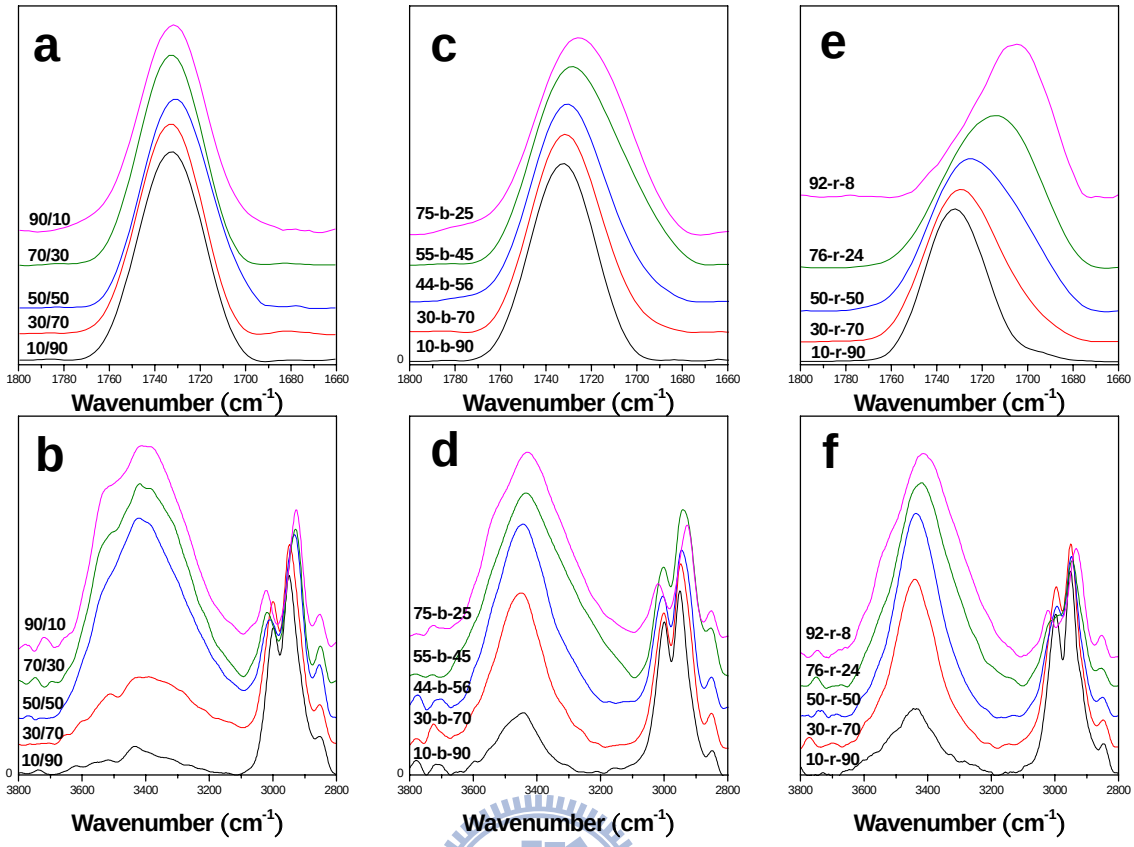


Figure 4.12. FTIR spectra of (a)、(b) PVPh/PMMA blends, (c)、(d) PVPh-b-PMMA copolymers and (e)、(f) PVPh-r-PMMA copolymers at room temperature

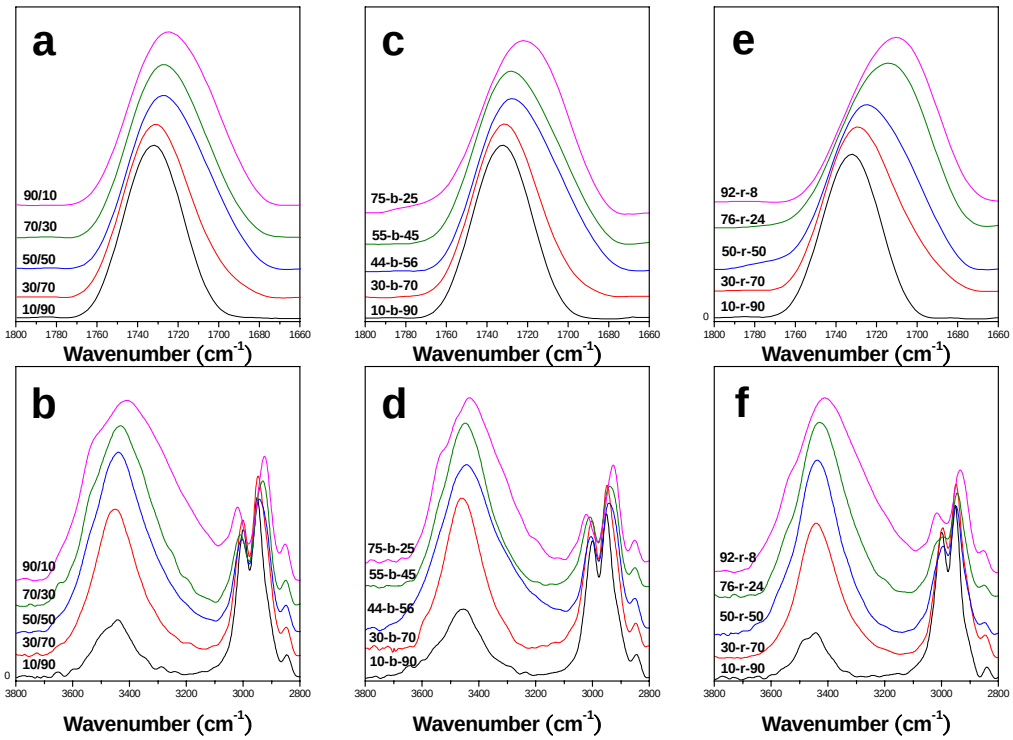


Figure 4.13. FTIR spectra of (a)、(b) PVPh/PMMA blends, (c)、(d) PVPh-b-PMMA copolymers and (e)、(f) PVPh-r-PMMA copolymers after the 180 °C thermal treatment procedure.

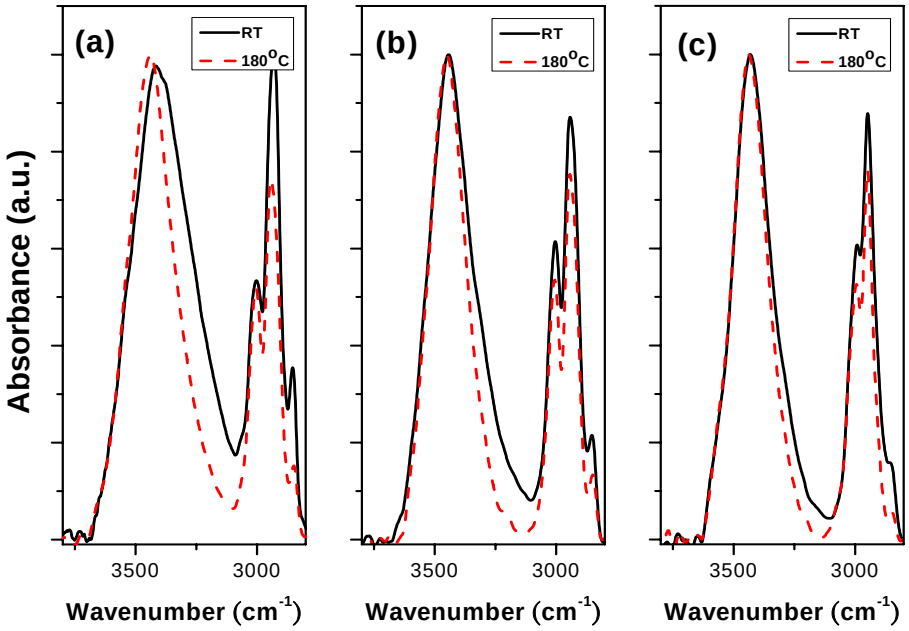


Figure 4.14. FTIR spectra of (a) PVPh/PMMA blends, (b) PVPh-b-PMMA copolymers and (c) PVPh-r-PMMA copolymers in 2800cm$^{-1}$~3800cm$^{-1}$.

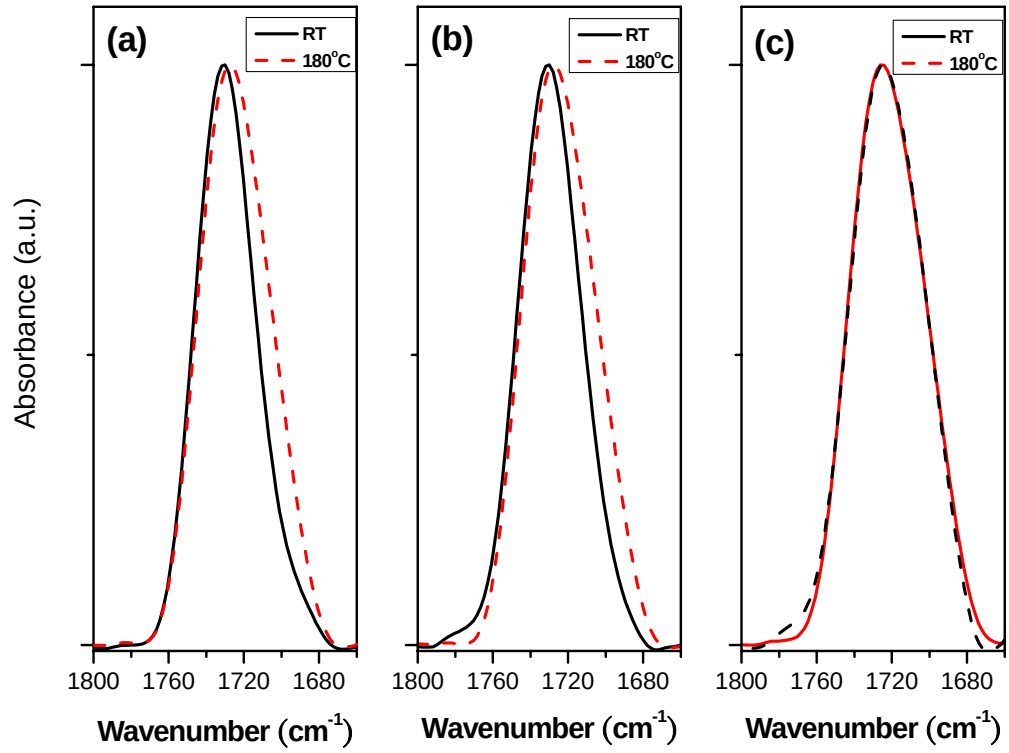


Figure 4.15. FTIR spectra of (a) PVPh/PMMA blends, (b) PVPh-b-PMMA copolymers and (c) PVPh-r-PMMA copolymers 1660cm$^{-1}$~1800cm$^{-1}$.

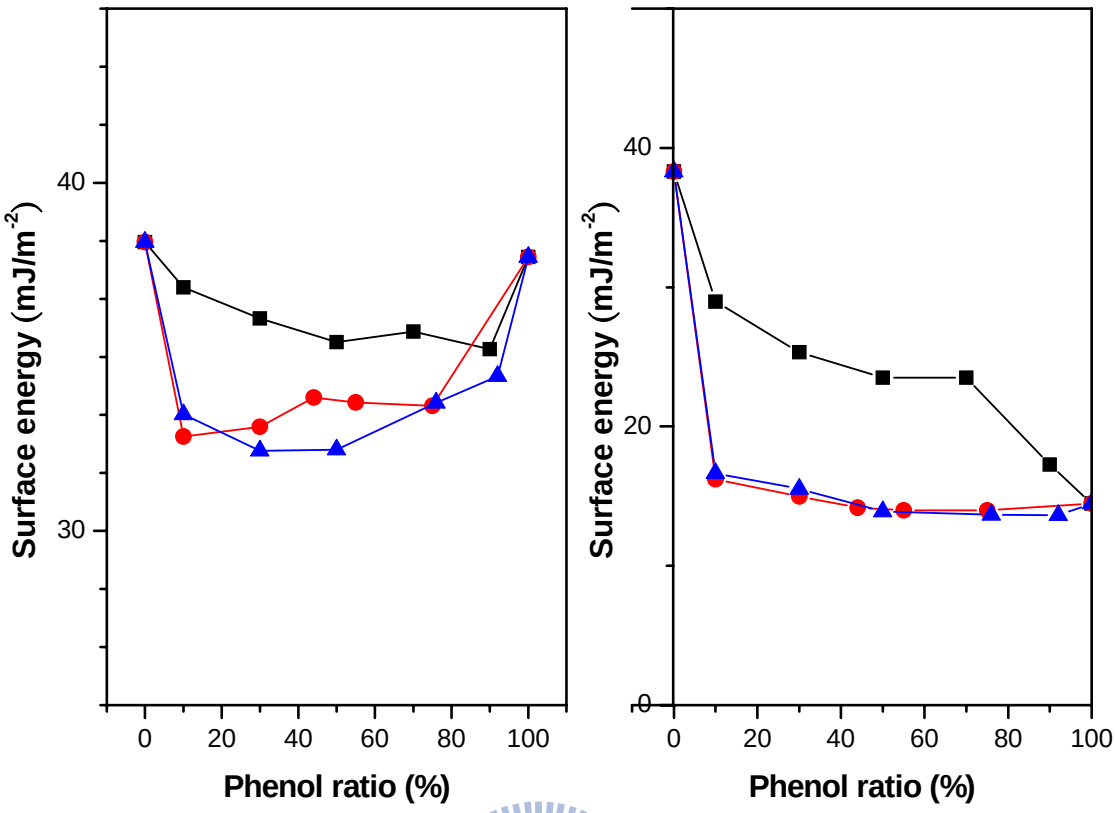


Figure 4.16. Surface energy of PVPh/PMMA random copolymers (▲), block copolymers (●) and their blends (■) (a) before (b) after the thermal treatment process.

# Chapter 5

# Conclusions

The technology of self-cleaning coatings, superhydrophobic surfaces, have attracted much interest because of potential applications in daily life as well as in many industrial processes. We use a simple method for fabricating a lotus-like micro–nanoscale binary structured surface of aluminum. The aluminum microsheets were generated by sandblasting then cleaned by ultrasonic cleaning ,and the nanoscale was produced by coating a complex polymer of nanoparticles and Polybenzoxazine Thus, a simple drop drying technology has been successfully developed for fabricating a complex lotus-like micro–nanostructure. The coating of polybenzoxazine/nanoparticles on films produced superhydrophobic surfaces with contact angle for water larger than 150° and the rolling angle smaller than 10° respectively

Self-cleaning coatings have been used in nature for millennia.It is only in the past decade that commercial self-cleaning products have become available to the consumer. The use of a self-cleaning coating is attractive as they are labour saving and effectively improve the appearance of the environment. Two main forms of self-cleaning films have been developed – superhydrophobic films that repel water droplets, and $TiO_2$ films that show attractive photocatalytic properties for the destruction of organic dirt. One interesting new development of the titania-based coatings is their ability to destroy harmful bacteria and viruses by photocatalytic action using sunlight.We introduce the photocatalytic concept to our superhydrophobic system,that can make a smart self-cleaning superhydrophobic

surface. Our results is considered significant importance industrial applications in the future.

The decrease of the intermolecular hydrogen-bonding fraction between hydroxyl groups of PVPh in PVPh/PMMA systems through a simple thermal treatment procedure tends to decrease the surface energy. The sequence distribution of the vinylphenol group in PVPh-co-PMMA copolymers plays an important role in dictating the final surface energy after thermal treatment. Besides, there is no surface enrichment occurs in PVPh/PMMA systems because of its hydrogen bonding between hydroxyl groups and carbonyl groups. The effects of molecule weight on surface free energy were also investigated carefully in this paper.

# Introduction to Author

English name: Chang-Yuang Li

Chinese name: 李昌源

Birthday: 1978 May 23

Address: No.148, Wunhua Rd., Erlun Township, Yunlin County 649, Taiwan (R.O.C.)

**Education:**

1996.09～2000.06 **B.S.**, Department of Chemistry, Chung Yuan Christian University , Taoyuan , Taiwan.

2005.09～2009.06 **M.S.**, Institute of Applied Chemistry, National Chiao Tung University, Hsinchu, Taiwan.

**Experience:**

Engineer, Far Eastern Textile Co. Ltd